Atmospheric Characterisation of Jupiter using Polarimetric Data

H. Frericks

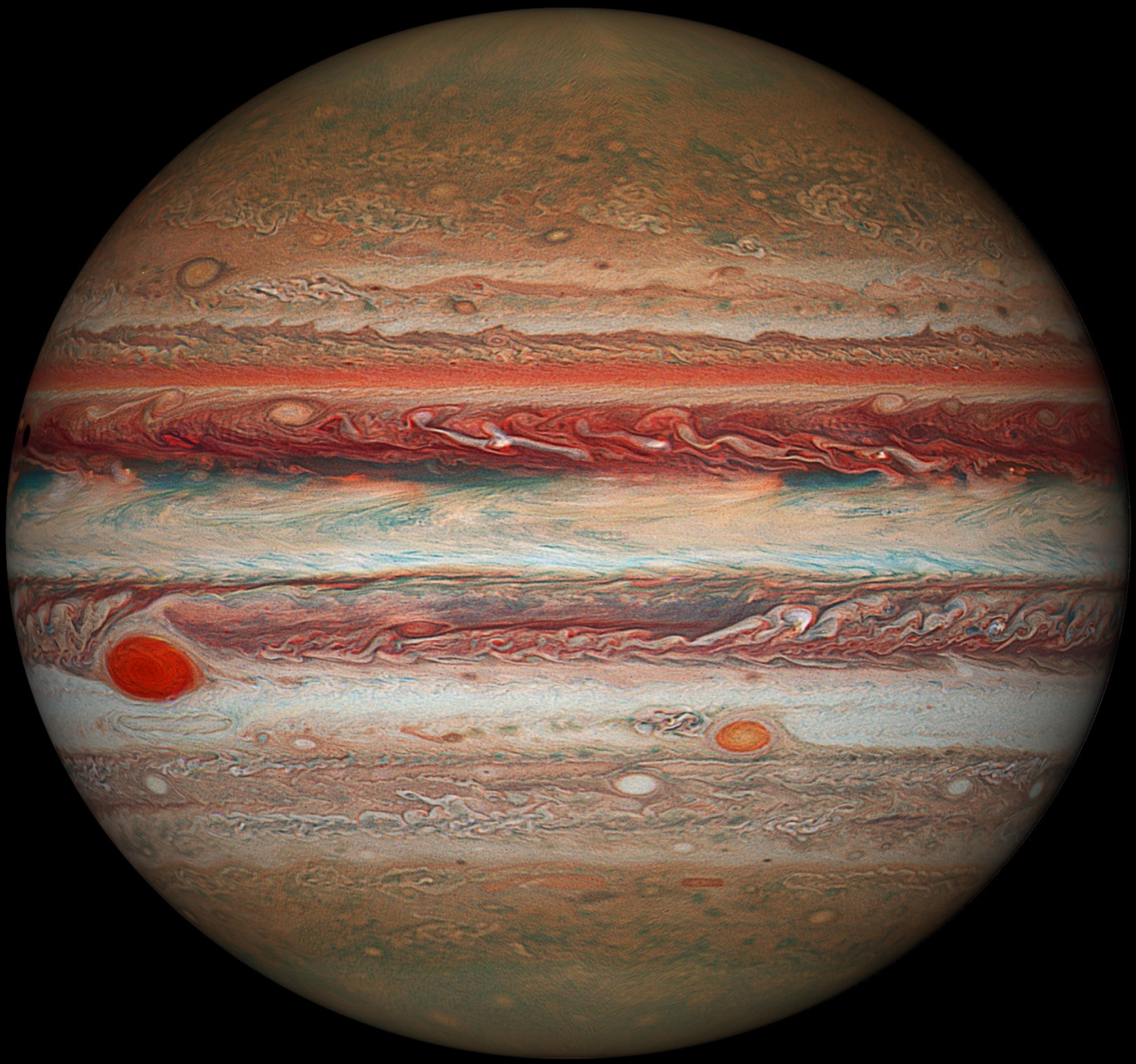

Credits: NASA/ESA Hubble Space Telescope OPAL programme, STScI, Karol Masztalerz

TU Delft Delft University of Technology

Challenge the future

(*This page is intentionally left blank*)

Atmospheric Characterisation of Jupiter using Polarimetric Data

by

H. Frericks

in partial fulfillment of the requirements for the degree of

Master of Science
in Aerospace Engineering

at the Delft University of Technology,
to be defended publicly on wednesday august 26, 2020 at 10:00.

Supervisor:	Prof. dr. L. L. A. Vermeersen
Thesis committee:	Prof. dr. ir. P. N. A. M. Visser
	Dr. A. Cervone

This thesis is confidential and cannot be made public until august 26, 2020

TU Delft Delft University of Technology

(*This page is intentionally left blank*)

Preface

This report is done in fulfilment of the graduation requirements of the MSc Spcaceflight programme at the Faculty of Aerospace Engineering at Delft University of Technology. This MSc thesis regards the topic of atmospheric characterisation of Jupiter using polarimetric data.

I would like to thank my family for their abiding and boundless support. Without them I would not have been able to reach this point of completing my studies. I would also like to thank my fellow students and friends who gave me an unforgettable study time and experience. I want to thank Maria Fernández Jiménez for her help. Also, I want to thank William McLean for his available time, the conversations helped me better understanding and applying the knowledge regarding my Thesis work. I would like to express my gratitude towards prof. Vermeersen and prof. Visser to guide me through the final MSc thesis phase.

Finally, I would like to wish you as reader a pleasant reading.

H. Frericks
July 14, 2020

(*This page is intentionally left blank*)

Abstract

Jupiter is the most visited outer solar system planet, but the exact variation in atmospheric properties along its disk remains largely a mystery. This is where polarimetry fits into the picture. Its added value to spectrometry by additionally measuring the polarisation degree and direction of light makes it a suitable remote sensing tool for the characterisation of planetary atmospheres. It can potentially be used to detect and characterise exoplanets as starlight is originally unpolarised [Kemp et al., 1971] while light reflecting from an object is not. The degree of polarisation is sensitive to the atmospheric properties and its coupling with the wavelength, phase angle and absorption are used to derive the approximate upper atmospheric structure of Jupiter. For this purpose, polarimetric observations of the Torino Polarimeter are compared to the results of a numerical model coded in Fortran. This numerical model uses a doubling-adding radiative transfer algorithm to simulate the polarisation properties of the designated atmospheric profile. The atmospheric profile consists of gas and aerosols, the latter modelled by spherical particles using Mie scattering theory. The numerical model results are processed and compared to the observations using a Matlab script. The particle properties are constrained by the observations using the wavelength filters, the implemented methane absorption and by using a variable cloud pressure and haze optical thickness.

The numerical model results best matching the observations show higher altitude clouds in the higher polarisation degree regions known as the zones, and lower altitude clouds in the belts. The optical thickness of the haze layer turns out to be low or zero in the zones and higher in the belts. To better characterise Jupiter's atmospheric structure, several aspects relating to the observations and the numerical model have to be investigated in more detail in order to improve the matching of the two.

(*This page is intentionally left blank*)

List of Symbols and Abbreviations

Table 1: List of Abbreviations

Parameter	Abbreviation
AU	Astronomical Unit (distance Earth-Sun)
U, B, V, R	Ultraviolet, Blue, Visible, Red (wavelength filter)
CCD	Charged Coupled Device
CCW	Counterclockwise
CW	Clockwise
DAP	Doubling Adding Program
GEOS	Geometry code
GSF	Generalised Spherical Functions
GRS	Great Red Spot
HST	Hubble Space Telescope
RTC	Radiative Transfer Code
SNR	Signal to Noise Ratio
SS	Single Scattering (used as subscript for F and P_L)
STP	Standard Temperature & Pressure
ToPol	Torino Polarimeter
UV	Ultraviolet

(*This page is intentionally left blank*)

Table 2: List of Symbols

Symbol	Physical meaning	Unit
D	Distance to the observer	m
F	Total flux (Stokes vector parameter)	-
G	Geometrical cross-section	m^2
N_A	Avogadro's constant ($6.022 \cdot 10^{23}$)	$mole^{-1}$
N_a	Aerosol number density	m^{-2}
N_{gas}	Number density of the gas molecules	m^{-2}
N_L	Loschmidt number	m^{-3}
P	Degree of polarisation (incl. circular polarisation)	-
P_L	Degree of linear polarisation	-
P_Q	Degree of linear polarisation due to Q	-
P_U	Degree of linear polarisation due to U	-
Q	Linear polarised flux in plane with local horizontal at 0°(Stokes vector parameter)	-
Q_{ext}	Particle scattering efficiency	-
R	Planetary scattering matrix	n.a.
S	Signal (equivalent to the polarisation images at different angles)	-
$\vec{S}$	Stokes vector	n.a.
T	Transmission function	-
U	Linear polarised flux in plane with local horizontal at 45°(Stokes vector parameter)	-
V	Circular polarised flux (neglected in the analysis)	-
b	Optical thickness	-
g	Gravitational acceleration	m/s^2
ga/A_g	Geometric albedo	-
nmug	Number of Gauss points in the DAP	-
npix	Number of pixels used for the numerical model	-
nr/n,nri	Refractive index and its imaginary part	-
plc/plh	pressure layer number for the cloud/haze (Table 4.1)	-
r,r_{eff}	radius, effective radius	μm
v,v_{eff}	variance, effective variance	-
x	scattering type parameter	-
x_{VV}	Generic mixing ratio of the gas	-
α	Planetary phase angle	° (degrees)
ΔP_L	P_L difference of the observations and the numerical model	-
δ	Depolarisation factor	-
θ	Scattering/reflection angle	°
θ_0	Incidence angle (angle between the Sun's position and local vertical)	°
λ	Wavelength	μm or nm
λp	Number of λ points used to construct all filters	-
μ_{atm}	Mean molecular atmospheric weight	$kg/mole$
σ	Error (in the parameter denoted in the subscript)	-
σ_{ext}	Extinction cross-section	m^2
σ_{sca}	Scattering cross-section	m^2
$\phi - \phi_0$	Difference in Azimuth angle of the incident and reflected light	°
χ	Polarisation angle	°

Contents

List of Figures

List of Tables

1

Introduction

Jupiter, being by far the largest planet in our solar system, is a so-called gas giant mainly composed of hydrogen and helium gas. Due to its gaseous properties, the atmosphere blends into the planet's liquid inner layers, making it difficult to distinguish clearly between both. Jupiter's atmosphere contains interesting features as the latitudinal regions known as belts and zones. Zones consist of relative dense, colourless, opaque clouds [Ingersoll et al., 2004] at higher altitudes and belts are relative cloud free at this same altitude, corresponding to holes in the cloud deck revealing the underlying deeper and warmer cloud layers [Ortiz et al., 1998]. Gas rises in the zones and subsides in the belts, forming convection patterns and creating zonal winds, which in turn allow the formation of cyclonic storms such as the great red spot [Ingersoll et al., 2004]. Although Jupiter is the most visited outer solar system planet (9 missions from 1973 onward), the upper atmospheric properties can be investigated and identified in more detail.

This is where polarimetry fits into the picture. Its added value to spectrometry by additionally measuring the polarisation degree and direction makes it a suitable remote sensing tool to contribute to the atmospheric characterisation of planets in this solar system and beyond. Direct starlight is originally unpolarised [Kemp et al., 1987] and becomes polarised by encountering an object (e.g. a planet, asteroid, etc.) Therefore, polarimetry can potentially be used to detect and characterise extra-solar planets as also polarised instead of only unpolarised light will be received from another solar system.

Polarised light has a strong coupling with wavelength and phase angle and is sensitive to the atmospheric properties. It thereby provides information about the planet's upper atmospheric layers. In this report, with upper atmospheric layers the layers having a pressure in the range of table 4.1 are referred to.

In this way, recent polarimetric data is used to analyse Jupiter's atmospheric structure. In [McLean et al., 2017], Jupiter's latitudinal polarisation variation is analysed using five imaging polarimetry data sets taken in different wavelength filters and different atmospheric profiles are proposed. The latitudinal polarisation variation is mainly attributed to a variable cloud top pressure between the layers and the analysis showed that the polar regions have a thicker haze layer compared to the mid-latitudes. [Fernández Jiménez, 2018] used polarimetric data obtained in different wavelength filters to derive the atmospheric profile of Jupiter's great red spot (GRS). It is found that towards the middle of the great red spot the clouds exist at higher altitude and that both the clouds and haze span a larger pressure region towards the edge of

the GRS. In this analysis polarimetric observations are used to analyse Jupiter's atmospheric structure along the entire visible disk. An existing numerical model is extended and serves to compare to the polarimetric observations. The objective is to identify the atmospheric properties matching the polarimetric observations to characterise Jupiter's upper atmosphere. Additionally, it might reveal latitudinal and local variations in atmospheric properties giving more insight in these particularities, enriching the current knowledge of the red gas giant and its atmosphere.

The report is used as guideline to touch upon the aforementioned aspects. First, the background information to serve as fundament is addressed in chapter 2. Afterwards, the polarimetric observations are elaborated upon in chapter 3, followed by the numerical model (chapter 4) and the procedure to compare these two (chapter 5). The result of the comparison of the observations and the numerical model is discussed in chapter 6 and finally the conclusions and recommendations are given in chapter 7 and 8 respectively.

1.1. Research Questions

The research question that forms the basis of this analysis is stated below. The additional sub-questions are introduced to form a complete and solid framework to guide the research in the correct direction.

Main question :

What is Jupiter's atmospheric structure according to the polarimetric observations?

Sub-questions :

- *What are the particle properties of the atmospheric aerosol layers best fitting the polarimetric data?*
- *What is the pressure profile of the aerosol layers according to the polarimetric observations?*
- *How well does the created model fit the polarimetric data?*

2

Background

Before diving into more detail in the polarisation analysis of Jupiter's atmosphere, first useful background information is provided to serve as fundament to build the analysis on.

First, light is shed upon the phenomenon of polarisation (section 2.1), which is used to perform polarimetric measurements to characterise in this case Jupiter's atmosphere (section 2.2). Specific information and particularities of the largest planetary atmosphere in the solar system are addressed in section 2.3 to understand what features might be observed by polarimetry. Finally, the representation of the polarimetric data using the so-called Stokes vector is dealt with in section 2.4.

2.1. Polarisation

Light is a collection of transverse electromagnetic waves, where the electric and magnetic field oscillate perpendicularly to both the propagation direction and to one another. The electric field oscillation defines the polarisation state. Starlight consists of a lot of these electromagnetic waves, and the polarisation direction is totally uncorrelated such that this light is called unpolarised. Although starlight is originally unpolarised [Kemp et al., 1987], it can become (partially) polarised by several principles; scattering, reflection, refraction and diffraction. Also absorption plays a role as absorbed light does not become polarised. In this analysis the main focus will regard scattering and absorption although the other principles also play a role when considering a planetary atmosphere.

Reflection is the dominant polarisation source on a planetary surface. The bottom of the atmospheric model used in this analysis comes closest to a planetary surface. However, in this analysis the bottom of the atmosphere is regarded a black surface which means that all light reaching this point will be absorbed (surface albedo is 0.0) instead of reflected.

Absorption is an important principle to consider. Both absorption in the gaseous layers of the atmosphere and the aerosol layers is taken into account in the analysis, as will be discussed later on.

In the analysis an optically thick cloud layer is regarded such that the amount of light reaching the atmospheric bottom is small. Consequently, the relative influence of absorption at the atmospheric bottom compared to absorption in the other atmospheric layers is small.

Another well known atmospheric phenomenon is scattering; the redirection of light rays from the original propagation direction by encountering suspended atmospheric particles diffusing the radiation partially. Scattering occurs in all media and is thus considered for both the gaseous and aerosol layers as will be addressed later on.

Scattering can be subdivided into two main parts: Single scattering by single particles and multiple scattering by the entire atmosphere. The latter occurs in both the gaseous and aerosol layers. Multiple scattering tends to lower the degree of polarisation. Single scattering can be split up in many types, in this analysis it will be limited to Rayleigh scattering and Mie scattering.

The distinction between the single scattering types is usually done based on a relation of the particle radius to the wavelength of the light passing through, given in equation 2.1 [Hansen and Travis, 1974]. Where $x << 1$ corresponds to Rayleigh scattering, $x \approx 1$ to Mie scattering and for $x >> 1$ (much larger e.g. $x > 1000$ for example) scattering in the geometrical optics regime occurs. The latter is not applicable for this analysis.

$$x = \frac{2\pi r}{\lambda} \tag{2.1}$$

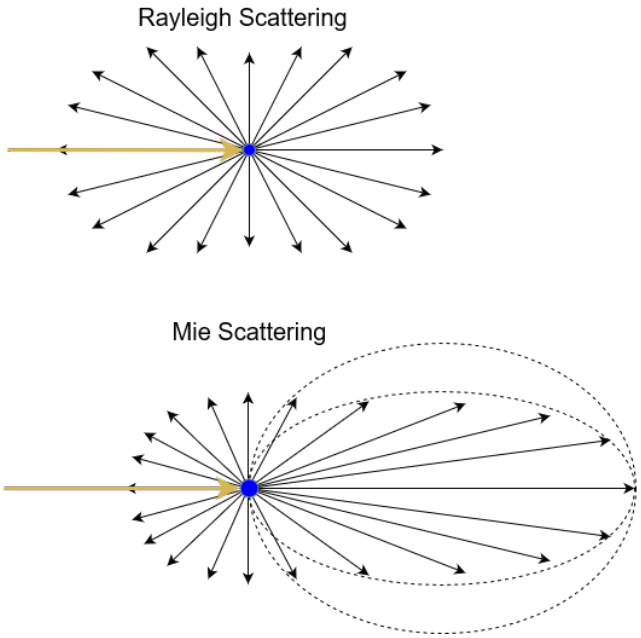

Figure 2.1: Rayleigh ($x << 1$) and Mie ($x \approx 1$) scattering visualised

Figure 2.1 visualises the scattering intensity using arrows indicating the magnitude as a function of the scattering angle (θ), where 0° corresponds to forward and 180° to backward scattering. Additionally, the gold arrow indicates the direction of the incident light and the blue circle the particle.

As can be seen from figure 2.1, the forward scattering pattern (right-side of the figure) depends stronger on x than the backward scattering pattern. The higher x is, the (relative) larger the forward scattering becomes (to a certain extent, visualised in Figure 2.1 by the dotted ellipses). Note that the figure shows the relative/normalised scattering intensity per scattering type. Also, note that Figure 2.1 shows examples for the forward Mie scattering (dotted

ellipses), but more angular patterns are possible. Thus unpolarised starlight can become polarised by the afore-mentioned principles which are briefly discussed above, which can be used to characterise a planetary atmosphere using polarimetry.

2.2. Polarimetry

Polarimetry is a technique used to measure the polarisation state of light, which can be used to provide information about planetary atmospheres.

Various polarimetric related research has been performed in the past and the planetary atmospheres of several planets as, among others, the Earth, Venus and Jupiter have been investigated. The latter will be focused on specifically as Jupiter is the subject of this analysis.

In 1929 [Lyot and Tessier, 1929] were the first to perform (Earth based) linear polarisation research regarding Jupiter in the visible wavelength spectrum. Later, the degree of Jupiter's circular polarisation was proved to be in the order of magnitude 0.001% for the hemispheres [Kemp et al., 1971]. The feature of the increasing degree of linear polarisation towards the poles was already observed by [Lyot and Tessier, 1929] at a wavelength of 560nm. [Gehrels et al., 1969] observed regions near the poles and equator for different wavelengths and phase angles enriching Jupiter's polarisation data. It was until 1973 that only Earth based observations, limiting the phase angle to about 12°, were conducted. This abruptly changed by the first Jovian flyby of Pioneer 10 in 1973, initiating a breakthrough for polarisation research due to the phase angle extension. It was shown that the degree of polarisation is also increasing towards the poles at higher phase angles [Tomasko et al., 1978]. This deduction was later linked to the presence of haze layers [West et al., 1986], which turn out to become optically thicker with increasing latitude, in combination with the fact that aggregates of fluffy particles are expected at the poles [West et al., 2004]. During the years that followed, several atmospheric models considering different cloud layers were formed, providing indications of Jupiter's atmospheric structure. The latitudinal polarisation variation indicating the contrast of the belts and zones is also addressed (among others by [West et al., 1986]).

As mentioned previously, direct starlight is originally unpolarised [Kemp et al., 1987], but can become polarised by encountering a planetary atmosphere due to the afore-mentioned principles. The degree of polarisation (P) relates to several atmospheric properties which characterise the atmospheric profile. The degree of polarisation is sensitive to the aerosol layers and its atmospheric properties (the pressure at where the aerosols are situated and the optical thickness of these layers), as well as to its particle properties (the size, variation in size, refractive index and the imaginary part of the refractive index which relates to the absorption properties of the particle). Besides, the degree of polarisation correlates with the gas molecules present in the atmospheric layers, such that molecular scattering and absorption contribute too. Data obtained at different wavelengths complement to a more complete picture as the sensitivity to the atmospheric parameters varies significantly with wavelength. Additional information is provided by the polarisation angle, which defines the direction of polarisation. The polarisation angle is not used in this analysis as it complicates the optimisation procedure.

The relation for the phase angle is $\alpha = 180° - \theta$ such that a low phase angle corresponds to almost back-scattering (θ close to 180°). As the Earth is closer to the sun than Jupiter, the maximum phase angle for ground-based observations is limited to about 12°. The phase angle is shown in Figure 2.2 and depends on the position of the Earth and Jupiter which in turn depends on the observation time. To fully characterise Jupiter's atmospheric properties

from polarimetric data a larger phase angle range is required, which can be achieved by In-situ measurements using an orbiter. This additional data can thus help in constraining the atmospheric properties, similar to the added value of the different wavelength filters.

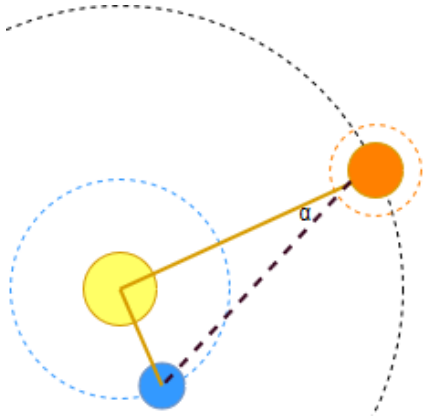

Figure 2.2: Sketch of the phase angle of Jupiter
(Yellow: Sun, Orange: Jupiter, Blue: Earth, dotted lines (blue, black) show orbits and Jupiter's atmosphere (orange))(Not to scale)

So far, most atmospheric characterisation has been performed using spectrometry; obtaining flux measurements. Stars (as the Sun) emit light or so-called electromagnetic waves, providing a certain power that is inversely proportional to the distance to the star squared (due to the star's spherical shape). The power received per unit area (W/m^2) is defined as the solar irradiance or flux. When this flux reaches a surface or atmosphere, part of it is reflected (Albedo) and part of it is absorbed and re-emitted (Infra-red) back into space. This flux of Jupiter's visible disk provides information about its atmospheric properties. When measuring the total flux (F) only, the effect of optically thick atmospheric layers as clouds is much larger than optically thinner layers as hazes, while the effect of the hazes on the polarisation state on the contrary is substantial. Also, the flux reflection effect of different composed layers can be very similar. In this way, the sensitivity of the flux result to the atmospheric properties is lower compared to the additional degree of polarisation.

Polarimetry adds value to the flux data by additionally measuring the degree and direction of polarisation, the degree of polarisation is namely more sensitive to the atmospheric and particle properties (see figures of [McLean et al., 2017]).

On the other hand, it becomes a difficult task to find an atmospheric profile that fits the observations well. Many parameters play a role and the effect of different parameters is interlinked, and depends on the wavelength. This greatly increases the optimisation time and complexity.

2.3. Jupiter's Atmosphere

In 1995 the Galileo mission was the first in probing Jupiter's atmosphere and thereby providing in-situ data for the probed locations. The acquired data is analysed and results can be found in (among others) [Niemann et al., 1996], [Sromovsky and Fry, 2002] and [Atreya et al., 2003]. Jupiter's upper atmosphere consists mainly of hydrogen (H_2)(about 86.4%), followed by helium (He)(about 13.6%) and more complex components as methane (CH_4) and ammonia (NH_3). The afore-mentioned composition regards the gas present in Jupiter's upper atmosphere.

Besides the gas, the upper atmosphere also contains aerosols, which in this case are subdivided in optically thick clouds (with relative large particles) and optically thin hazes (with smaller particles) (as is done in [McLean et al., 2017] and [Fernández Jiménez, 2018] as well).

Note again that, in this report, with upper atmosphere or atmospheric layers the layers having a pressure in the range of table 4.1 (up to about 5.6bar) are referred to. For this part of the atmosphere, the main constituents of hydrogen en helium are in the gas phase. With increasing pressure, the main constituents of hydrogen and helium first come in the liquid phase (which starts at a pressure of about 1.7Mbar [Lissauer and de Pater, 2013]) and with even higher pressure become electrically conducting like metals. Finally, the composition of the centre core of Jupiter is not exactly known, it is expected to be composed of solid material. [Militzer et al., 2016]

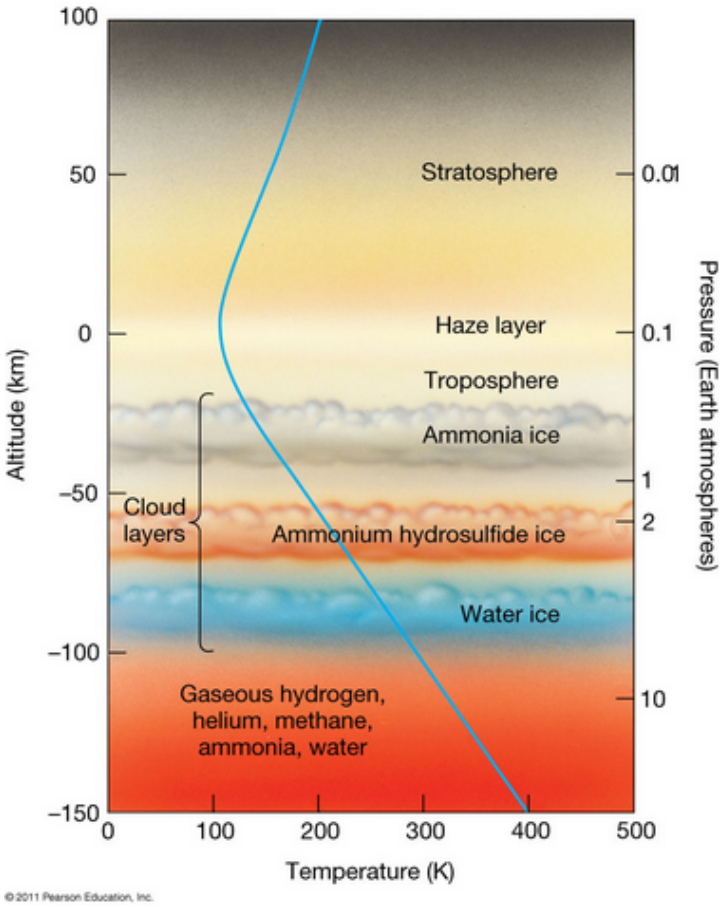

Figure 2.3: Jupiter's expected atmospheric structure (©Pearson Education Inc)

In reality, Jupiter's aerosol layers have no clearly defined horizontal and vertical boundaries and therefore vary with location and pressure. However, all (found) performed research agrees on Jupiter's different cloud layer composition. In essence, three cloud layers are expected as being a water (H_2O), ammonium-hydrosulfide (NH_4SH) and ammonia (NH_3) cloud (in sequence of decreasing pressure or increasing altitude) [West et al., 2004]. The haze layer is defined as the overlaying layer of the highest (ammonia) cloud, which is expected to become optically thicker towards the poles (see among others [West et al., 2004], [McLean et al., 2017]). The expected atmospheric structure is visualised in figure 2.3 and gives an idea of the pressure level and altitude at which the aerosol layers are expected.

In Jupiter's atmosphere latitudinal bands are present, the lighter bands are often referred to as zones and the darker as belts. Spectroscopic observations showed that zones consist of relative dense, colourless, opaque clouds [Ingersoll et al., 2004]. On the contrary, the belts correspond to clouds deeper (higher pressure, lower altitude) in the atmosphere and therefore to warmer layers [Ortiz et al., 1998]. As gas rises in the zones and subsides in the belts, convection patterns are formed. The rising and subsiding air motions cause a latitudinal temperature and pressure gradient between the belts and zones. As wind blows from high to low pressure regions, the pressure gradient induces winds to blow. The planetary rotation defines the direction of these zonal winds (known as the Coriolis effect), on the northern hemisphere, the wind curves towards the planet's rotational direction while on the southern hemisphere it curves towards the opposite direction. [Lissauer and de Pater, 2013] High pressure systems or cyclonic storm systems as the great red spot can form at the belt-zone boundaries [Ingersoll et al., 2004] where the zonal winds are largest, the rotational state is as mentioned before.

The above is visualised in Figure 2.4 where the darker belts, the lighter zones and the great red spot (GRS) can clearly be seen. The zonal winds reaching extreme velocities at the belt-zone boundaries (for example shown in fig 8.4 of [Lissauer and de Pater, 2013]) are indicated in the frame on the left too.

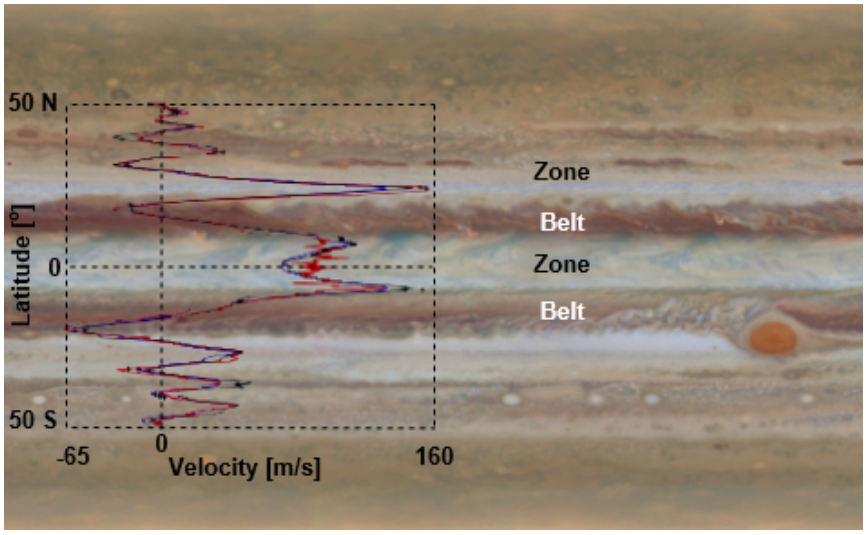

Figure 2.4: Zonal wind over Jupiter's surface
(Both figures adapted and combined from [Wong et al., 2015]) Red: Voyager (1979), Blue: Cassini (2000), Black: HST (2015), Eastward velocity is defined as positive

2.4. Stokes Formalism

In 1852, George Gabriel Stokes came up with a way of representing polarised light making use of the so-called Stokes vector (see equation 2.2 [Hansen and Travis, 1974]). This vector plays an important role as the degree of polarisation can be derived from its parameters (see chapter 3).

$$\vec{S}(\alpha,\lambda) = \begin{bmatrix} F(\alpha,\lambda) \\ Q(\alpha,\lambda) \\ U(\alpha,\lambda) \\ V(\alpha,\lambda) \end{bmatrix} \tag{2.2}$$

F is the total flux, Q and U the linear polarised flux, with Q defined in a plane with a local horizontal of 0° and U in a plane with a local horizontal at 45° and V is the circular polarised flux.

Stokes' parameters Q and U are defined w.r.t. the plane in which both Planet, Star and observer lie; the planetary scattering plane. The parameters can be transformed to another reference plane of choice (which might become useful when the polarimetric data is obtained in an inclined plane) via the transformation matrix given in equation 2.3 [Hovenier and van der Mee, 1983]. The angle β denotes the angle between the old and new reference plane, defined in counter-clockwise direction, when looking towards the observer.

$$L(\beta) = \begin{bmatrix} 1 & 0 & 0 & 0 \\ 0 & cos(2\beta) & sin(2\beta) & 0 \\ 0 & -sin(2\beta) & cos(2\beta) & 0 \\ 0 & 0 & 0 & 1 \end{bmatrix} \tag{2.3}$$

The Stokes vector parameters (F, Q, U, V) can be combined to form the degree of polarisation as is shown in equation 2.4.

$$P = \frac{\sqrt{Q^2 + U^2 + V^2}}{F} \tag{2.4}$$

Making use of the simplification that the circularly polarised flux (V) is negligible which is proven to be a good assumption [Kemp et al., 1971], the degree of linear polarisation can be found (see equation 2.5).

$$P_L = \frac{\sqrt{Q^2 + U^2}}{F} \tag{2.5}$$

The linear polarisation vector is inclined w.r.t. the horizontal plane, defining the polarisation angle χ as stated in equation 2.6 [Hansen and Travis, 1974].

$$\chi = \frac{1}{2} arctan2(\frac{U}{Q}) \tag{2.6}$$

This is the procedure to derive the degree of polarisation from the Stokes vector parameters. It is applicable to this analysis as well as all Stokes vector parameters can be generated with the numerical model code along the visible disk, and consequently the polarisation state of all local points can be deduced from it.

3

Observations

This chapter addresses the observations and how to derive the degree and direction of polarisation from it. The working principle of the instrument, the Torino Polarimeter is touched upon (section 3.1) as well as the errors and inaccuracies present in the data (section 3.2). Finally, the wavelength filters in which the observations are obtained are dealt with (section 3.3). It is important to note that the observations are provided in this analysis such that additional calibration and pre-processing is not applicable nor required.

The ground-based polarimetric observations are taken in the Ultraviolet, Blue, Visible and Red (U, B, V and R) wavelength filters on 08-06-2016 with the Torino Polarimeter (ToPol) installed on a 1-m telescope at the Calern observing station of the Observatoire de la Côte d'Azur in France [Devogèle et al., 2017]. At this time, the planetary phase angle (α, the angle between the Sun, the target (Jupiter) and the observer (Earth)) is $10.73°$, which is favourable as it is close to the maximum phase angle when observing Jupiter from Earth of about 12 degrees.

The polarimeter's double wedge, in combination with the double Wollaston prisms let the incoming rays emerge at four different angles (forming four different beams) creating four polarisation images at different angles (0, 45, 90, 135°), corresponding to the Stokes parameter combinations F+Q, F-Q, F+U and F-U (or signals $S_{1,2,3,4}$) [Oliva, 1997]. The CCD contains four horizontal strips and each beam projects an image in one of these strips. To acquire the individual Stokes parameters (F, Q, U), the images of the four beams have to be combined.

Afterwards, the degree of linear polarisation (P_L) can be determined from these Stokes parameters according to the procedure shown in equation 3.1 to 3.3 [McLean et al., 2017].

$$P_Q = \frac{Q}{F} = \frac{S_1 - S_2}{S_1 + S_2} \tag{3.1}$$

$$P_U = \frac{U}{F} = \frac{S_3 - S_4}{S_3 + S_4} \tag{3.2}$$

$$P_L = \sqrt{P_Q^2 + P_U^2} \tag{3.3}$$

3.1. The Torino Polarimeter

As mentioned before, the observations are obtained using the Torino Polarimeter (ToPol). The working principle of the instrument is shown in Figure 3.1. Light enters at the pupil image [Oliva, 1997] (top left in the figure) and encounters the combination of wedge and wollaston. Part of the light encounters the combination of upper wedge and wollaston, creating the polarisation images at 0 and 90° (see right part of the figure). The same principle holds for the

downward facing wollaston and corresponding wedge, which creates the 45 and 135° polarisation images. This is the basic principle of the ToPol. Note that the Wollaston up and down terms refer to both the position and orientation of the Wollastons which is opposite from the orientation of the wedges.

From Subfigure 3.1b it can be seen that generally a polarimeter uses several lenses to focus the light additional to the wedge-wollaston part (which holds for the ToPol as well, although not explicitly shown in Figure 3.1a). The light entering the wollaston prisms is refracted into different light beams, where the final lens is used to project the polarisation images on the CCD (the detector). As all the polarisation images (at 0, 45, 90 and 135 °, corresponding to F+Q,F-Q,F+U,F-U) are projected on one CCD, the Stokes vector parameters F, Q and U can be deduced from the ToPol measurements. Note that with the polarimeter of Figure 3.1b the circular state of polarisation (V) can be determined using the middle wedge-wollaston combination using a quarter wave plate (QWP). However, with the ToPol the circular polarisation (V) has not been measured (no QWP is present) and is consequently not used in the analysis.

Figure 3.1: Working principle of the Torino Polarimeter

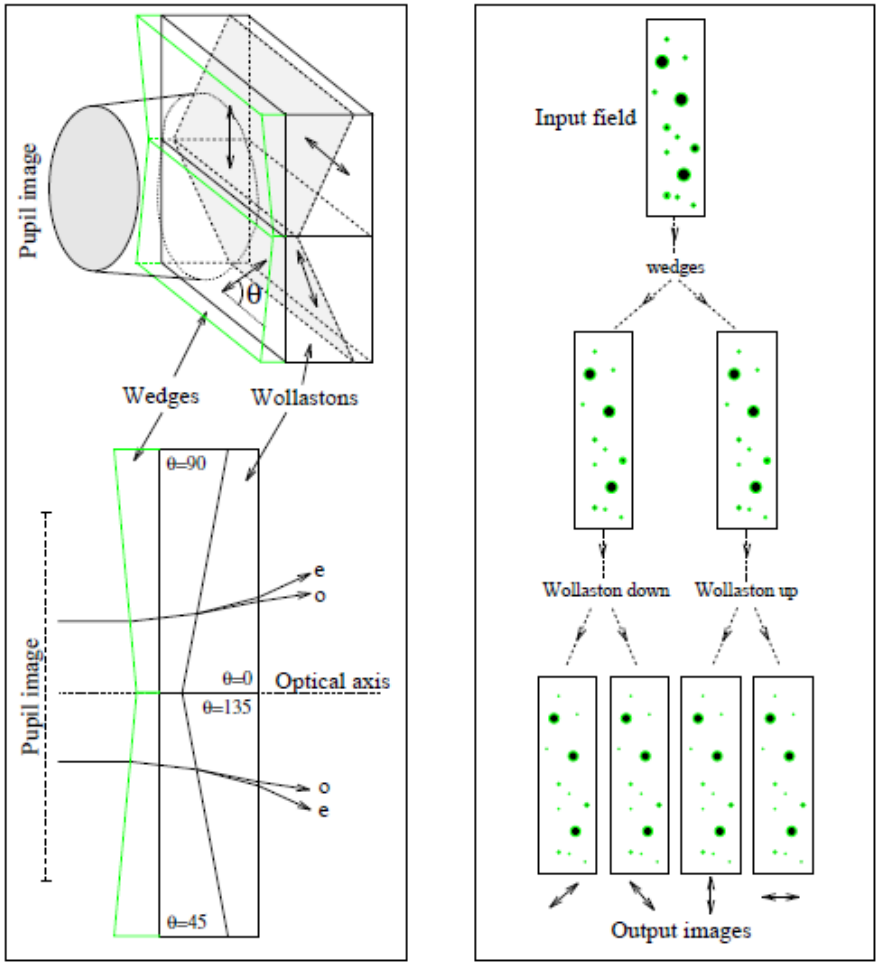

(a) Working Principle of the ToPol [Oliva, 1997]

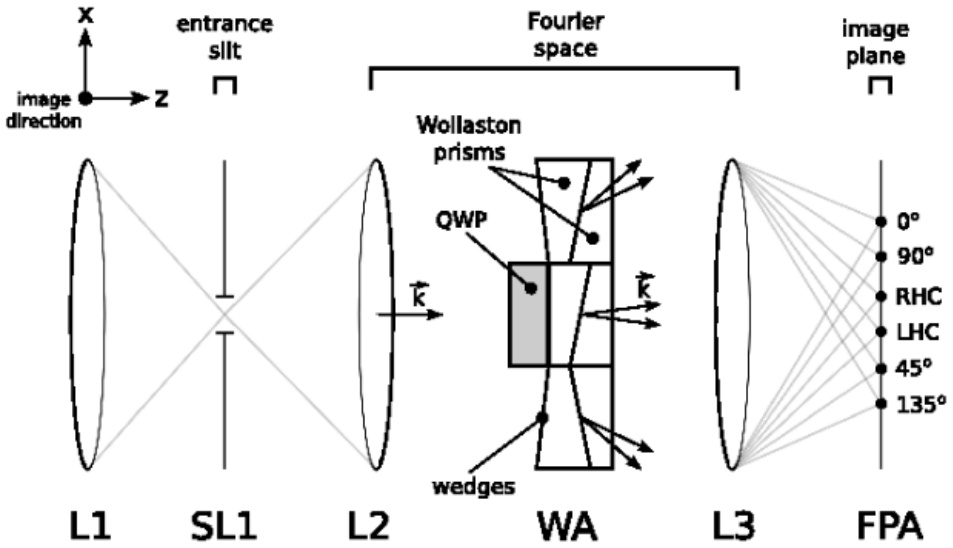

(b) Example of a Polarimeter using wedges and wollastons (credit: Semantic Scholar)

3.2. Errors and Inaccuracies

The errors and their corresponding inaccuracies can be subdivided in two categories; the observational and instrumental errors. The errors determine the accuracy of the observations, which is essential to classify if a model fits the observations well.

3.2.1. Observational Errors

The observational errors relate to the inaccuracies in the observations itself. Even with a (theoretically) perfect instrument, error sources are present due to other aspects. The ground-based instrument observes Jupiter through Earth's atmosphere, inducing a seeing limitation which causes a spreading out effect of the observational parameter values per pixel location. This means that a certain pixel value is influenced to a certain extent by the values of the surrounding pixels. It is found by [McLean et al., 2017] that the minimum resolvable detail on Jupiter's disk at the observation time is about 1 arcsec. As the plate scale of the images was 0.2379 arcsec/pixel, an area of 5x5 pixels ($5 \cdot 0.2379 > 1$) is regarded to apply box-car smoothing on in the analysis of [McLean et al., 2017] for the separate Stokes vector parameters before constructing P_L from it.

Another observational error relates to the amount of noise present in the data, which is usually taken into account by the signal-to-noise ratio (SNR). The noise error scales with the SNR of the data, so with the square-root of the number of photons falling on each separate pixel of the detector. It is found that the errors in P_Q and P_U can be determined with equation 3.4 and 3.5 [McLean et al., 2017]. These equations show the relative error which scales with the signal to noise ratio (SNR) of the data according to [McLean et al., 2017].

$$\sigma_{PQ} = \frac{1}{\sqrt{S_1^2 + S_2^2}} \tag{3.4}$$

$$\sigma_{PU} = \frac{1}{\sqrt{S_3^2 + S_4^2}} \tag{3.5}$$

The equation for the photon noise error for the degree of linear polarisation (P_L) [Bagnulo et al., 2009] is given by equation 3.6.

$$\sigma_{P_L} = \sqrt{cos^2(2\chi)\sigma_{P_Q}^2 + sin^2(2\chi)\sigma_{P_U}^2} \tag{3.6}$$

For the noise error to be relative small, a long exposure time would be preferred as in this way a larger number of photons will fall on the detector.

When evaluating the noise error on P_L (σ_{PL}) using the observations and equation 3.6, it turns out that this error source is relatively small (order of magnitude (of maximum values) of 10^{-5} for all wavelength filters) compared to the other error sources (see sub-section 3.2.3).

3.2.2. Instrumental Errors

Distortion between the strips in an individual image occurs because of the different optical paths of the signal in each strip. If the wedge and wollaston are up or down (or one up and one down) it influences the optical path slightly. Furthermore, as can be seen in figure 3.1b, the polarimeter used consists of several elements; lenses, the Wollaston prisms, etc. Due to slight imperfections in these elements, the light path can be slightly deviated causing the pixels of the different strips not to match perfectly. So the alignment error is caused by the different optical

paths of the signal in each strip. Additionally, misalignment of consecutive images occurs due to slightly inaccurate guiding of the telescope according to [McLean et al., 2017].

In the data reduction a significant issue is present regarding this distortion. For point sources this is not a problem as the pixel counts within an aperture are added up and the background is subtracted as no details have to be resolved. Therefore, the pixel values are summed up to finally deduce P_L from it. In this case disk-resolved observations are regarded and it has to be possible to distinguish different features (as the GRS) from the data. As Jupiter's visible disk is resolved in individual pixels having a unique value, it is aimed to align each strip pixel by pixel such that each detector pixel corresponds to the exact same region on the disk. In reality, it is difficult to align these strips due to the different optical paths of the signal in each strip, such that an error is induced. (based on [McLean et al., 2017]) The effect of this error is relative large when the P_L variation along the disk is large as well. This distortion-alignment effect can be compensated for by averaging over an array of pixels by applying smoothing. The 5x5 pixel smoothing proposed before [McLean et al., 2017] can be used to compensate for both seeing limitation and distortion at the same time. (based on [McLean et al., 2017]) An estimation of the alignment error will be discussed in the upcoming section.

Another influencing factor is the sensitivity of the different detector pixels, which might vary slightly. Consequently, the sensitive detector pixels will have more photon counts than the less sensitive pixels. With polarimetry this effect is small as the degree of polarisation is a relative measure and the number of photons per detector pixel is large. According to [Devogèle et al., 2017], analyses of flat fields show that the CCD has no dead pixels and dark frame analyses show that 24 isolated pixels posses a high dark current value.

The results generated with the model (see chapter 4) are less reliable near the edges as well. The model namely assumes local plane parallel layers at each pixel location. This means that a light beam enters with an angle θ_0; the angle between the Sun's position and the local vertical. The reflection angle θ denotes the angle between the local vertical and the observer. This assumption becomes less accurate when approaching the edges as it only considers direct sunlight at a specific location. In theory, when the local vertical would be perpendicular to the Sun (so parallel to the local plane), no light will directly enter the atmosphere at that location. However, in practice a twilight zone exists where Sunlight is still present, only travelling through part of the atmosphere (so not directly). The alignment error of subsection 3.2.4 in this region is significant too, so both the observations and numerical model show less reliable results near the edges. Consequently, this does not induce a problem in the P_L-comparison of the observations and the numerical model.

The instrumental polarisation variation turns out to be small. The observed variation across the field of view in P_Q and P_U is in the order of magnitude 10^{-3} at most and is small compared to the other error sources (according to [McLean et al., 2017]). The previously mentioned difference in sensitivity of the detector pixels will consequently be small as well. These variations are ignored in the instrumental polarisation across the CCD in [McLean et al., 2017]. Note that Jupiter was always observed at the centre of the field of view.

3.2.3. Estimation of the Photon Noise Error

The photon noise error is determined using equations 3.4 to 3.6 [McLean et al., 2017] for the observations in all wavelength filters. The results are shown in figure 3.2. It can be seen that the noise error is small. From the results it can also be verified that $\sigma_{PL} \approx \sigma_{PQ} \approx \sigma_{PU}$ as is stated in [Bagnulo et al., 2009]. Note that these errors only hold if there are no alignment

and/or distortion errors [McLean et al., 2017].

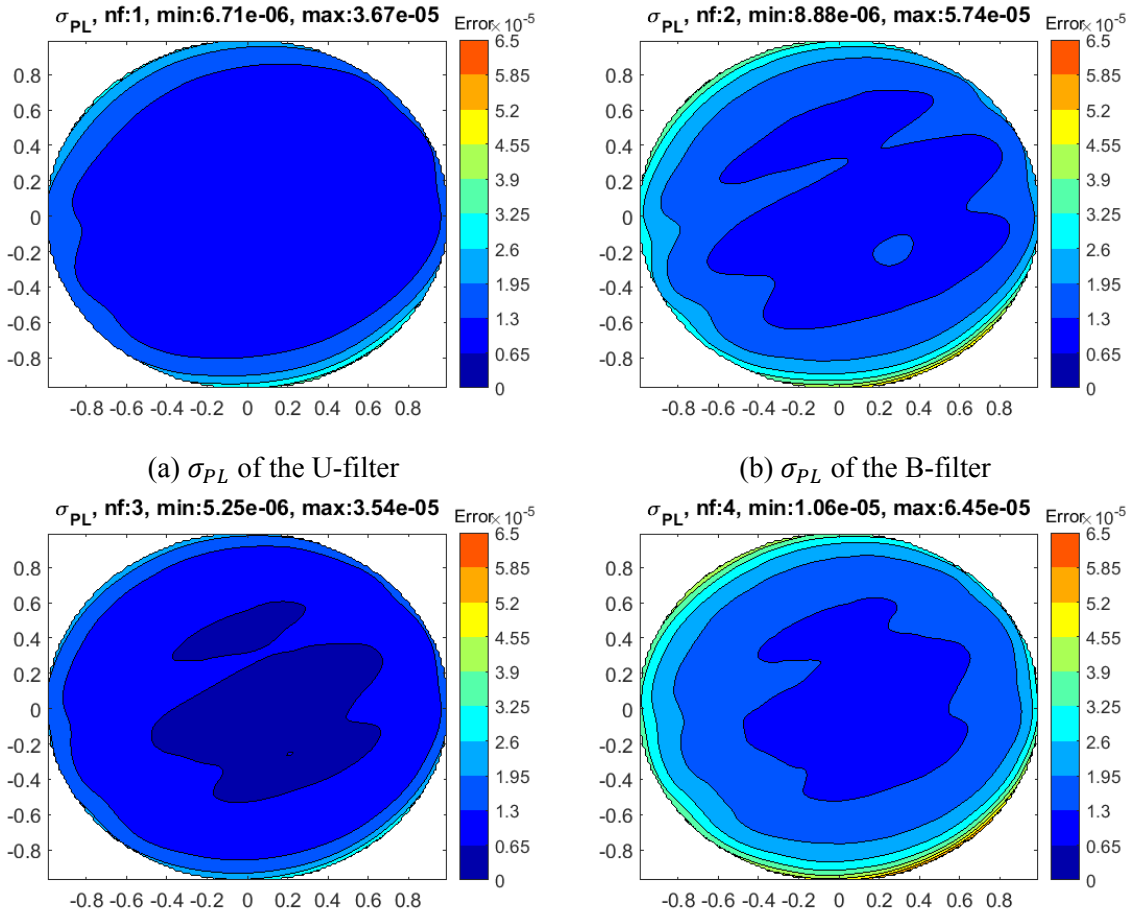

(a) σ_{PL} of the U-filter

(b) σ_{PL} of the B-filter

(c) σ_{PL} of the V-filter

(d) σ_{PL} of the R-filter

Figure 3.2: Photon noise error estimation for the 4 wavelength filters (U, B, V, R)

3.2.4. Estimation of the Alignment Error

The afore-mentioned instrumental error related to distortion and the consequential image alignment due to the slightly different optical paths of the beams of the four strips is estimated. Jupiter's visible disk has a diameter of about 200 pixels on the CCD according to [McLean et al., 2017]. The four signals ($S_{1,2,3,4}$ see Figure 3.1) corresponding to the stokes vector parameters combinations F+Q, F-Q, F+U and F-U are regarded. Note that Q and U of the observations have to be determined by F, P_L and χ of the observations as this data was not provided in the analysis. These signals are all separately shifted one pixel in all directions (top, bottom, left and right) and correspond to the combination of a particular wedge and Wollaston configuration, before deducing the misaligned P_Q and P_U from it (see equations 3.1 and 3.2). With these misaligned P_Q and P_U the misaligned degree of polarisation (P_L) can be determined (see equation 3.3).

Consequently, 16 P_L matrices result, 8 with shifted P_Q-values and 8 with shifted P_U-values. The shifted P_Q-values are combined with the correct P_U-values and vice versa. The 8 P_L matrices corresponding to the shifted P_Q-values are subdivided in shifted values for S_1 and S_2 both

having 4 shifting directions (top, bottom, left, right). The same holds for P_U except that the signals S_1 and S_2 become S_3 and S_4. All 16 P_L matrices are compared to the observations for that particular wavelength filter and the maximum differences are finally used as the alignment error. The result for all the wavelength filters is visualised in Figure 3.3.

In reality, it is possible that the image shifts one pixel in a certain direction, however, the exact alignment error is unknown. Also, the Torino Polarimeter (ToPol) observes through Earth's atmosphere such that the data becomes spread out; the value at one pixel not only comes from data of that particular pixel, which makes it even more difficult to estimate the exact alignment error. The described method is consequently only an estimation to get an impression of the actual alignment error. It is important to notice that the estimated alignment error is a worst-case scenario as the maximum difference for misalignments in all directions for all signals is considered. What can be seen from the estimation though, is that the data in the centre region is less prone to the alignment error than at the edges. This consideration is important when comparing the numerical atmospheric data to the observations later on.

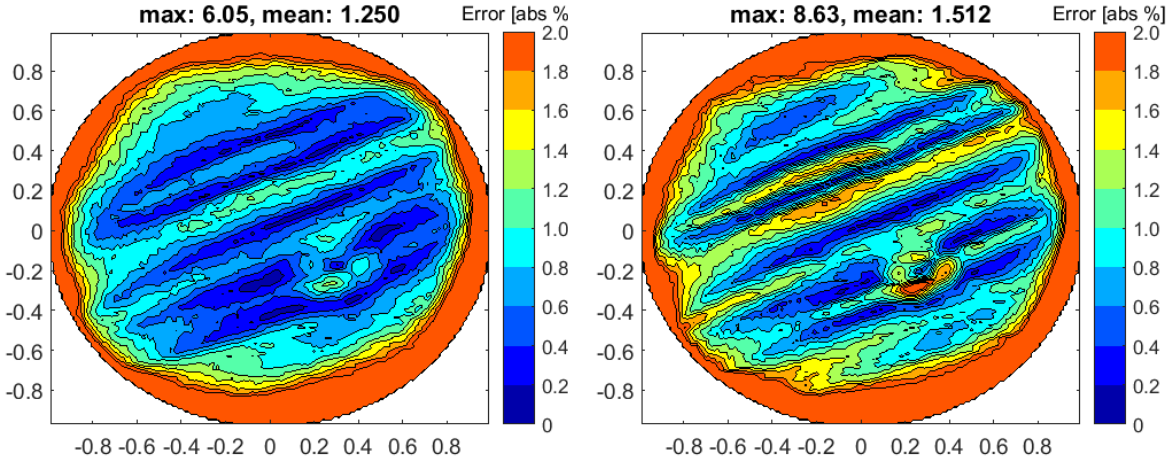

(a) Estimated alignment error on P_L in the U-filter (b) Estimated alignment error on P_L in the B-filter

(c) Estimated alignment error on P_L in the V-filter (d) Estimated alignment error on P_L in the R-filter

Figure 3.3: Alignment error estimation
(as absolute percentage)

3.3. The Wavelength Filters

The observational results can be converted to linear polarisation (P_L) values along the entire Jovian disk. These polarisation results depend strongly on the applied wavelength filter. The data of the numerical model (see chapter 4) is generated per wavelength and the individual Stokes vector elements (F,Q,U) are numerically integrated over the wavelength spectrum of the filter afterwards. These integrated Stokes vector elements are used to determine the linear degree of polarisation according to equation 3.1 to 3.3.

The Torino Polarimeter (ToPol) is equipped with a filter wheel with classical Johnson-Cousins wavelength filters [Devogèle et al., 2017] (the previously mentioned U, B, V and R filters). The filter properties for the Johnson-Cousins wavelength filters are based on [Bessell, 1990] and are stated in Table 3.1. The filter shape can be seen in Figure 3.4 and the data points of the wavelength filters are taken from [Bessell, 1990].

The wavelength points of [Bessell, 1990] are a selection of wavelengths for every wavelength-filter used. As no intermediate data points are provided, this is the λ-resolution used in this analysis. The numerical integration error using these wavelength points is small compared to the previously mentioned error sources.

Table 3.1: Wavelength filter points of [Bessell, 1990]

Filter	λ-range [nm]	λ_{eff} [nm]	$\Delta\lambda$ [nm]	data points
U	300-420	370	5	25
B	360-560	420	10	21
V	470-700	530	10	24
R	550-900	600	10,50*	24

*step of 50nm from 750-900nm

Figure 3.4: Verification of the wavelength filter data points used

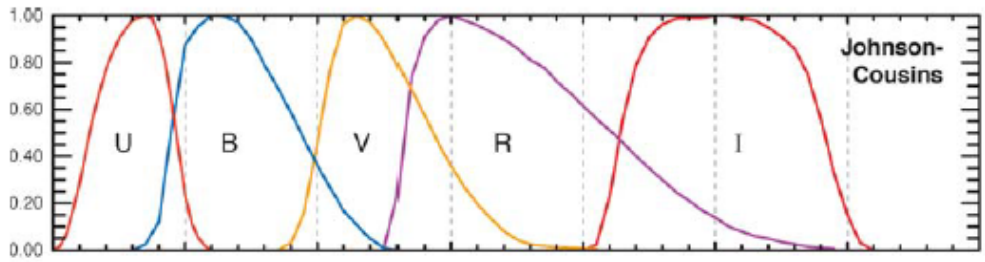

(a) Wavelength filters [Bessell, 2005]

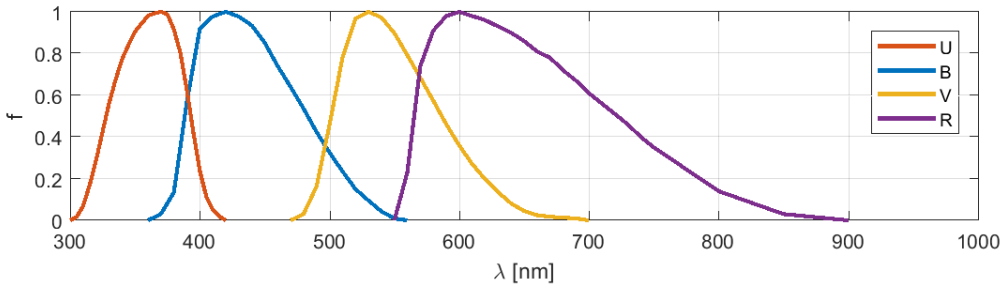

(b) Wavelength filters of data points used ([Bessell, 1990])

4

The Numerical Atmospheric Model

This chapter regards the numerical atmospheric model used to generate the Stokes vector parameters F, Q and U per wavelength per pixel along Jupiter's visible disk. This data generated by the Fortran code is used to find a fit of the observations using the Matlab code as described in chapter 5. The Fortran code which is regularly referred to as the numerical atmospheric model consists of three main parts; the particle properties are determined according to the Mie scattering theory [de Rooij and van der Stap, 1984], followed by the build up of the atmosphere using aerosol layers containing these particles, and finally the Stokes vector parameters F, Q and U are determined per wavelength for every pixel location along Jupiter's visible disk. Afterwards, the additions made to this existing code are elaborated upon. The correct working principle of the Fortran code is verified in section 4.3. An approximation of UV-absorption is discussed in section 4.4 and the single scattering sensitivity analysis to limit the particle property search in chapter 5 is presented in section 4.5. Additional information, such as the relation between the accuracy and computation time is evaluated and addressed in appendix A.

4.1. The Numerical Model (Fortran Code)

The numerical model consists of three main parts; the Mie scattering code, the radiative transfer code and the geometry code, all elaborated upon in the subsections below.

4.1.1. Mie Scattering Code

The Mie scattering code serves to compute the single scattering properties of user-defined particles based on Mie scattering theory (among others in [van de Hulst, 1957] and [de Rooij and van der Stap, 1984]). This Mie scattering code is established by [de Rooij and van der Stap, 1984]. Only single spherical particles are considered as aggregates of particles have to be additionally added to the existing Fortran code. This addition is used to model the polar regions which is done by [Karalidi et al., 2013] and [McLean et al., 2017]. In the mie scattering code, first, the user-defined input variables have to be specified, which among others are the refractive index containing an imaginary part and the wavelength. Then, a size distribution has to be chosen and the particle properties (depending on the chosen distribution) have to be defined. In this case, only the 'two parameter Gamma'-distribution is used, with the two specifying parameters being the effective radius ($r_{eff}[\mu m]$) and the effective variance (v_{eff}:$[0, 0.5]$). The larger the effective variance, the farther the minimum and maximum radius lie from the defined effective radius. The distribution of the particle size is thus taken into account via the

size distribution of the two parameter Gamma, which is determined with equation 4.1 and 4.2 [Hansen and Travis, 1974] (with Γ the Gamma-function).

$$n(r) = C \cdot r^{\frac{1}{v_{eff}}-3} \cdot e^{\frac{-r_{eff}}{r_{eff} \cdot v_{eff}}} \tag{4.1}$$

With:

$$C = \frac{1}{(r_{eff} \cdot v_{eff})^{\frac{1}{v_{eff}}-2} \cdot \Gamma(\frac{1}{v_{eff}} - 2)} \tag{4.2}$$

The next step involves the computation of the scattering matrix, which is shown in equation 4.3. The scattering matrix elements are used later on to determine the expansion coefficients.

$$S(\theta,\lambda) = \begin{bmatrix} a_1(\theta,\lambda) & b_1(\theta,\lambda) & 0 & 0 \\ b_1(\theta,\lambda) & a_2(\theta,\lambda) & 0 & 0 \\ 0 & 0 & a_3(\theta,\lambda) & b_2(\theta,\lambda) \\ 0 & 0 & -b_2(\theta,\lambda) & a_4(\theta,\lambda) \end{bmatrix} \tag{4.3}$$

Then expansion in generalised spherical functions (GSF) is applied. The scattering matrix elements of equation 4.3 are used together with several equations and initial conditions to finally come up with the expansion coefficients ($\alpha_{1-4}, \beta_{1-2}$). This procedure is described in detail in [de Rooij and van der Stap, 1984].

These expansion coefficients describe the single scattering properties of the distribution of particles with the user-defined input values over the defined scattering angle (θ) range. This information is written to a Mie-output file and is used as input for the radiative transfer code.

4.1.2. Radiative Transfer Code

The upper atmosphere can be built using horizontal homogeneous locally parallel layers in this part of the code. The parallel layers are defined by a top and bottom pressure as indicated in Table 4.1 (data from [Lindal, 1992] and [West et al., 1986]). In this analysis the bottom of the atmosphere is regarded a black surface which means that all light reaching this point will be absorbed, which corresponds to a surface albedo of 0.0. All pressure layers contain gaseous molecules and optional aerosol layers. The latter use the single scattering properties of the expansion coefficients outputted by the Mie-code. This atmospheric representation is used in the doubling-adding algorithm [Rossi et al., 2018] (as described in [de Haan et al., 1987]) to find the Fourier coefficients to come up with the Stokes vector parameters F, Q and U.

This doubling-adding algorithm (DAP) requires input parameters as, among others, the optical thickness (see section 4.2.1 and 4.2.2), the single scattering albedo (a) and the surface albedo. Finally, the combined expansion coefficients (accounting for both multiple and single scattering, the latter coming from the Mie code) form an important parameter that is used in the doubling-adding algorithm.

The output contains a Fourier coefficient file, including several types of scattering and absorption properties, for both the defined aerosol layers and the gaseous layers.

Table 4.1: Pressure layers (data from [Lindal, 1992] and [West et al., 1986])

Layer number	Bottom pressure (bar)	Top pressure (bar)	Δp (bar)
1	5.623	4.217	1.406
2	4.217	3.162	1.055
3	3.162	2.371	0.791
4	2.371	1.778	0.593
5	1.778	1.334	0.444
6	1.334	1.000	0.334
7	1.000	0.7499	0.2501
8	0.7499	0.5623	0.1876
9	0.5623	0.4217	0.1406
10	0.4217	0.3612	0.1055
11	0.3612	0.2371	0.0791
12	0.2371	0.1778	0.0593
13	0.1778	0.1334	0.0444
14	0.1334	0.1000	0.0334
15	0.1000	0.0100	0.0900
16	0.0100	0.0001	0.0099

Note that the bottom of layer 1 is bounded by a black surface (approximation)(i.e all light that reaches this point is assumed to be absorbed)

4.1.3. Geometry Code

The geometry code (GEOS) uses the Fourier coefficients obtained by the radiative transfer code to determine the Stokes vector parameters F, Q and U along Jupiter's entire visible disk. This is done using the local reflection matrix R. This part of the Fortran code does not contain additions made in this analysis (besides the implemented loops to write the output to the different output files).

By defining the planetary phase angle (α) and using the number of pixels along the equator, the user (indirectly) defines the local angles. The local geometry angles comprise the illumination angle θ_0, which is the angle between the incident sunlight and the local vertical, the reflection or viewing angle θ is the angle between the local vertical and the reflected light towards the observer and the azimuth difference angle $\phi - \phi_0$ is the angle between the two vertical planes containing the directions of propagation of the reflected and incident light [Rossi et al., 2018].

The locally reflected flux vector (F) is defined by equation 4.4 [Hansen and Travis, 1974].

$$\vec{F}(\mu, \mu_0, \phi - \phi_0) = \mu_0 \vec{R}(\mu, \mu_0, \phi - \phi_0)\vec{F}_0 \tag{4.4}$$

With F_0 the incident (unpolarised) flux vector, R the (4x4) planetary scattering matrix and $\mu_0 = cos(\theta_0)$ and $\mu = cos(\theta)$.

As the incident light is assumed to be unpolarised ($\vec{F}_0 = [F_0, 0, 0, 0]$), only the first column of the reflection matrix (denoted as R_1) is used, such that equation 4.4 can be written to equation 4.5.

$$\vec{F}(\mu, \mu_0, \phi - \phi_0) = \mu_0 \vec{R}_1(\mu, \mu_0, \phi - \phi_0)\vec{F}_0 \tag{4.5}$$

Moreover, circular polarisation is neglected such that the fourth element (corresponding to V) can be omitted and only the first three elements of the first column of R (corresponding to F, Q and U) are used. This R_1, for given local angles, can be determined to finally come up with the Stokes vector parameters F, Q and U which are then given at the centre of every pixel location (corresponding to these local angles). These F, Q and U are finally written to the output file of the geometry program.

The degree of linear polarisation (P_L) could be determined directly with the geometry code too. However, as the code only regards one wavelength at a time, the output file would then only contain the value for a specific wavelength. As wavelength filters are used, the Stokes vector parameters have to be integrated over the entire wavelength range before computing P_L from it. Note that this holds for the observations as well, where first the Stokes vector parameters are deduced from the signals per wavelength filter before obtaining P_L. Note that in this analysis the observed P_L result is already provided.

To get an as good as possible representation of the observations using the numerical model, this same procedure is used. As the wavelength filters are constructed outside the Fortran code, the only required output parameters are the Stokes vector parameters F, Q and U per wavelength for all pixels along Jupiter's visisble disk.

A Matlab program is created to construct the wavelength filters, to match the Stokes vector parameters to the exact pixel location on the visible disk (this is not done in the geometry program) and to compare the results of the numerical model with the observations. This Matlab code will be discussed in chapter 5.

4.2. Additions to the Numerical Model

This section sheds light on the additions to the already existing numerical model written in Fortran. The main additions consist of making the optical thickness and the refractive index of the gas a function of wavelength and the implementation of methane absorption. Besides the main additions, loops have been implemented to loop through the wavelength and optional other parameters. The input-output flow is added as well, such that the program can be run in one go. Note that similar additions to the existing numerical model are performed before, among others in [McLean et al., 2017] and [Fernández Jiménez, 2018].

4.2.1. Optical Thickness

The optical thickness of the atmospheric layers is one of the main factors influencing the stokes vector parameters and thereby the polarisation state. The optical thickness can be subdivided into two main parts with a contribution of both the aerosol layers (b^a) and the gaseous layers (b^m), which both have a component from scattering (sca) and absorption (abs). The optical thickness is defined in the numerical model as stated in equation 4.6.

$$b = b^a + b^m = b^a_{sca} + b^a_{abs} + b^m_{sca} + b^m_{abs} \tag{4.6}$$

The aerosol components (b^a_{sca},b^a_{abs}) are based on the input parameter of the total aerosol optical thickness ($baer$ in the code). The molecular components (b^m_{sca},b^m_{abs}) depend on the wavelength and the amount of gaseous absorption and can be defined specifically for the characteristics of Jupiter's atmosphere.

Molecular Scattering Optical Thickness :

The molecular scattering part (b^m_{sca}) can be determined with equation 4.7 [Hansen and Travis, 1974] and the absorption part is dealt with in section 4.2.2. The equation is based on the assumptions of hydrostatic equilibrium and a constant gravitational acceleration with altitude.

$$b^m_{sca}(\lambda) = N_{gas}(\Delta p) \cdot \sigma_{sca}(\lambda) = \frac{N_A \cdot \Delta p}{\mu_{atm} \cdot g} \cdot \frac{24\pi^3}{N_L^2} \frac{(n^2-1)^2}{(n^2+2)^2} \frac{6+3\delta}{6-7\delta} \frac{1}{\lambda^4} \tag{4.7}$$

The parameter N_{gas} denotes the column number density of the gas molecules [m^{-2}], which indicates the amount of gas molecules present in an atmospheric column with a horizontal cross-section of $1m^2$. σ_{sca} is the scattering cross section of the gas molecules [m^2] which scales with λ^{-4} and is an indication for the amount of scattering of the molecules. The wavelength dependence of the refractive index (n) is discussed later on.

When writing out these two terms, the only variables that remain are the pressure difference between the top and bottom of the atmospheric layer (Δp), the wavelength (λ) and the refractive index of the gas (n) that is a function of wavelength. The Loschmidt number (N_L) depends on the standard temperature and pressure (STP) conditions set. The other parameters are constants for Jupiter's atmosphere and are stated in Table 4.2. The value of the mean molecular weight comes from data of [Atreya et al., 2003], for g the mean value of Jupiter from [Lissauer and de Pater, 2013] is used, for the refractive index the value for hydrogen at the chosen STP conditions (T=0°C and p=1atm) is used and finally for δ the value is based on a mostly hydrogen containing atmosphere [Hansen and Travis, 1974].

Table 4.2: Optical thickness input parameters

Parameter	Symbol	Value	Unit
Avogadro's constant	N_A	$6.022 \cdot 10^{23}$	$mole^{-1}$
Mean molecular atmospheric weight	μ_{atm}	$2.22 \cdot 10^{-3}$	$kg \cdot mole^{-1}$
Jupiter's gravitational acceleration	g	25	ms^{-2}
Refractive index of the gas	n	see figure 4.1	-
Depolarisation constant of the gas	δ	0.02	-

The Wavelength Dependence of the Refractive Index :

The wavelength dependence of the refractive index of the hydrogen gas, which is a factor to consider for the parameter n of equation 4.7, is determined with equation 4.8 from [Peck and Huang, 1977]. Note that this equation holds for a wavelength (λ) given in μm and that this equation can be rewritten such that only the refractive index (n) appears on the left-hand side of the equation.

$$10^6(n-1) = \frac{14895.6}{180.7 - \lambda^{-2}} + \frac{4903.7}{92 - \lambda^{-2}} \tag{4.8}$$

The refractive index of hydrogen gas as a function of wavelength is shown in figure 4.1. This implementation is required for the correct determination of the molecular scattering optical thickness (equation 4.7) where the refractive index (n) of hydrogen gas is a function of wavelength.

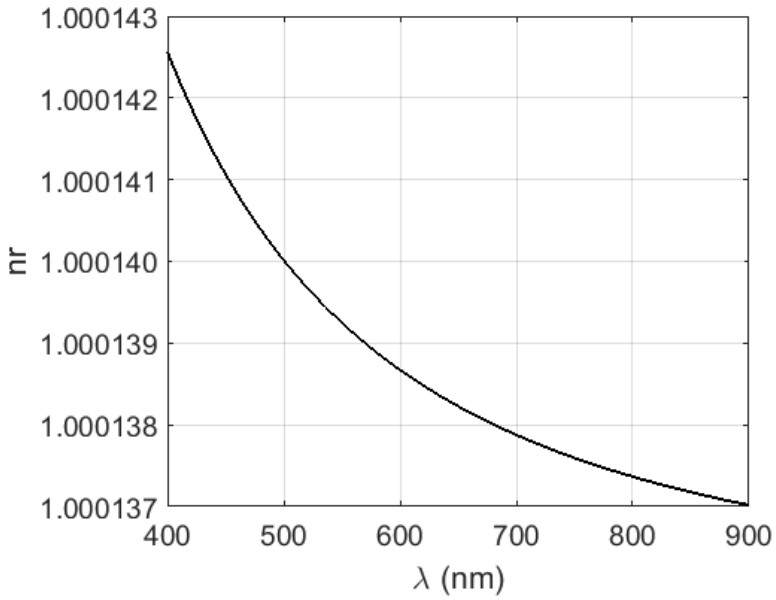

Figure 4.1: Refractive index of hydrogen gas as a function of wavelength based on equation 4.8 of [Peck and Huang, 1977]

Aerosol Optical Thickness :

The determination of the aerosol optical thickness (b^a) is similar to that of b_{sca}^m dealt with previously. It is the product of the aerosol column number density (N_a) and the extinction cross-section (σ_{ext}), as shown in equation 4.9.

$$b^a = N_a \cdot \sigma_{ext} \tag{4.9}$$

The extinction cross-section is often defined using the particle scattering efficiency (Q_{ext}) and the geometrical cross-section ($G = \pi r^2$) as shown in equation 4.10.

$$\sigma_{ext}(\lambda) = Q_{ext}(\lambda) \cdot G(r) \tag{4.10}$$

The extinction cross-section therefore depends on both the wavelength (λ) and the particle size (r). As both the particle scattering efficiency (Q_{ext}) and the geometrical cross-section (G) are computed by the mie-code, the extinction cross-section (σ_{ext}) is determined using equation 4.10. Using the fact that the aerosol column number density (N_a) is independent of wavelength and that b^a is a user defined input, b^a can be determined w.r.t. one wavelength. In order to keep b^a as close to the user defined input value as possible for all wavelengths, b^a can be defined best for a wavelength close to the mid-wavelength of the filter. This is preferred to get an as good as possible indication of the optical thickness value. Therefore, the equation to compute b^a is shown below (equation 4.11) and the reference wavelength (λ_0) is chosen as 550nm as it is approximately in the middle of the total wavelength-range (300-900nm) and it is in conformance with [McLean et al., 2017].

$$b_{\lambda 1}^a = b_{\lambda 0}^a \cdot \frac{\sigma_{ext1}(\lambda)}{\sigma_{ext0}(\lambda)} \tag{4.11}$$

When b^a is known, the scattering and absorption contributions can be determined using equation 4.14 and 4.15, where the single scattering albedo (a) is defined in equation 4.12.

$$a = \frac{\sigma_{sca}}{\sigma_{ext}} \tag{4.12}$$

$$\sigma_{ext} = \sigma_{sca} + \sigma_{abs} \tag{4.13}$$

$$b_{sca}^a(\lambda) = a(\lambda) \cdot b^a \tag{4.14}$$

$$b_{abs}^a(\lambda) = (1 - a(\lambda)) \cdot b^a \tag{4.15}$$

4.2.2. Methane Absorption

Jupiter's geometric albedo is shown in Figure 4.2 with the wavelength (λ in μm) on the x-axis and the geometric Albedo (A_g) on the y-axis. The geometric Albedo is the fraction of the actual reflected flux (at $\alpha = 0°$) over the flux that a white, isotropically reflecting visible disk would reflect [Lissauer and de Pater, 2013].

From figure 4.2 it can be seen that when the amount of methane absorption increases, the geometric albedo decreases as light that has been absorbed cannot be reflected. Note that methane absorption starts from about $\lambda = 520$nm onwards.

The wavelength filter boundaries are indicated in their respective colours. It can be observed that absorption is most dominant in the R-filter, where methane is the most influencing absorbing gas.

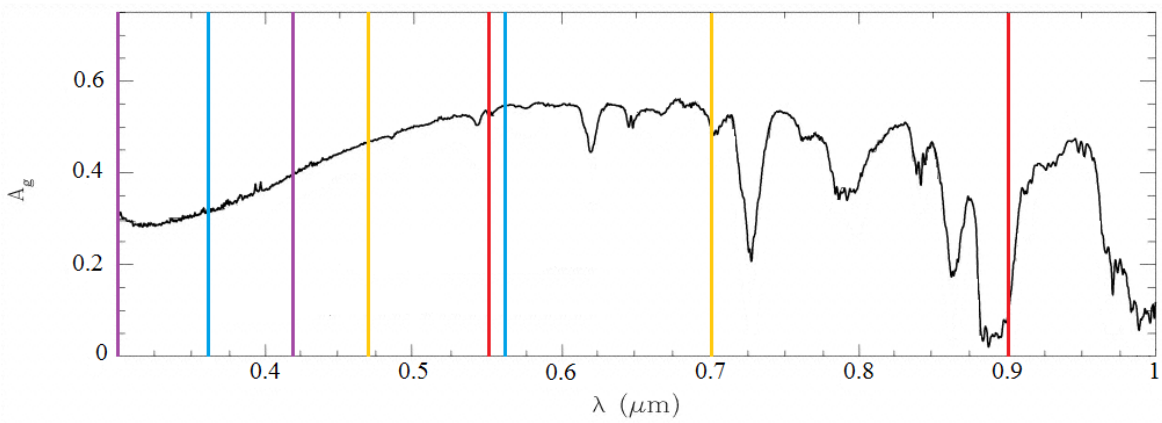

Figure 4.2: Jupiter's geometric albedo
(figure adapted from iopscience.iop.org)

Methane absorption band implementation :

The molecular absorption optical thickness (b^m_{abs}) is a measure of the amount of absorption in a particular atmospheric layer at a particular wavelength. The methane absorption can be taken into account by means of equation 1 of [Sun and Rikus, 1999], which is stated in equation 4.16 and rewritten to the parameter symbols of [Sánchez-Lavega, 2011].

$$T(\lambda, a) = \sum_{i=1}^{n} w_i e^{-k_i(\lambda)a} \tag{4.16}$$

With n the number of absorption coefficients, w_i denoting the weight factors, k_i the absorption coefficients [(km-am)$^{-1}$] and a is the absorber or column abundance [km-am]. An amagat (am) represents the ratio of the number density of particles at a given temperature and pressure to the number density of the reference standard temperature and pressure (STP) [Sánchez-Lavega, 2011]. The absorber or column abundance is stated in equation 4.17 [Sánchez-Lavega, 2011]. This equation assumes hydrostatic equilibrium as well as that the volume mixture ratio (x_{VV}) and gravitational acceleration (g) remain constant with altitude.

$$a = \frac{N_A}{N_L} \frac{x_{VV}}{\mu_{atm} \cdot g} p = \frac{N_{gas}}{N_L} \cdot x_{VV} \tag{4.17}$$

The parameter N_{gas} is the column number density of the gas molecules $[m^{-2}]$. N_L denotes the Loschmidt number $[m^{-3}]$; the number of particles of an ideal gas in a given volume (number density) at STP (standard temperature and pressure). The parameter p denotes the pressure difference of the top and bottom of the atmospheric layer in bar. The STP conditions are defined as a standard temperature of 273K (0° Celsius) and a standard pressure of 1atm. The corresponding Loschmidt number can be determined as $2.479 \cdot 10^{25} m^{-3}$. The ratio (N_{gas}/N_L) denotes the column height (in meter) of all atmospheric gases when brought to STP. x_{VV} denotes the generic mixing ratio (the mixing ratio of the absorbing gas; e.g. the volume fraction of the absorbing gas), which is $2.1 \cdot 10^{-3}$ for methane (CH_4). The rest of the constant parameter values are indicated in table 4.2. The column abundance 'a' then denotes the column height of the methane molecules in the atmosphere when brought to STP. This is multiplied with the methane absorption coefficients which indicate the absorption per meter of column to finally indicate the total amount of methane absorption.

The relation for the optical thickness is stated in equation 4.18 [Sánchez-Lavega, 2011].

$$b_{abs}^{m} = k_i \cdot a = k_i \frac{N_{gas}}{N_L} \cdot x_{VV} \tag{4.18}$$

According to equation 4.16 and 4.18, the optical thickness (b) relates to the transmission function (T) as shown in equation 4.19. Note that the weight factors depend on the number of coefficients (nc), for nc=1, $w_1 = 1$, for nc=2, $w_1 = w_2 = 0.5$ and for nc=4, $w_1 = w_4 \approx 0.174$, $w_2 = w_3 \approx 0.326$ [Tomasko et al., 2008]. So first the Transmission function (T) is determined before substituting the result in equation 4.19.

$$b_{abs}^{m} = -ln(T(\lambda, a)) \tag{4.19}$$

With equation 4.19, b_{abs}^{m} for the 1, 2 and 4-term absorption coefficients from [Karkoschka and Tomasko, 2009] can be determined according to the previously mentioned weight factors.

4.2.3. Refractive index

As mentioned previously in section 2.3, Jupiter's aerosol layers have no clearly defined boundaries and therefore vary with location and pressure. Previous research agrees on Jupiter's different cloud layer composition. Three cloud layers are expected being a water (H_2O), ammonium-hydrosulfide (NH_4SH) and ammonia (NH_3) cloud (in sequence of decreasing pressure or increasing altitude) [West et al., 2004]. Due to the low temperature in the upper part of the atmosphere, all three mentioned clouds are expected to be ice clouds. Also, a haze layer overlaying the highest (ammonia-ice) cloud is expected (see among others [West et al., 2004], [McLean et al., 2017]). Polarisation is sensitive to the upper atmospheric layers only such that the effect of the lower clouds is small, especially when the optical thickness of the higher clouds is high. Therefore, it is decided to use one cloud layer and a haze layer in the analysis, the latter is in conformance with previous research (among others [Sromovsky and Fry, 2002] and [West et al., 2004]). The composition of these so-called aerosol layers is fundamental as it closely relates to the particle properties. The highest cloud deck on Jupiter is expected to consist of ammonia-ice and its refractive index has been obtained in the past using laboratory experiments as described in [Romanescu et al., 2010].

Previous atmospheric models representing Jupiter's atmosphere by among others [McLean et al., 2017] and [Fernández Jiménez, 2018] use a refractive index of 1.42 for the ammonia-ice (NH_3) cloud which originates from [Martonchik et al., 1984]. Other research of [Romanescu et al., 2010] resulted in a value of about 1.49 in the temperature range 80-100K at a wavelength of 632.8nm, however, the temperature of Jupiter's ammonia-ice cloud is expected to be around 140K [West et al., 1986]. The refractive index for this same ammonia-ice cloud used in this analysis is chosen in conformance with the afore-mentioned previous research as 1.42.

The composition of the stratospheric haze is yet unknown, consequently, different values have been used in previous research. [McLean et al., 2017] uses a refractive index for the haze of 1.50 based on [Stoll, 1980], while [Fernández Jiménez, 2018] regards a value of 1.66 according to [Sromovsky and Fry, 2002]. In this analysis both the smaller particles of [McLean et al., 2017] and the larger particles of [Fernández Jiménez, 2018] are used as initial particles such that both refractive indices of the haze are evaluated.

Another aspect to consider is the fact that the refractive index varies with wavelength. Implementing this variation in the numerical model will make it more accurate. However, the variation of refractive index with wavelength for the proposed cloud and haze has not yet been used in previous research of [Stam et al., 2004], [McLean et al., 2017] and [Fernández Jiménez, 2018]. Up until now, the refractive index value is only known at specific wavelength values via laboratory experiments (see for example [Romanescu et al., 2010]). Consequently, the wavelength dependence of the refractive index of the aerosol layers cannot be taken into account in this analysis.

4.3. Verification of the Additions to the Numerical Model

The additions to the numerical model elaborated upon previously have to be verified to show that the Fortran code is working as expected. This verification is done using figure 4 of [Stam et al., 2004] which is shown in sub-figure 4.3c. The figure shows the disk-integrated flux and degree of linear polarisation as a function of wavelength for a phase angle of 90° for three Jupiter-like exoplanets. These three Jupiter-like exoplanets are referred to as model 1, 2 and 3 and consist of only molecules, molecules with a tropospheric cloud layer and molecules with a tropospheric cloud layer and a stratospheric haze layer respectively. The known parameter values used for this figure are stated in table 4.3.

Table 4.3: Parameter values for the verification of figure 4 of [Stam et al., 2004]

Parameter	Value	Unit
$r_{eff,c}$	1.0	μm
$v_{eff,c}$	0.1	-
nrc	1.42	-
$r_{eff,h}$	0.5	μm
$v_{eff,h}$	0.01	-
nrh	1.66	-
middle wavelength	0.700	μm
b^m_{sca}	21.47^1 , 0.51^3	-
baerc	6^2	-
baerh	0.25^2	-
surface albedo	0.0	-
atmospheric mixing ratio of CH_4	0.18	%

[1]: at $\lambda = 0.4\mu m$, [2]: at $\lambda = 0.7\mu m$ and [3]: at $\lambda = 1.0\mu m$

The parameter value b^m_{sca} is 21.47 at λ =0.4μm and 0.51 at λ =1.0μm. When adapting b^m_{sca} of the numerical model to these values it can be shown that both the Flux and P_L-curves match the result of [Stam et al., 2004] visualised in sub-figure 4.3c well. The only notable difference occurs for P_L near λ =0.9μm, where the result of this analysis shows more oscillatory behaviour and higher P_L-values for model 3 only. These P_L oscillations for both analyses possibly relate to the low Flux value at this wavelength. This might be caused by a lower value for the number of Gaussian points used in this analysis or by the definition of the disk integrated P_L (with or without using U in the calculation, see appendix A). Unfortunately, this difference cannot be investigated in more detail due to a lack of information of the parameter values used in [Stam et al., 2004]. Note that the figures generated with the code of this analysis shows the wavelength range of 0.4 to 0.9μm (instead of 0.4 to 1.0 μm) as that is the wavelength range required to construct the wavelength filters. Verification of the wavelength range from 0.9 to 1.0μm therefore does not add value as this part does not influence the results. Also, the high phase angle of 90° results in very high P_L values such that the effect of this possible deviation is much smaller for the P_L comparison presented in this analysis as the phase angle is 10.73°. For the verification of this figure the imaginary part of the refractive index (nri) which is a measure for the absorptiveness of the aerosol particles is unknown. Consequently, it is expected that a value of zero (or close to zero) is used to create sub-figure 4.3c. In the comparison a nri-value of $1 \cdot 10^{-7}$ is used as a value of zero does not work out in the data generation of the Fortran code. Note that the same methane absorption coefficients used in [Stam et al., 2004] from

[Karkoschka, 1994] are used for this verification to verify the methane absorption peaks and sinks.

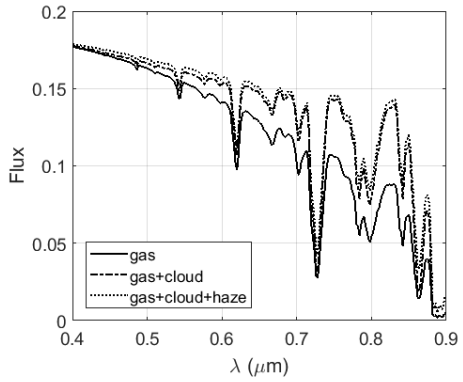

(a) Flux of numerical model

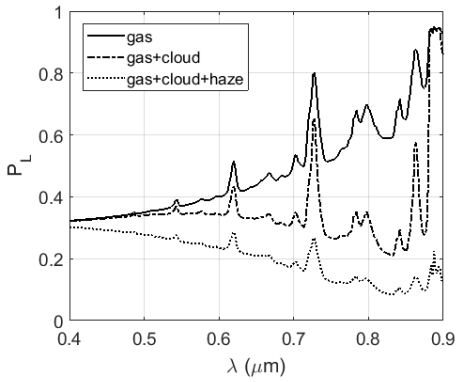

(b) P_L of numerical model

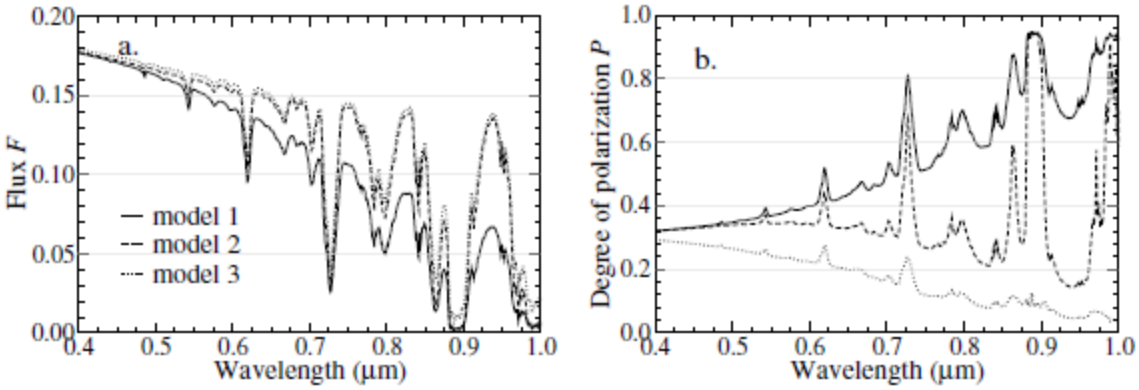

(c) Flux and P_L from Figure 4 of [Stam et al., 2004] (horizontal grid lines added)

Figure 4.3: Verification of Figure 4 [Stam et al., 2004]

This analysis shows that the Fortran code with made additions works as expected. This implies that the methane absorption of sub-section 4.2.2 is implemented well as the absorption peaks (P_L) and sinks (F) have the same height and depth for both figures. The correct implementation of the molecular scattering optical thickness (b^m_{sca}) cannot be verified with 4.3c as the values of this figure are used for verification instead of the values applying for Jupiter in this analysis. This parameter has been verified before using data for other planetary bodies using [Stam, 2015]. Moreover, the implementation of the varying optical thickness (baer) with wavelength and the refractive index of hydrogen gas with wavelength are verified with help of this figure.

4.4. Absorption at lower wavelength

It can be observed from the geometric albedo (the black curve of Figure 4.4) that besides absorption due to methane (520-900nm), additional absorption is present at lower wavelength. About this so-called UV-absorption much is unknown, among others the source. With the current knowledge it is not possible to take this UV-absorption accurately into account in this analysis. Therefore an approximation of this UV-absorption is considered in this analysis.

As mentioned previously, the methane absorption is taken into account in the molecular absorption optical thickness (b_{abs}^{m}) as it is gaseous absorption. However, it is yet unknown what exactly causes the absorption at lower wavelengths. Therefore, two scenario's are regarded; absorption by the gas only (again through b_{abs}^{m}) and absorption caused merely by the aerosol layers using the imaginary part of the refractive index (nri). The second approach will be used in this analysis as it is expected that when gaseous absorption would be present, it can be linked back to specific gasses causing this. Moreover, not much is known about the absorption potential of the aerosols such that the absorption at the lower wavelengths could be caused by it. Therefore, it is in the end chosen to use absorption by the aerosol layers to approximate the UV-absorption. A combination of gaseous and aerosol absorption is possible but this greatly complicates the problem and the contribution of both sources is difficult to establish.

First, to have a better comparison with the geometric albedo, a model lying both close to the data points (from [Karkoschka, 1998]) and to the parameter values from fitting the observations so far is searched for. The result is shown in Figure 4.4 for the parameters; $rc_{eff} = 0.5\mu m$, $rh_{eff} = 0.2\mu m$, $vc_{eff} = 0.05$, $vh_{eff} = 0.01$, plc=6, plh=13, baerc=50, baerh=0.3 and nric=nrih=(2e-4)i. This model lies close to the models found by [McLean et al., 2017] and is therefore a good starting point to find a good match of the geometric albedo data of [Karkoschka, 1998]. It can be seen that this model matches the geometric albedo curve reasonably well (figure 4.4). Still some differences occur but to exactly match the geometric albedo curve the exact atmospheric parameters have to be known.

Consequently, this model will be used to approximate the absorption at lower wavelength (300-520nm) in case of gaseous absorption via b_{abs}^{m} and due to aerosol absorption via the parameter nri. Note that the measured geometric albedo of Jupiter (data of [Karkoschka, 1998]) contains the actual variations in atmospheric parameters as the pressure layer of the cloud, the optical thickness of the haze, etc. while the result presented here contains one value per parameter as mentioned previously. Only the haze optical thickness and the pressure layer at which the cloud is present vary significantly, such that when taking average values (plc=6, baerh=0.3) the variations can be approximated. Therefore, this analysis can only be used to get a first order approximation of the absorption properties at lower wavelength. As the origin of the UV-absorption is still unknown, it is difficult to derive more accurate absorption properties and take this aspect into acount more accurately.

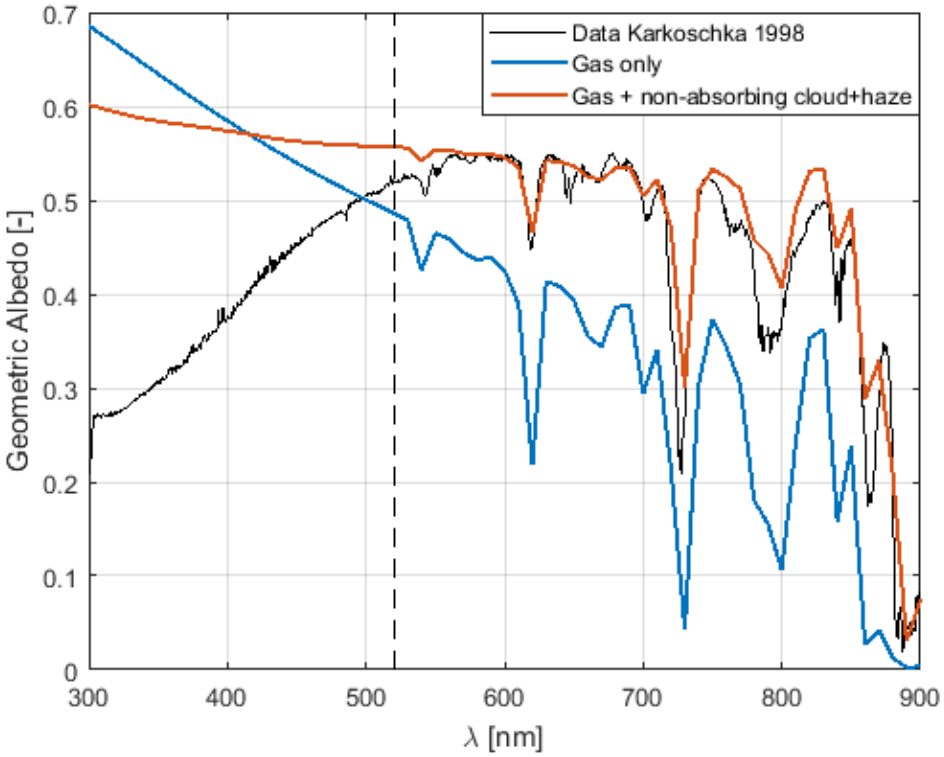

Figure 4.4: Jupiter's geometric albedo comparison with numerical model 4 without UV-absorption

Scenario 1 :

Scenario 1 regards absorption by the gas layers only. This scenario is not used in this analysis but still provides useful information on how to approximate gaseous absorption (via b_{abs}^{m}) when the absorption coefficients are unknown. The new b_{abs}^{m} can be derived using equation 4.18, with the relation of 'a' from equation 4.17. In this case, the only variable in the equation is the pressure difference between the top and bottom of the pressure layer (Δp) and the result is stated in equation 4.20 and 4.21. All relevant parameters in the equations are addressed in section 4.2.2. The parameter C_1 denotes the absorption coefficients which are unknown as the absorber at lower wavelengths is yet unknown. Therefore, an estimation is made for the constant C as the rest of the parameters it consists of (equation 4.21) is constant too. This estimation is based on the difference between the red and black curve of Figure 4.5.

Thus, the latter numerical model (red line of Figure 4.4) is used to convert the difference in geometric albedo (Δga) between the continuum (no absorption) and the data curve from [Karkoschka, 1998]. In the end, the blue curve of Figure 4.5 results. The coefficients approximate the geometric albedo data curve closely and could therefore be used to incorporate gaseous absorption at lower wavelength. The approximation is used that the absorption is divided proportionally to the pressure difference of all the pressure layers in this case. The value for b_{abs}^{m} can be determined for non-proportional (pressure) cases as well, however, it is difficult to estimate in which layers more absorption would be present. Therefore, this proportional pressure case is regarded in this scenario.

$$b_{abs}^{m} = \Delta p \cdot C \qquad (4.20)$$

$$C = \frac{N_A \cdot X_{VV}}{\mu_{atm} \cdot g \cdot N_L} \cdot C_1 \qquad (4.21)$$

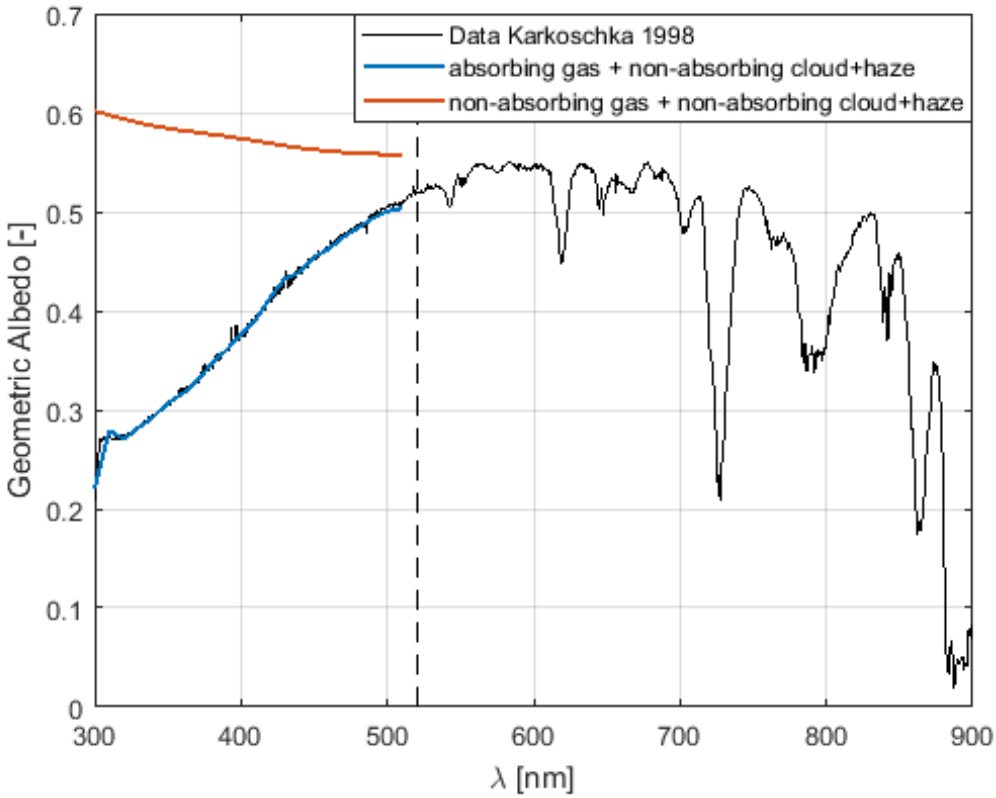

Figure 4.5: Jupiter's geometric albedo of numerical model 4 with and without gaseous UV-absorption

Scenario 2 :

The second approach, absorption caused by the absorbing potential of the aerosols, is used to approximate UV-absorption in this analysis. This absorbing potential is represented in the imaginary part of the refractive index (nri), which is estimated as 2e-4 for the wavelength range of 520-900nm in this analysis to fit the geometric albedo curve as shown in figure 4.6. From the continuum of the used model (the blue curve of Figure 4.4 from 300-520nm) it can be seen that the geometric albedo increases with decreasing wavelength. Consequently, nri has to increase with decreasing wavelength as well to make up the effect. It turns out that when modelling nri of the haze (nrih) higher than nri of the cloud (nric) a close approximation to the geometric albedo curve of [Karkoschka, 1998] can be found. The resulting geometric albedo of the model with and without absorption in the wavelength range 300-520nm is shown in Figure 4.6. The geometric albedo difference with the data at 520nm is kept over the entire range from 300-520nm to model the absorption as good as possible. When a difference in geometric albedo is present at 520nm, and the curves are exactly matched at 510nm (the wavelength point before) too much absorption would be considered as the jump back from 520nm to 510nm would induce a very high absorption at 510nm. Note that a $\Delta\lambda$ of 10nm is used as all the wavelength filter points are captured then. The nri-value is linearly increasing to a maximum at 300nm for both the cloud and the haze, which results in a maximum nric of 5e-3 and nrih of 0.1. The ranges therefore become nric: [2e-4, 5e-3] and nrih: [2e-4 0.1]. Again, it has to be noted that this UV-absorption approximation is based on the geometric albedo value for one combination

of atmospheric parameter values only. The geometric albedo data of [Karkoschka, 1998] takes into account the variation in atmospheric parameters such that this section only addresses a fist order approximation of UV-absorption. Also, a second drawback of this approximation is that a variable nri-value cannot be linked to a specific composition of the cloud and haze as a specific cloud and haze composition corresponds to a certain nri-value. Despite the fact that this analysis only regards an approximation, it is a more accurate representation of reality than not regarding UV-absorption at all.

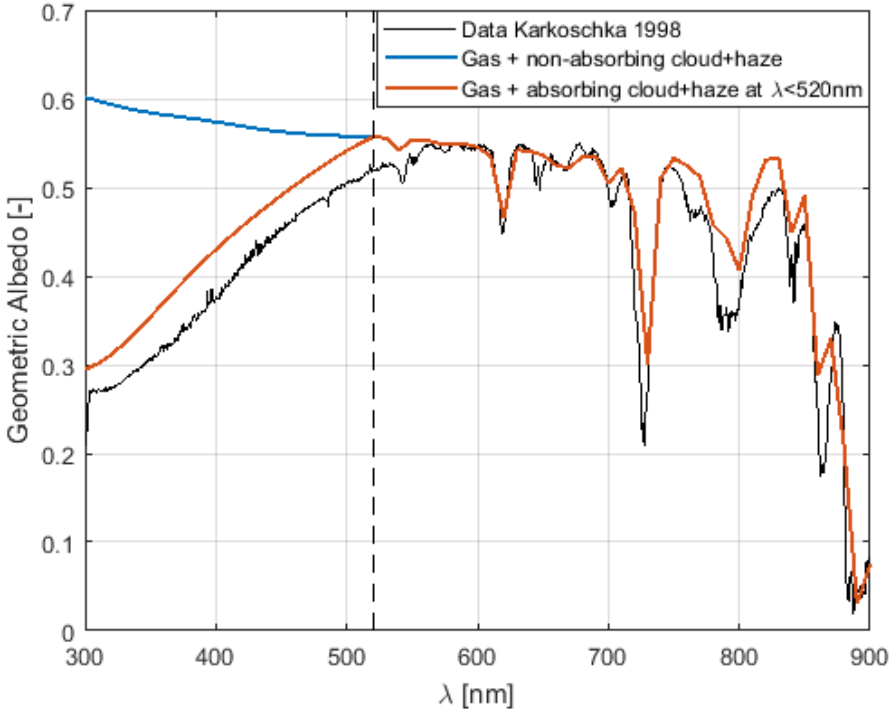

Figure 4.6: Jupiter's geometric albedo of numerical model 4 with and without UV-absorption in the aerosol layers

4.5. Single Scattering Sensitivity Analysis

In the numerical model (see section 4.1), the Mie scattering code (see subsection 4.1.1) is responsible for the single scattering properties of the spherical particles used to build up the atmosphere from. A preliminary analysis regarding these single scattering properties is presented which might give a possible starting point for the particle properties that can be used in the fitting procedure later on. Moreover, it helps understand better what the effect of different particle properties on the single scattering degree of polarisation is.

The input parameters of the Mie code, which determine the particle's single scattering properties (with the chosen 2-parameter Gamma size distribution) are the particle's effective radius (r_{eff}) and variance (v_{eff}) as well as the refractive index (nr, including an imaginary part which is set to $1e^{-7}$ in this particular analysis). Additionally, the wavelength (λ) and the scattering angle (θ) influence the single scattering F and P_L.

The single scattering properties can be derived from the scattering matrix S (see equation 4.3) using equation 4.22 where C is a constant factor [van de Hulst, 1957], S the scattering matrix and the first and last part denote the Stokes vector of the scattered light beam and the incident light beam respectively [Hovenier and van der Mee, 1983]. The single scattering total flux and degree of linear polarisation can be determined from S as a_1 and $-b_1/a_1$ respectively.

$$\begin{bmatrix} F_{sc} \\ Q_{sc} \\ U_{sc} \\ V_{sc} \end{bmatrix} = C \cdot S \begin{bmatrix} F_i \\ Q_i \\ U_i \\ V_i \end{bmatrix} \tag{4.22}$$

The single scattering total flux (F_{ss}) and degree of linear polarisation ($P_{L,ss}$) are determined as a function of scattering angle (θ) and the results are shown in Figures 4.7, 4.8, 4.9 and 4.10. All figures show the effect of varying one parameter only, the constant values of the rest of the parameters are: $\lambda = 700nm$, $r_{eff} = 1\mu m$, $v_{eff} = 0.1$, nr=1.42 (and nri=1e-7) and are based on [Stam et al., 2004].

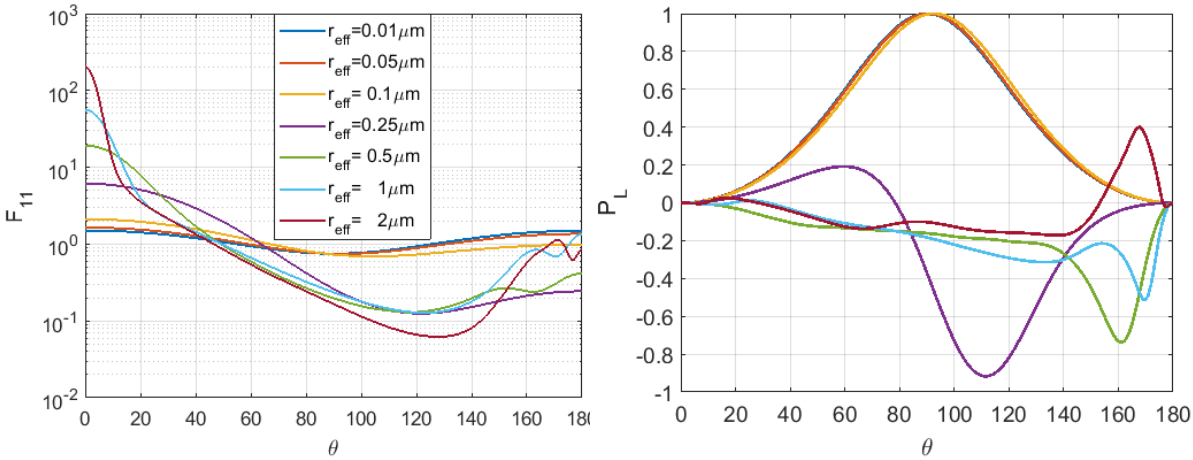

(a) Total flux for various r_{eff}

(b) P_L for various r_{eff}

Figure 4.7: F_{ss} and $P_{L,ss}$ for various r_{eff}

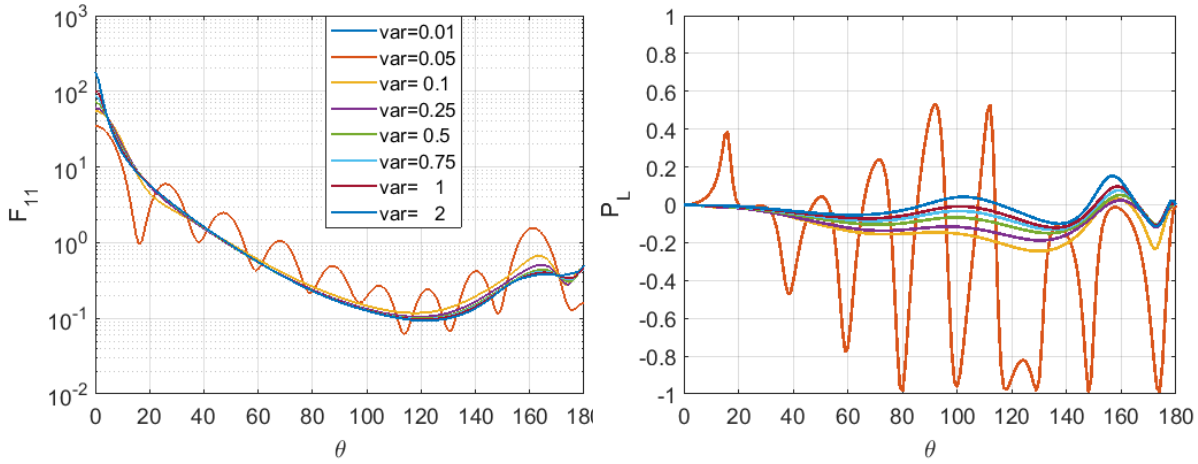

(a) Total flux for various v_{eff}(=var) (b) P_L for various v_{eff}

Figure 4.8: F_{ss} and $P_{L,ss}$ for various v_{eff} (denoted as var)

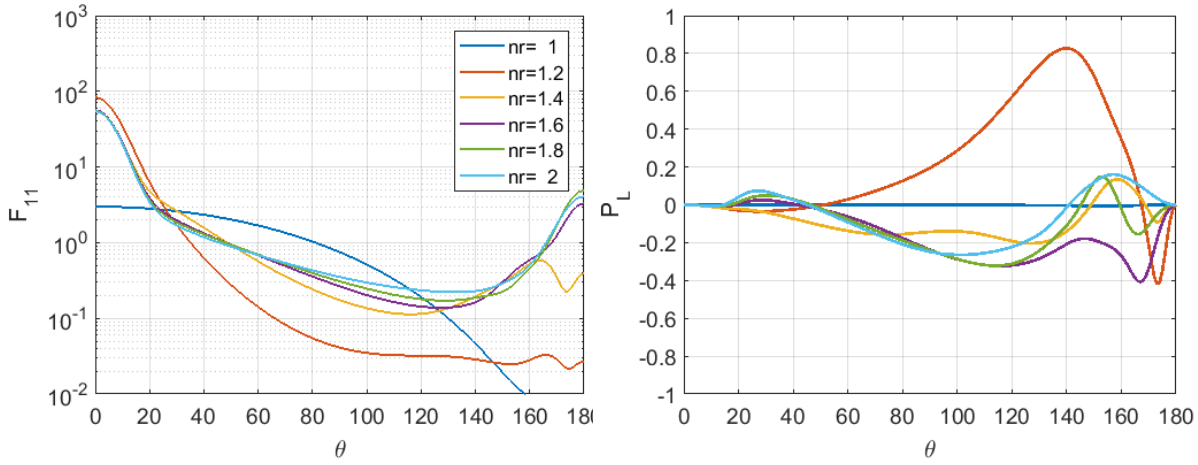

(a) Total flux for various nr (b) P_L for various nr

Figure 4.9: F_{ss} and $P_{L,ss}$ for various nr

From figure 4.7 it can be seen that for small particles the typical bell-shaped P_L-curve of Rayleigh scattering is present. The effective variance curves of figure 4.8 show that for small values oscillations are present and the curves for v_{eff}=var=0.01 and 0.05 are such close that the latter lies on top of the former. Also, note from figure 4.9 that a refractive index of 1 in fact means that the same medium is regarded such that no scattering occurs. Several aspects can be observed from the figures. An important base relating to these observations is the type of single scattering that occurs. Recall that the distinction between the single scattering types is usually based on a relation of the particle radius (r) to the wavelength (λ) of the light passing through the particle, given in equation 4.23. Where $x << 1$ corresponds to Rayleigh scattering, $x \approx 1$ to Mie scattering and for $x >> 1$ (much larger e.g. $x > 1000$ for example) scattering in the geometrical optics regime occurs. In this analysis r will not be multiple orders of magnitude higher than λ such that the latter will not occur.

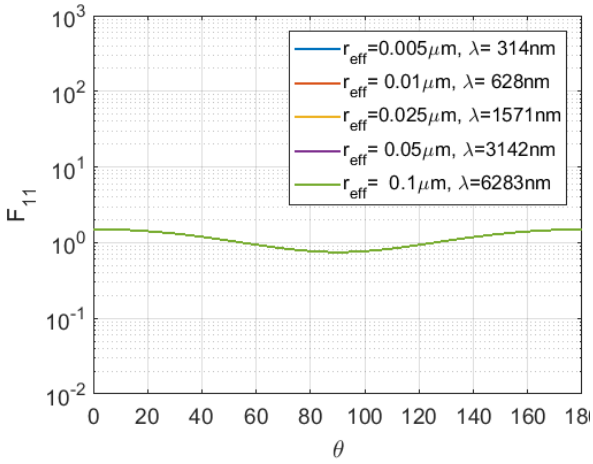

(a) Total flux for x=0.1 combinations

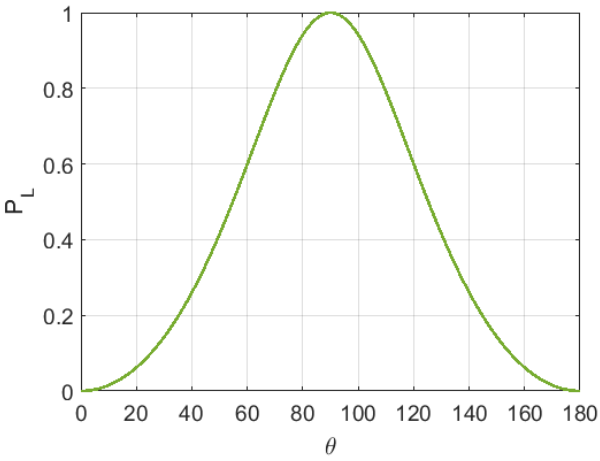

(b) P_L for x=0.1 combinations

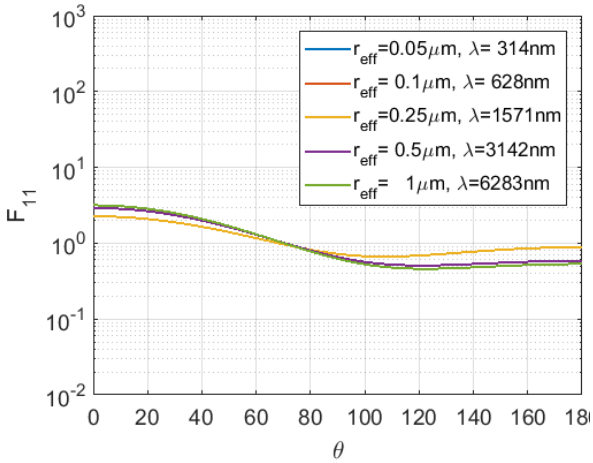

(c) Total flux for x=1 combinations

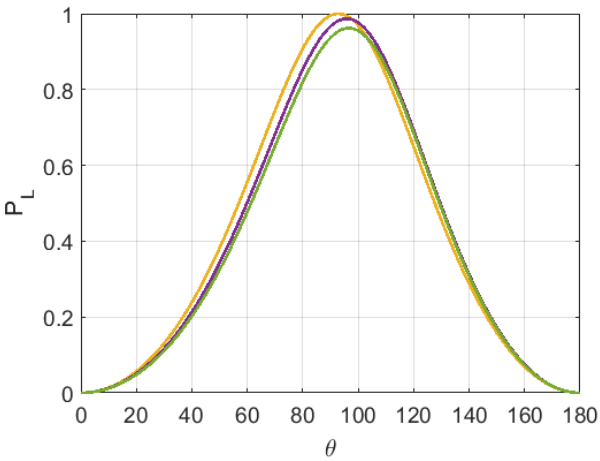

(d) P_L for x=1 combinations

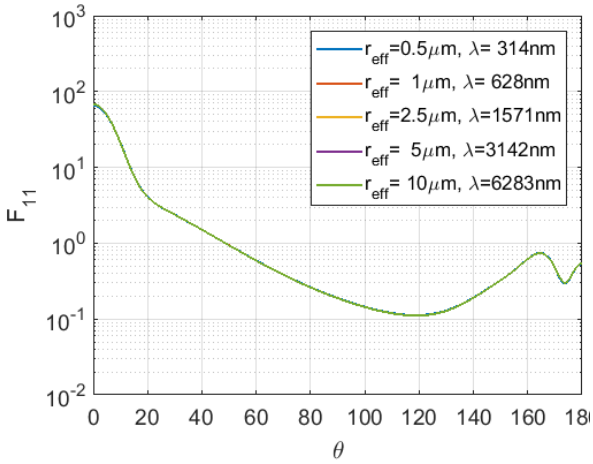

(e) Total flux for x=10 combinations

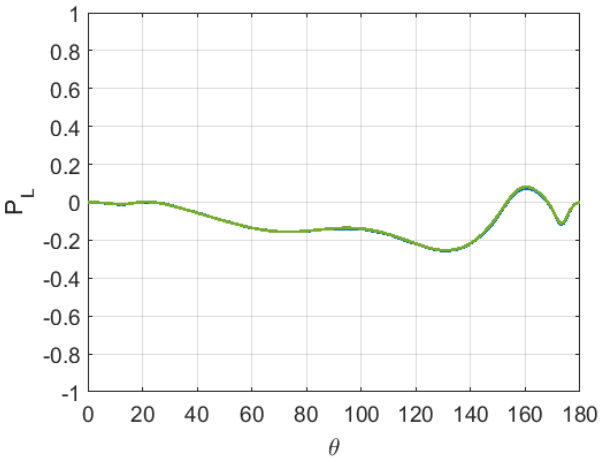

(f) P_L for x=10 combinations

Figure 4.10: F_{ss} and $P_{L,ss}$ for various x

$$x = \frac{2\pi r}{\lambda} \tag{4.23}$$

The different single scattering types can clearly be seen from the results of Figure 4.10. Firstly, from Figure 4.10 the general F_{ss} and $P_{L,ss}$ shapes can be seen (note that the green line indicates that all lines lie on top of each other). A bell-shaped $P_{L,ss}$ and F_{ss} curve is present for Rayleigh scattering. For the Mie scattering case the same shapes arise, although for higher r_{eff} and wavelength the curves start to shift a bit. For $x = 10$ the curve has an entirely different shape. This information is important as different wavelength filters are used in the analysis, such that for a particular particle (with constant r_{eff}) the type of scattering can change with wavelength.

Additionally, a more detailed investigation of $P_{L,ss}$ for r_{eff} and nr is made in Figure 4.11. The figure spans a range from r_{eff} = 0.1-5μm and nr from 1.1-1.9 and the x-parameter values are indicated on the right vertical axes. From the figure it can be observed that for relative larger r_{eff} (1-5μm) the refractive index becomes less sensitive to this r_{eff} as the contour lines of the two bottom plots are oriented mainly vertically. It can be seen that a high $P_{L,ss}$ only occurs for specific combinations of r_{eff} and nr. This combination changes with wavelength and for the higher wavelengths the maximum shifts to higher r_{eff} and nr values. When a specific composition of the cloud and haze is chosen later on, the specific refractive index can be used to look up what particle size results in the approximately preferred single scattering P_L-value. It has to be taken into account that in the analysis four different wavelength filters are used which makes it difficult to relate $P_{L,ss}$ to r_{eff} and nr directly. The $P_{L,ss}$ value can be used to check if a certain degree of linear polarisation can be achieved at the phase angle (10.73°, thus at $\theta = 169.27°$) at which the observations are taken.

Note that this analysis is already carried out before the observations were provided such that a slightly different phase angle was used. A value of 10.46° is used in this single scattering analysis as it is the highest phase angle of the data presented in [McLean et al., 2017] instead of the phase angle of the observations of this analysis of 10.73° as this latter value was not known at that point.

It is difficult to already identify what specific parameter values for r_{eff}, v_{eff}, and nr will match the observations well based on the single scattering properties only. Therefore, this single scattering analysis serves to identify the influence of these parameters on the single scattering Flux and degree of polarisation. In this way, knowledge is gained about the sensitivity of the different input parameters, which might be used in the fitting procedure later on. For example, when a particle is not able to capture the P_L-variation of the observations, it can be seen what particle properties show a larger single scattering P_L value and might therefore be able to capture this P_L-variation.

Despite that the single scattering properties are not used to determine the starting values for the particle properties, this single scattering analysis still shows some interesting aspects. These aspects are useful in the understanding of this subject. For example, the parameter x (see equation 4.23) influences the type of single scattering as is shown in figure 4.10. Note that Rayleigh scattering occurs (see the curve shapes) for the small particles in Figure 4.7 as well, as x(r) is small. For a certain parameter size (r_{eff}) a minimum effective variance (v_{eff}) is required to prevent strong oscillatory behaviour w.r.t. the scattering angle (θ), which is the case in Figure 4.8 for $r_{eff} = 1\mu m$ and an effective variance of $v_{eff} \leq 0.05$. Finally, both F_{ss} and $P_{L,ss}$ are strongly dependent on the particle properties as a little change in one parameter can induce a significant difference (see figures 4.7 to 4.9).

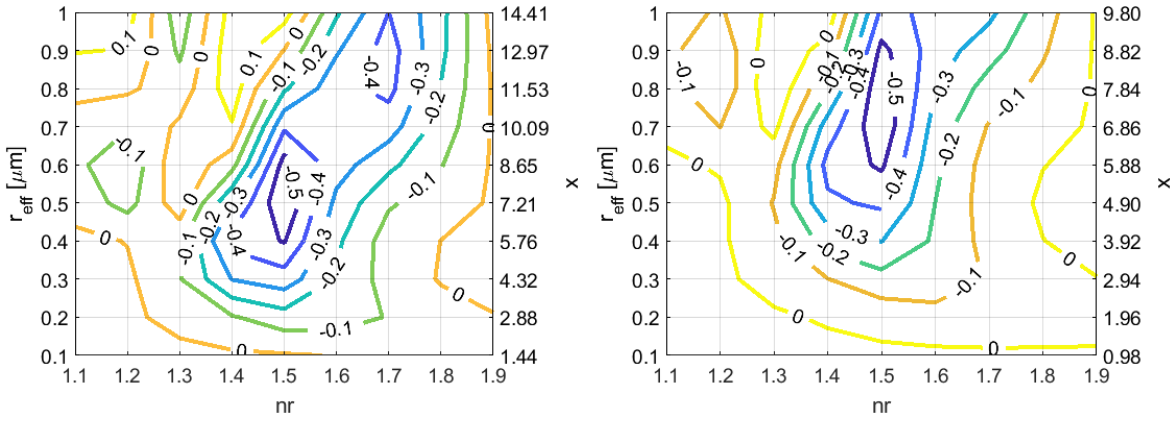

(a) $P_{L,ss}$ for mid-λ B-filter (436nm) and $\alpha = 10.46°$

(b) $P_{L,ss}$ for mid-λ R-filter (641nm) and $\alpha = 10.46°$

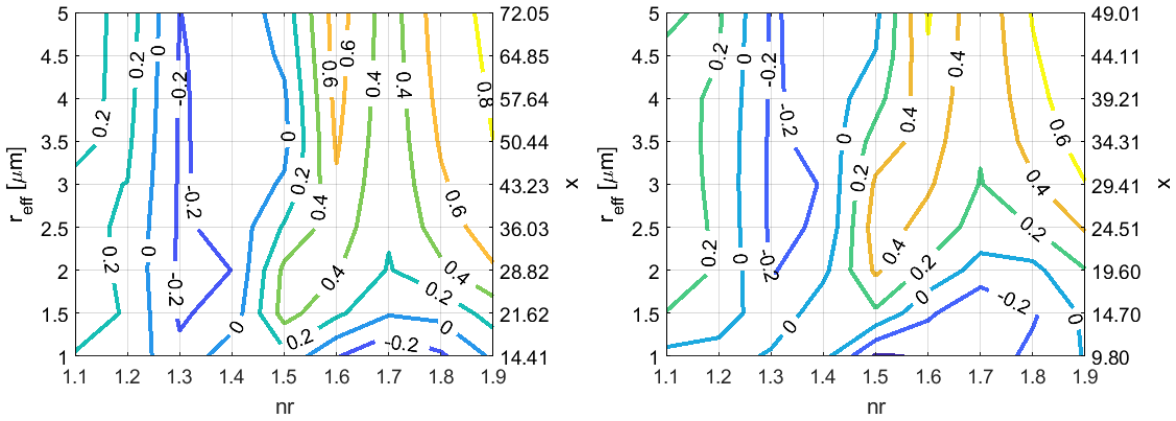

(c) $P_{L,ss}$ for mid-λ B-filter (436nm) and $\alpha = 10.46°$

(d) $P_{L,ss}$ for mid-λ R-filter (641nm) and $\alpha = 10.46°$

Figure 4.11: $P_{L,ss}$ for various r_{eff}-nr combinations in the B and R-filter

5

Fitting Procedure

This chapter elaborates on the fitting procedure written in Matlab. The aim is to find an as good as possible match of the observations with data generated using the numerical model (see chapter 4). Therefore, in this chapter the Matlab code and its link to the Fortran code are elaborated upon in section 5.1. The data processing of the output data of the Fortran code which serves as input for the Matlab code is addressed and verified in section 5.2. Some main considerations before initiating the fitting procedure are discussed in section 5.3. Afterwards, the optimisation parameters used in the fitting procedure are dealt with in section 5.4. The method is elaborated upon in section 5.5 and the different regarded situations to make a comparison between different particles and implementations is touched upon in section 5.6.

It has to be taken into account that the ground-based observations allowed for a limited phase angle of 10.73° and that only spherical particles have been regarded in this analysis. As more limitations hinder a high accuracy comparison between the observations and model, the outcome will give an indication of the atmospheric structure of Jupiter's upper atmospheric layers instead of a conclusive result.

5.1. The Matlab code

The Matlab code processes the data generated using the numerical atmospheric model written in Fortran (chapter 4) as is visualised in the code flow diagram of figure 5.1 to be able to compare the observations to the numerical model data.

First, a short recap of the numerical atmospheric model related to figure 5.1 is given. The Fortran code is regularly referred to as the numerical atmospheric model and consists of three main parts; the MIE, DAP and GEOS code parts. All three parts have particular input parameters which are used in the procedure to come up with output parameters. The MIE code relates to the particle properties, the DAP code to the atmospheric build up and the GEOS code finally translates this information to the Stokes parameters F, Q and U per wavelength per pixel along Jupiter's visible disk.

The Matlab code is subdivided in three main parts as well. First, the output of the numerical atmospheric model has to be processed. The Stokes parameters F, Q and U are provided per wavelength and for all pixels along Jupiter's disk in matrix format. The wavelengths of the different wavelength filters are linked to the output files of the Fortran code to be able to integrate F, Q and U along the wavelength filters using numerical integration. With these integrated F, Q and U the degree of linear polarisation (P_L) per wavelength filter per pixel can

be computed using equation 2.5. This P_L per wavelength filter can consequently be compared to the observed P_L corresponding to the same wavelength filter for the entire disk. The P_L-difference that arises between the observations and the numerical model data is referred to as ΔP_L and is used to evaluate the atmospheric properties of Jupiter's upper atmosphere. Several possible ways to minimise ΔP_L exist and the one used in this research is elaborated upon in section 5.5. The atmospheric properties corresponding to this minimum ΔP_L can be identified. Based on the found ΔP_L along Jupiter's disk, different particle properties and a different atmospheric build up can be proposed in order to come up with a lower ΔP_L. This part is shown by the feedback-loop in the figure.

It is important to note that the verification of the Fortran code is already addressed in section 4.3 and that the verification of the Matlab code is present in section 5.2.

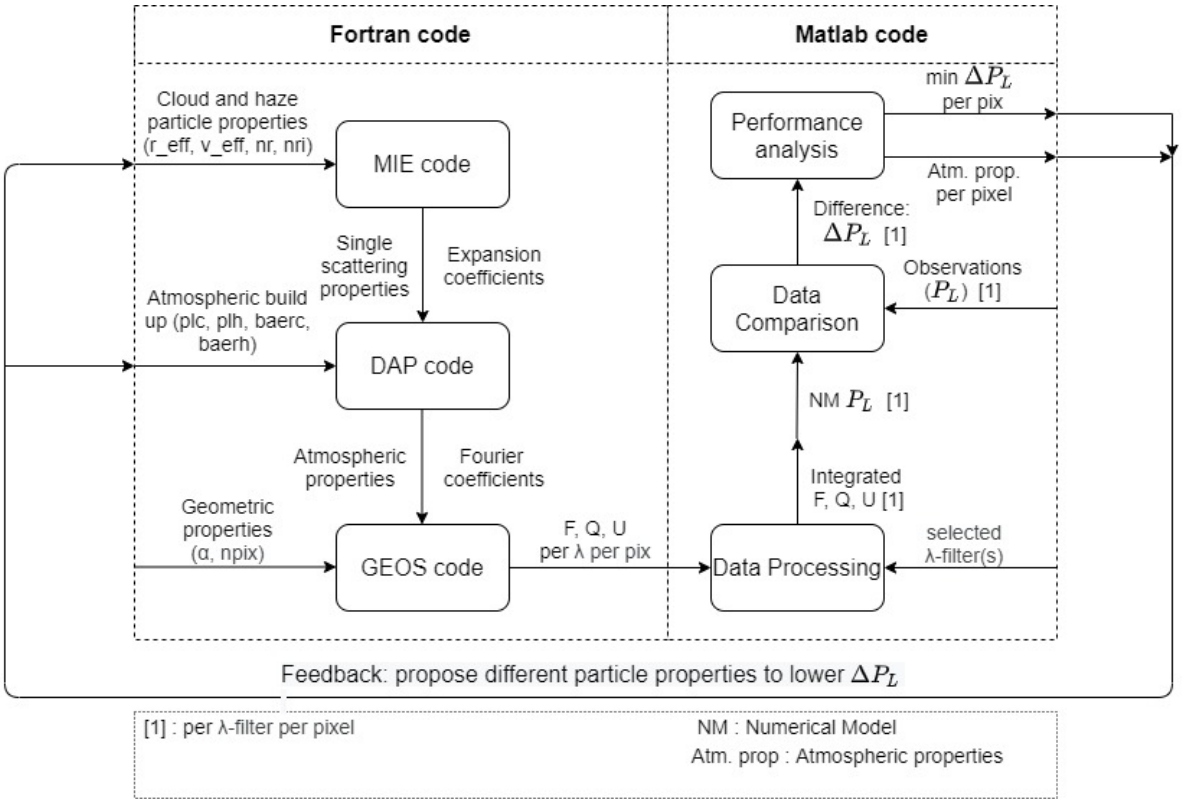

Figure 5.1: Code Flow Diagram

5.2. Data Processing and Verification

This section discusses the data processing part of the Matlab code (see figure 5.1) in more detail and additionally verifies that this part of the code works as expected.

The output of the numerical atmospheric model, the Stokes vector parameters (F, Q and U) per wavelength and per pixel location along Jupiter's visible disk, have to be processed before a comparison with the observations can be made. As every output file regards one wavelength, the wavelengths of the chosen wavelength filter (see section 3.3) have to be linked to the data files.

The next step is to integrate F, Q and U over the wavelength filter, which is done using the trapezoidal rule. The result is the integrated F, Q and U over the wavelength filter.

Afterwards, the degree of linear polarisation (P_L) can be determined from the integrated F, Q and U using equation 2.5.

The ToPol instrument observes a number of photon counts on the detector and from the different signals the Stokes vector parameters can be deduced per wavelength filter. The degree of linear polarisation is therefore determined from the integrated Stokes vector parameters for the observations, which is done for the numerical model as well.

The next step comprises the matching of the data to the correct pixel locations on Jupiter's visible disk. The Fortran code outputs the data in a matrix where the data is loaded in from the left, such that all zeros appear on the right (see subfigure 5.2a). The relative pixel locations are used for this matching. This procedure can be seen in figure 5.2 from subfigure 5.2a to 5.2b.

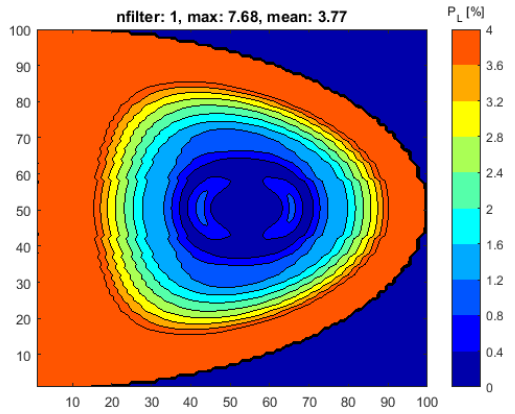

(a) P_L for λ_{eff}=366nm (U-filter) from input data

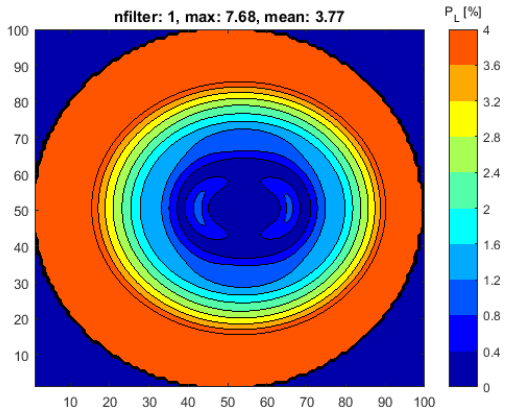

(b) P_L for λ_{eff}=366nm (U-filter) on visible disk

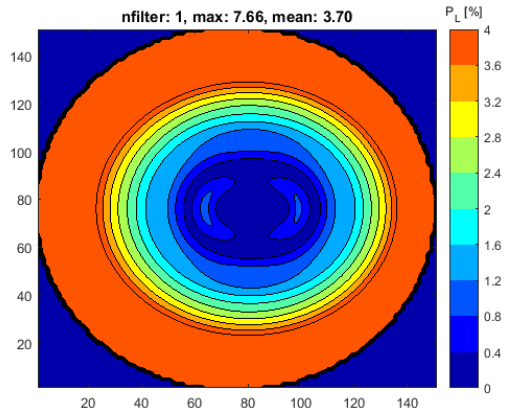

(c) P_L for λ_{eff} =366nm (U-filter) interpolated

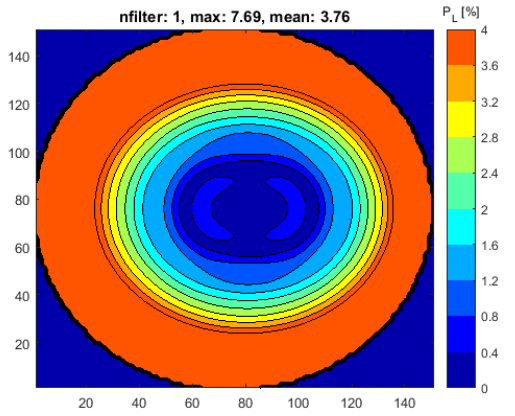

(d) P_L integrated over the U-filter and interpolated

Figure 5.2: Verification of the data processing for the U-filter

Finally, the degree of linear polarisation per wavelength filter has to be interpolated to the size of the observations (151x151 pixels) to make it possible to compare every pixel location directly. Consequently, a small interpolation error is induced by using the Matlab interpolation function which uses linear interpolation. This step is shown from subfigure 5.2b to 5.2c.

The data processing is verified by visual inspection using figure 5.2. Polarisation data in the U-filter is used as in this filter no methane absorption is present and as the effective wavelength represents the wavelength filter best for this filter.

From sub-figure 5.2a and 5.2b it can be seen that the correct pixel locations are matched well using the relative pixel locations and indeed Jupiter's visible disk is created. It can be seen that the results with and without interpolation (sub-figures 5.2b and 5.2c) only slightly differ which confirms the correct interpolation implementation, while the number of pixels increases to the observational data size (151x151 pixels). Also, the result when integrating the Stokes vector parameters F, Q and U before constructing P_L for the U-filter (sub-figure 5.2d) is very close to the result at the effective wavelength (sub-figure 5.2c) which confirms that the numerical integration is implemented correctly.

5.3. Pre-fitting Considerations

Before comparing the observations and the numerical model, some considerations have to be regarded, which are dealt with in this section.

5.3.1. Exclusion of the Polar Regions

In the fitting procedure it is decided to exclude the polar regions. The numerical atmospheric model (Fortran code) considers spherical particles that scatter light according to the Mie theory. It is expected that the polar haze contains aggregates of particles, which can be added to the code as is done by [Karalidi et al., 2013] and [McLean et al., 2017]. However, in this analysis this addition has not been made due to time constraints and thus only single spherical particles are regarded which cannot fit the polar regions well. Consequently, the polar regions are disregarded in this analysis.

When the optical thickness of the haze is small, the influence of this choice is marginal. However, in the polar regions a higher optical thickness of the haze is expected such that the effect is larger. Indeed, it turns out that the high polarisation values at Jupiter's polar regions cannot be matched well by the numerical model used in this analysis.

Due to the afore-mentioned reasons, it is decided to exclude the polar regions. It is decided to define the poles as the region in the B-filter where P_L exceeds 4%. In this way, both the polar region latitudes are in conformance with the general polar latitudes of Jupiter (for example in [Lissauer and de Pater, 2013]) and the highest polarisation regions (which are difficult to match) are disregarded.

5.3.2. Not Applying Data Smoothing

The observations of the Torino Polarimeter are already processed such that the provided data of this analysis consists of total flux (F) and degree of linear polarisation (P_L) values along Jupiter's entire visible disk. As a consequence, no additional data processing of the observations is required. Additionally, the effect of the distortion and corresponding alignment error (due to the internal telescope's path) is not exactly known, making it difficult and not recommended to compensate for.

It is also possible to apply data smoothing on the results of the numerical model. For the numerical model aspects as the seeing limitation and the distortion and alignment error are in fact not present, as no observations with a telescope through Earth's atmosphere are regarded. It is possible to simulate the observations by taking into account these effects. However, the exact effect of the seeing limitation and distortion and alignment error is unknown. Moreover, the results from the numerical model are already much more smooth than the observations (see for example the P_L figures in appendix A). Averaging can be used to compensate the

observations for the distortion-alignment error and the seeing limitation as is done in [McLean et al., 2017]. To better mimic these observations averaging can be applied on the numerical model as well. However, the data processing part is already carried out previous to this research and the F and P_L result of the observations are directly provided. Therefore, no averaging has to be applied at this stage as the processed data is already available.

All in all, it has been decided not to apply data smoothing on both the observations and numerical model result.

5.3.3. Variation in Disk Shape of the Observations and the Numerical Model

To be able to compare the observations and the numerical model pixels one to one, the shape of their non-zero valued data has to be exactly the same. The observations have a size of 151x151 pixels such that the data of the numerical model is interpolated to this same size (using the linear interpolation function in Matlab). However, due to the phase angle (α) and the numerical model which only regards direct sun-light, the outer right edge is missing for the numerical model as no direct sun-light is received here. The observations do have the right outer edge visible as in reality a twilight-zone exists such that still light can be received from this part of the atmosphere that entered at another location. To compensate for this effect only the non-zero valued pixels of the observations that have a non-zero valued pixel for the numerical model are considered. The consequence is that the right edge of the visible disk is not as smooth as the left edge, which can be seen in the figures of chapter 6. Note that the numerical model has to be rotated by the north pole angle of 24.9331° (for the observation date) as the observations are rotated by this same angle. Otherwise, the right edge of the numerical model does not match the right edge of the observations.

5.4. Optimisation Procedure

The objective of this analysis is to find an as good as possible fit of the degree of linear polarisation observations (chapter 3) with the numerical model. For this purpose different numerical model parameter values are evaluated to minimise the P_L-difference between the numerical model and the observations. This P_L-difference is minimised per wavelength filter and per pixel location on Jupiter's disk. A similar optimisation procedure is already used in previous research, such as in [Fernández Jiménez, 2018] where the region of Jupiter's great red spot is analysed.

The cloud's pressure layer (plc) and the haze optical thickness (baerh) are regarded as variables to capture the ΔP_L variation along the disk (see section 5.5). The difference in P_L-sensitivity related to the position on Jupiter's disk is mitigated by performing the optimisation per pixel location.

The main parameter that has to be minimised is the P_L-difference between the observations and the numerical model, which is stated in equation 5.1.

$$\Delta P_L = |P_{L,obs} - P_{L,nm}| \tag{5.1}$$

$P_{L,obs}$ and $P_{L,nm}$ denote the degree of linear polarisation of the observations and the numerical model respectively. This parameter is minimised per wavelength filter and pixel location for a particular set of particle properties, as is explained in the upcoming sections and chapter.

5.5. Method

The atmospheric parameter values best representing the observations using the minimum P_L-difference of section 5.4 are searched for. The atmospheric parameters consist of the following for both the cloud and the haze; the refractive index and its imaginary part (nr and nri), the effective radius of the spherical particles used (r_{eff}), the effective variance on the effective radius (v_{eff}), the pressure layer defining the pressure boundaries at which the aerosols are present (pl) and the optical thickness (baer). The distinction between the cloud and haze is in this analysis made by the addition of c or h to the subscript of the parameter name respectively.

In this analysis only one cloud layer is considered besides an overlying haze layer. It is possible and it would better resemble Jupiter's atmospheric structure to take into account more cloud layers as different composed clouds are expected in Jupiter's atmosphere. However, it complicates the fitting procedure by introducing more parameters (6 per added cloud on top of the 12 parameters for the haze and first cloud). Moreover, polarimetry is sensitive to the upper atmosphere and its properties only, limiting the added value of more cloud layers. Clouds have a relative high optical thickness, such that the sensitivity decreases rapidly for every lower cloud added. Considering the aforementioned arguments, one optically thick cloud is chosen to partially make up the effect of the different clouds.

The next step is to limit the number of possible values for the 12 optimisation parameters as the P_L-sensitivity of the parameters is different. As a consequence, the less P_L-sensitive parameters can be set to a realistic value, which will be based on previous research, while the P_L-sensitive parameters are kept variable to capture the variation in P_L with wavelength and position along Jupiter's disk. The less P_L-sensitive parameters are identified in appendix B as the haze pressure layer and the optical thickness of the cloud layer while the cloud pressure layer and the haze optical thickness are P_L-sensitive. Additionally, appendix C shows the test cases used as stepping stone to build the results of chapter 6 on. The pressure layer at which the haze is present is set to layer 14, which ranges from 0.1334-0.1000bar. This value is in conformance with results from (among others) [Sromovsky and Fry, 2002] and [McLean et al., 2017]. When an optically thick cloud is considered, the exact aerosol optical thickness (when large enough) has only a marginal influence on P_L. Therefore, an optical thickness of the cloud layer (baerc) of 25 is regarded in combination with a cloud extending over two pressure layers (pressure layers as defined in Table 4.1). A cloud extending over two pressure layers is considered as it better resembles the different clouds and is in conformance with [McLean et al., 2017] and [Fernández Jiménez, 2018] as well as the optical thickness value itself.

As initial starting point, the cloud and haze particles of [McLean et al., 2017], and [Stam et al., 2004] (the latter are also used in [Fernández Jiménez, 2018]) are regarded. The refractive index (nr+nri) is taken in accordance with these particles and is regarded a constant in this analysis to limit the number of optimisation parameters. From previous research an upper cloud of ammonia-ice is expected, which has an obtained refractive index of 1.42 [Martonchik et al., 1984] which is thus used in the analysis. The exact composition of the overlaying haze is yet unknown. Hence, a refractive index of 1.50 is used for the smaller particles based on [Stoll, 1980] who modelled Jupiter's polarisation using Pioneer observations. This refractive index of the haze is used by [Karalidi et al., 2013] and [McLean et al., 2017] as well. For the larger haze particles a refractive index of 1.66 is used based on [Sromovsky and Fry, 2002] which is in conformance with [Stam et al., 2004] and [Fernández Jiménez, 2018]. The imaginary part of the refractive index (nri) is chosen in conformance with the cloud and haze particles

of [McLean et al., 2017] and [Stam et al., 2004] as well. For the smaller particles ([McLean et al., 2017]) a value of 0.015 for the cloud and 0.001 for the haze is used and for the larger particles ([Stam et al., 2004]) a value for both the cloud and haze of 1e-7 is used as a value of zero does not work in the Fortran code. In case of the approximation of UV-absorption by the aerosols (which is done for situation 3 as described in section 5.6) nri is estimated using geometric albedo data of [Karkoschka, 1998] (as is explained in section 4.4). In the wavelength range from 300 to 520nm, nri is varied to match the geometric albedo and is linearly increased from 2e-4 (at 520nm) to 5e-3 (at 300nm) for the cloud and from 2e-4 to 0.1 for the haze.

This would leave the particle's effective radius and effective variance (r_{eff}, v_{eff}) for both the cloud and haze as well as the cloud's pressure layer (plc) and haze optical thickness (baerh) to be determined. The parameters r_{eff} and v_{eff} are analysed using grid search for various plc and baerh values and the found values are equal or close to the original values of [McLean et al., 2017] and [Stam et al., 2004], as is discussed in section 6.1.

For the other two parameters it is expected that significant variations along Jupiter's visible disk occur. In the first place, previous research showed that in Jupiter's belts and zones the clouds exist at different pressure levels. Secondly, the optical thickness is expected to become higher towards the poles (among others in [West et al., 2004] and [McLean et al., 2017]) and differences between the belts and zones are expected as well. The pressure layer at which the cloud is present and the haze optical thickness are therefore taken as variables in the analysis such that they can have a different value per pixel location and per wavelength filter.

The optimisation procedure of identifying the minimum ΔP_L per wavelength filter per pixel along Jupiter's disk is visualised in figure 5.3. For each individual pixel along the disk (excluding the poles), ΔP_L is determined for all combinations of cloud pressure (plc) and haze optical thickness (baerh) as visualised in the top right sub-figure. The minimum ΔP_L value for each pixel is identified as well as the corresponding best performing plc and baerh values. In this way, the ΔP_L, baerh and plc values along Jupiter's disk can be determined and visualised. An example of the latter is shown in the plots of figure 5.3. This procedure is repeated for all four wavelength filters.

This ΔP_L optimisation per wavelength filter per pixel is performed regarding the particle properties (table 6.2 and 6.3), the cloud optical thickness of 25, the haze pressure range from 0.1334-0.1000bar and the combination of variable cloud pressure layer and haze optical thickness. The parameter values chosen for the cloud pressure and haze optical thickness span the expected parameter value range and are indicated in the colour bar of the two bottom sub-figures of figure 5.3. In subsection 6.5.3 the cloud pressure and haze optical thickness are compared to previous research.

In this optimisation procedure first the most P_L-sensitive atmospheric parameters have been identified in order to simplify the parameter search. The most P_L-sensitive parameters are identified as the cloud pressure (plc) and the haze optical thickness (baerh). To analyse the particle properties in more detail three different particle property situations are regarded as will be explained in section 5.6. It has to be noted that adding more variable parameters will result in a limited improvement of the ΔP_L performance as the current parameters capture the P_L variations with wavelength and position well. Simultaneously it would increase the optimisation complexity, the data generation time and the clarity of the variable parameter results. The latter is true as it becomes more difficult to distinguish patterns in the plc and baerh plots when more variable parameters are introduced.

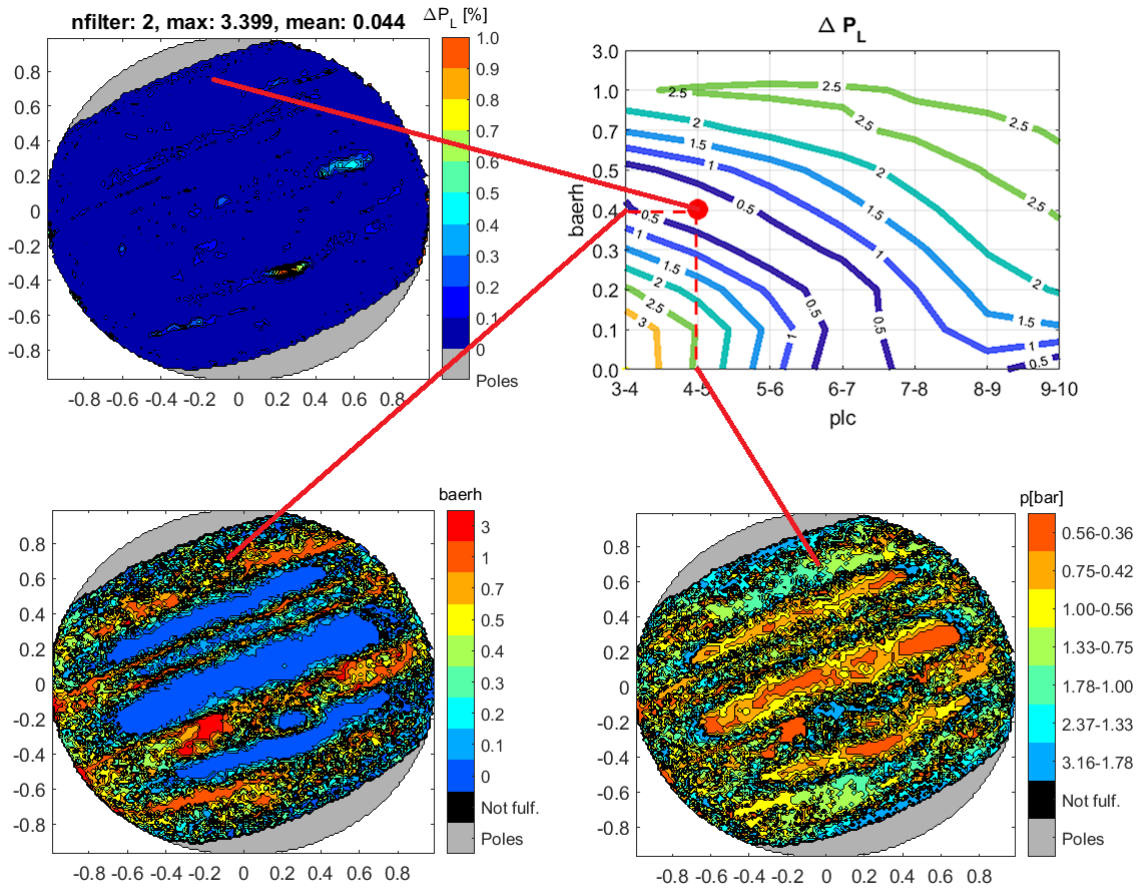

Figure 5.3: Optimisation procedure per pixel per wavelength filter

5.6. Different Situations

The results elaborated upon in the next chapter are divided in three different situations.

First, the larger cloud and haze particles with the atmospheric properties as mentioned in table 6.2 are regarded and no UV-absorption is taken into account.

The second case regards the smaller cloud and haze particles with the atmospheric properties as stated in table 6.3. In this situation, no UV-absorption is considered as well.

The last option again regards the smaller cloud and haze particles with the atmospheric properties as stated in table 6.3. Additionally, it takes into account the absorption at lower wavelength using the imaginary part of the refractive index (nri) that matches the geometric albedo of Jupiter (as explained in section 4.4). A drawback of the UV-absorption approximation is that the estimated imaginary part of the refractive index has to be linked to a certain particle composition, which is unknown for the estimated values. Also, using the geometric albedo the exact amount of UV-absorption cannot be determined as the exact composition of Jupiter's atmosphere is unknown. Therefore, it is a first order approximation of UV-absorption. On the other hand, an approximation of the UV-absorption of Jupiter's atmosphere is a better representation of reality than when not taking into account this effect.

6

Results

This chapter presents the parameter values used in the numerical model that best match the observed degree of linear polarisation (P_L). The corresponding P_L-difference is evaluated for three different situations. Also, the results of the degree of linear polarisation (P_L) and the non-calibrated total flux (F) obtained using the procedure described in section 5.5 are discussed. The best cloud pressure and haze optical thickness values per pixel location minimising ΔP_L are presented as well.

6.1. Determination of the Particle Properties

The P_L-difference between the observations and the numerical model (ΔP_L) per wavelength filter per pixel is evaluated as is explained in section 5.4 and 5.5. The values of r_{eff} and v_{eff} are varied linearly, using grid search, around the initial values as stated in table 6.1. These starting values are taken from previous research where polarimetric data of Jupiter's atmosphere or Jupiter-like exo-planets is presented. The rest of the parameter space is fixed, with the particle properties as stated in table 6.1, a value for the cloud optical thickness of 25 and the haze pressure ranging from 0.1334 to 0.1000bar and finally a variable cloud pressure and haze optical thickness of which the values are shown in the colour-bar of figure 6.13.

Various parameter values have been evaluated in combination with a variable cloud pressure and haze optical thickness and it turned out that both the smaller particles ($r_{eff,c} = 0.5\mu m$ and $r_{eff,h} = 0.2\mu m$) suggested by [McLean et al., 2017] and the larger particles ($r_{eff,c} = 1.00\mu m$ and $r_{eff,h} = 0.50\mu m$) suggested by [Stam et al., 2004] (and used as well in [Fernández Jiménez, 2018]) match the observations well for a variable cloud pressure and haze optical thickness. Therefore, different situations are regarded as explained in section 5.6 to be able to make a comparison between different particle properties. For the defined refractive index, the values of r_{eff} and v_{eff} for both the cloud and haze are analysed.

Some examples of different $r_{c,eff}$ and $r_{h,eff}$ for fixed v_{eff} and their ΔP_L result are shown in appendix E. It can be seen that it is difficult to quantify what particle properties are performing best in terms of minimising ΔP_L as variations along the disk and along the wavelength filters occur. These variations in turn relate to the sensitivity to P_L of the different wavelength filters and disk positions. Furthermore, particle properties deviating from the initial particle properties do not show (significant) better ΔP_L performance. Therefore, it is decided at an early stage of this analysis to use the particle properties close or equal to the initial particle properties

of table 6.1. These particle properties for the different situations are indicated in table 6.2 and 6.3 respectively.

Latitudinal variations due to the belts and zones are expected to be mainly caused by variation in the cloud altitude. Variation in haze optical thickness is expected to be present as well with slight differences between the belts and zones and with a higher value towards the polar regions. These variations are addressed in sub-section 6.5.2. Previous research did not mention (large) variations in particle properties as the cloud composition is expected to be (approximately) constant over the entire disk. [McLean et al., 2017] and [Fernández Jiménez, 2018] did not use variable particle properties for different locations, however, they did not fit Jupiter's entire visible disk. Consequently, only one cloud and haze particle are considered in this analysis as well. More cloud and haze particles also complicate the analysis of the variable cloud pressure and haze optical thickness as it becomes more difficult to distinguish distinct patterns.

Table 6.1: The parameter values of the numerical model used to represent Jupiter's atmosphere

Parameter	$r_{eff,c}$	$v_{eff,c}$	nr_c	$r_{eff,h}$	$v_{eff,h}$	nr_h
[Stam et al., 2004]	$1.0\mu m$	0.1	1.42	$0.5\mu m$	0.01	1.66
[Karalidi et al., 2013]	$0.5\mu m$	0.1	1.48+0.01i	aggregates	aggregates	1.50+0.001i
[McLean et al., 2017]	$0.5\mu m$	0.05	1.42+0.015i	$0.2\mu m$	0.01	1.50+0.001i
[Fernández Jiménez, 2018]	$1.0\mu m$	0.1	1.42	$0.5\mu m$	0.01	1.66

Note that [Karalidi et al., 2013] uses aggregates of haze particles for the polar regions such that no specific value for $r_{eff,h}$ and $v_{eff,h}$ is used

The P_L-difference of the observations and the numerical model (ΔP_L) is evaluated for the parameter values specified previously in section 5.5 and the best parameter value combinations are stated in Table 6.2 and 6.3 in combination with a variable optical thickness of the haze (baerh) and pressure layer at which the clouds occur (plc). Per pixel and wavelength filter, the combination of baerh and plc minimising ΔP_L is regarded. The results and the corresponding analysis are discussed in the upcoming sections. Note that for the third situation other values are found for the imaginary part of the refractive index (nri), which is indicated by (3) in table 6.3.

Table 6.2: The parameter values of the numerical model used to represent Jupiter's atmosphere for situation 1

Parameter	Cloud	Haze
r_{eff}	$1.00\mu m$	$0.50\mu m$
v_{eff}	0.10	0.01
nr	1.42	1.66
nri (2)	1e-7	1e-7
pl	variable	14 (0.1000-0.1334bar)
baer	25	variable

Table 6.3: The parameter values of the numerical model used to represent Jupiter's atmosphere for situation 2 and 3

Parameter	Cloud	Haze
r_{eff}	$0.52\mu m$	$0.22\mu m$
v_{eff}	0.05	0.01
nr	1.42	1.50
nri (2)	0.015	0.001
nri [520-900nm] (3)	2e-4	2e-4
nri_{max} (at 300nm) (3)	5e-3	0.1
pl	variable	14 (0.1000-0.1334bar)
baer	25	variable

6.2. Situation 1

For the first situation the larger cloud and haze particles with the atmospheric properties as mentioned in table 6.2 are regarded. No UV-absorption is taken into account in this case as it cannot be implemented accurately as much is unknown about it.

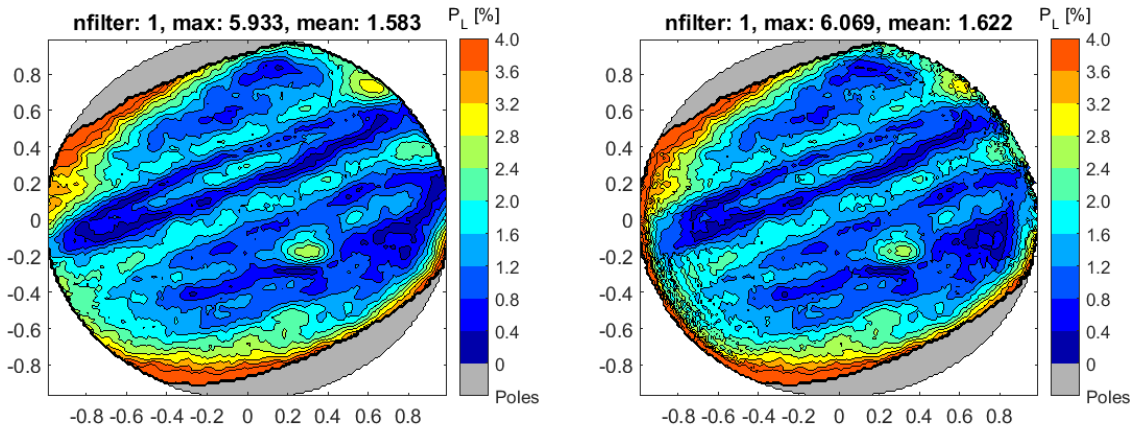

(a) Observed P_L in the U-filter

(b) Numerical model P_L in the U-filter

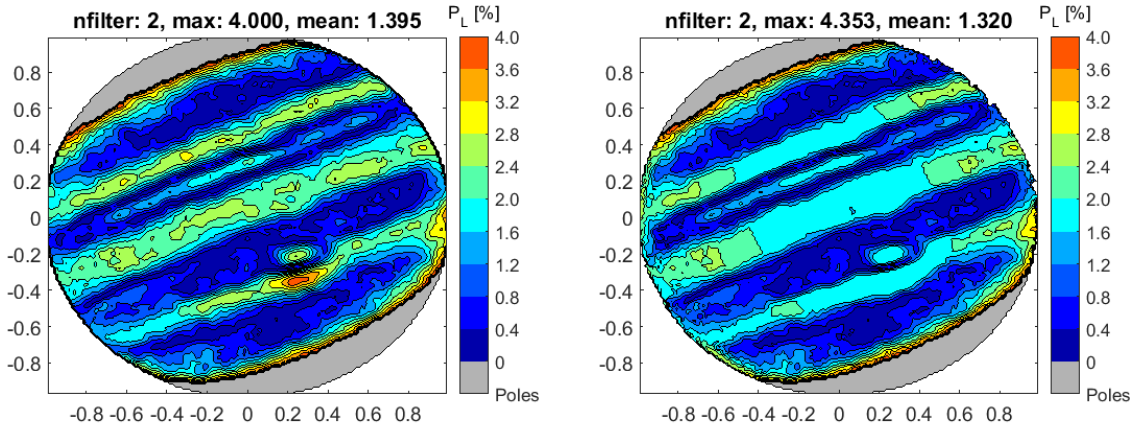

(c) Observed P_L in the B-filter

(d) Numerical model P_L in the B-filter

Figure 6.1: 1: Comparison of the observed and modelled P_L for the U and B-filter

6.2.1. The P_L Comparison

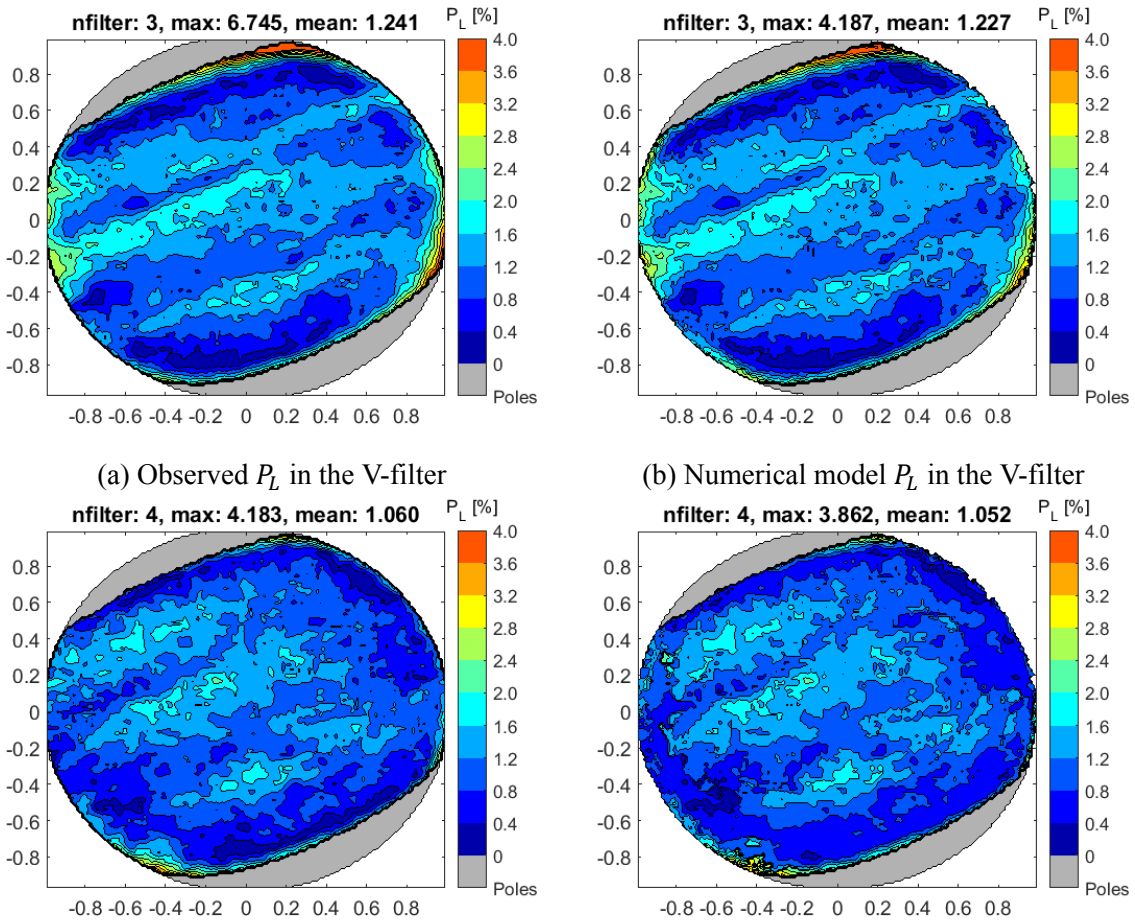

(a) Observed P_L in the V-filter

(b) Numerical model P_L in the V-filter

(c) Observed P_L in the R-filter

(d) Numerical model P_L in the R-filter

Figure 6.2: 1: Comparison of the observed and modelled P_L for the V and R-filter

The linear degree of polarisation (P_L) plots are shown in Figure 6.1 and 6.2 for all wavelength filters respectively. The observations are shown in the left sub-figures and the corresponding result of the numerical model can be seen on the right. The difference in P_L between the observations and the numerical model, which is denoted as ΔP_L, is visualised in Figure 6.3. These ΔP_L plots show in a clear way where the higher P_L-differences along Jupiter's disk occur.

The results of the U-filter (first sub-figures of Figure 6.1 and 6.3) show that the model fits the P_L observations well except from some small low P_L regions near the edges. The results of the B-filter show larger P_L-differences, mainly for the high P_L-regions for the mid-longitudes. In these high P_L-regions, the particle properties are not able to capture the high observed P_L. In the V-filter the fit of the observed P_L is well along the entire disk except for some marginal differences at the edges. The modelled P_L in the R-filter matches the observations well for most part, except for some relative high P_L-regions near the left edge.

The P_L-comparison for situation 1 shows that the particle properties are able to match the low P_L-regions of the observations well for all four wavelength filters. The higher observed P_L-regions, especially at the mid-longitudes in the B-filter cannot be captured by the model, such that a significant ΔP_L arises in these regions. Also, some low P_L regions of the observations

in the U-filter occurring at the edges cannot be matched by the model. In principle, the latter does not have to be a problem as the numerical model is less accurate near the edges .

More conclusions regarding the P_L-differences for the four wavelength filters for this situation and the corresponding variable atmospheric parameters plc and baerh are given in section 6.5.

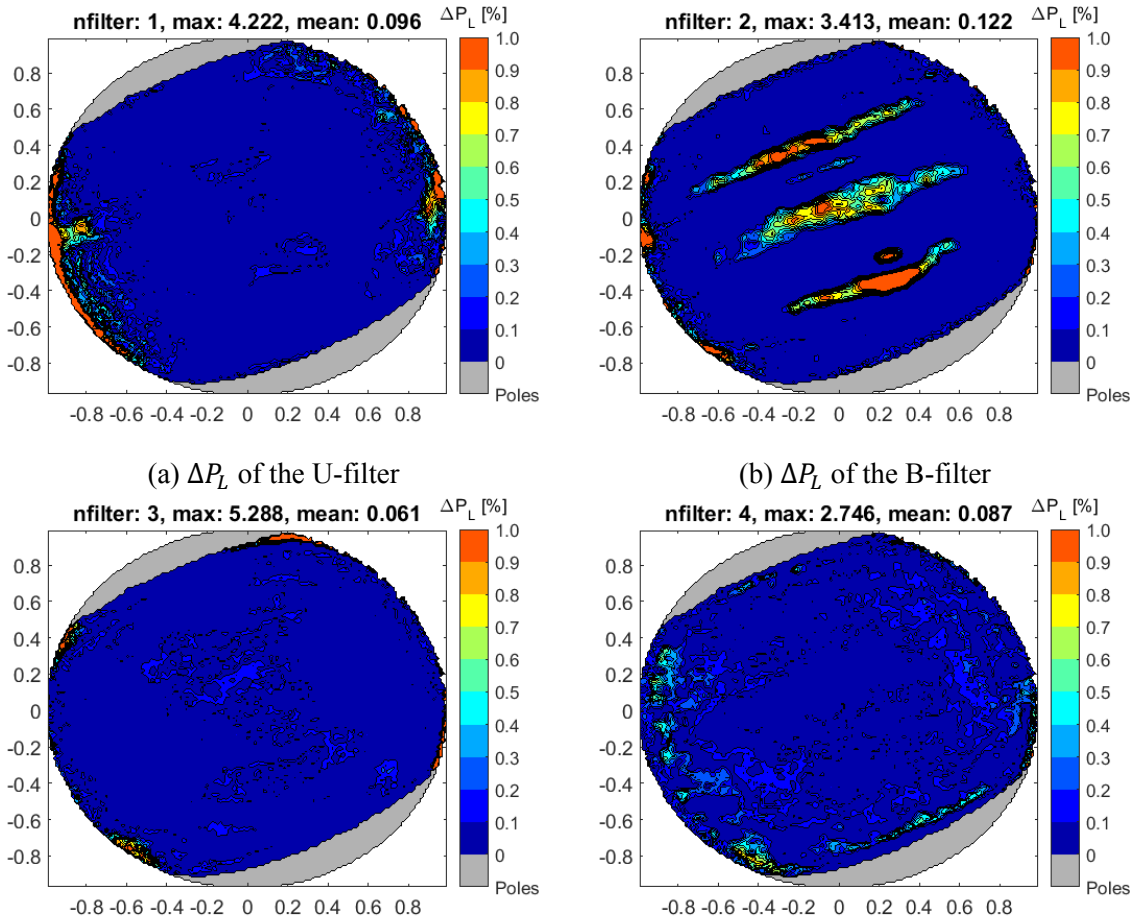

(a) ΔP_L of the U-filter

(b) ΔP_L of the B-filter

(c) ΔP_L of the V-filter

(d) ΔP_L of the R-filter

Figure 6.3: 1: P_L-difference between the observations and the numerical model

6.3. Situation 2

For this situation the smaller particles of table 6.3 are used and no UV-absorption is considered.

6.3.1. The P_L Comparison

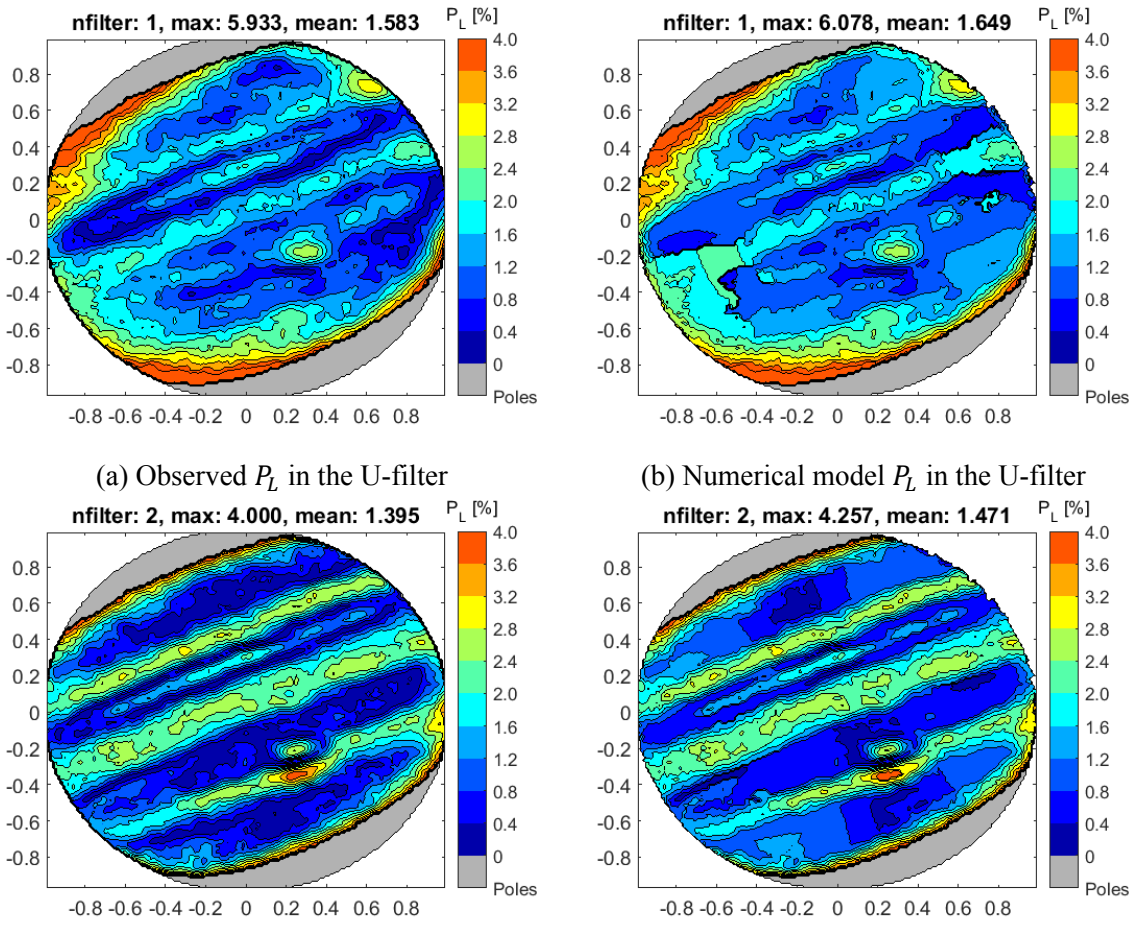

(a) Observed P_L in the U-filter

(b) Numerical model P_L in the U-filter

(c) Observed P_L in the B-filter

(d) Numerical model P_L in the B-filter

Figure 6.4: 1: Comparison of the observed and modelled P_L for the U and B-filter

The observed and modelled P_L are visualised in Figure 6.4 and 6.5 for situation 2 for all wavelength filters. The left sub-figures show the observations and the right sub-figures the result of the numerical model, the P_L-difference between the two is shown more clearly in Figure 6.6.

From Figure 6.4 and the first sub-figure of 6.6 showing the result of the U-filter, it can be seen that some low P_L regions towards the edges are difficult to fit with these particle properties. The higher P_L regions are matched closely for these particle properties for this filter. The B-filter shows similar results; the low P_L-regions at higher longitude are difficult to match while the high P_L-regions are fitted very well. The fit of the observed P_L in the V-filter is well along the entire disk, the ΔP_L of figure 6.6 shows only tiny differences. For the R-filter, the low P_L-regions towards the edges are difficult to fit as well, while the higher P_L-regions are again matched well.

The P_L-comparison for situation 2 shows that the particle properties are able to fit the high

P_L-regions well for all four wavelength filters, while the lower P_L-regions are more difficult to match well, mainly towards higher longitude. It is notable that the low P_L-regions in the V-filter are matched well by the model. The higher ΔP_L towards higher longitude likely relates to the fact that the particle properties of [McLean et al., 2017] are derived for the mid-longitude only. It is possible to add more cloud and haze particles to match the low P_L-regions better, however, it will make it more difficult to draw conclusions from the variable atmospheric parameters plc and baerh (see section 6.5).

More conclusions regarding the P_L-differences for the four wavelength filters for this situation and the corresponding variable atmospheric parameters plc and baerh are given in section 6.5.

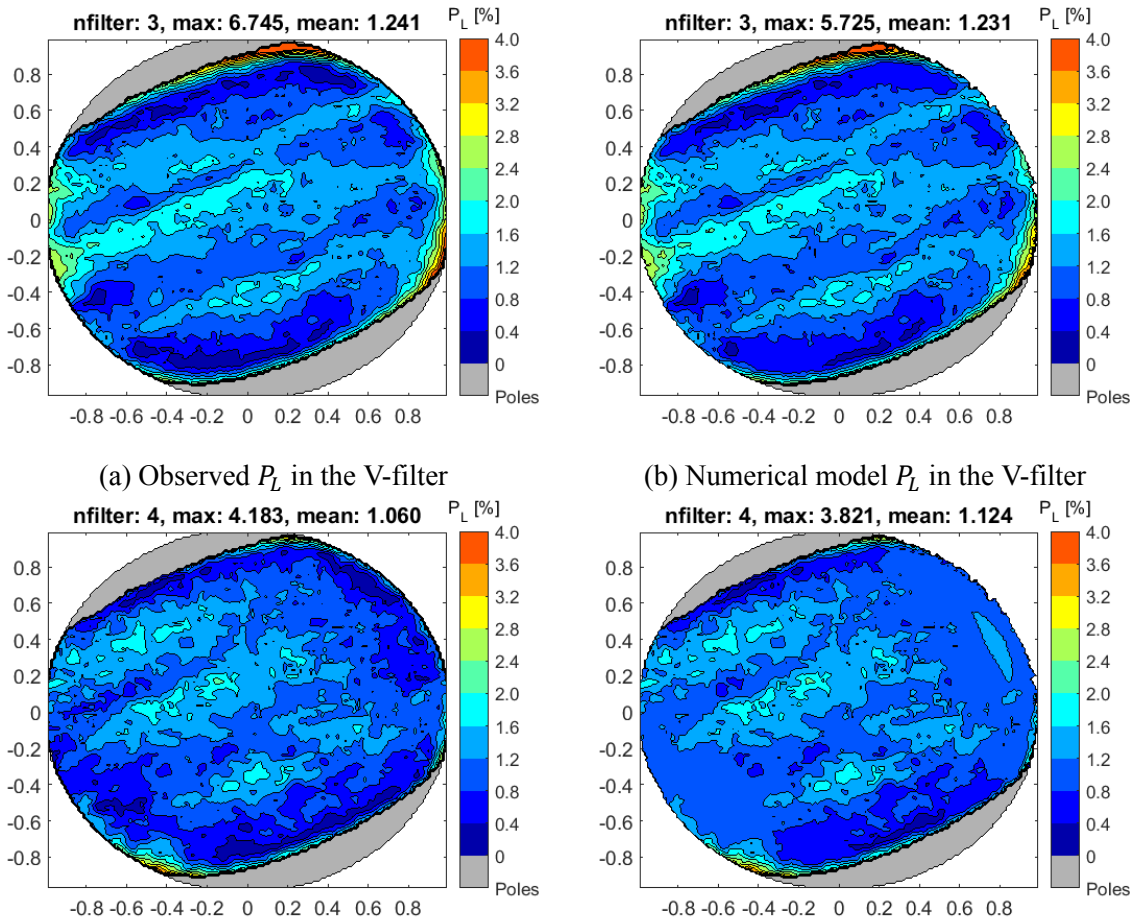

(a) Observed P_L in the V-filter

(b) Numerical model P_L in the V-filter

(c) Observed P_L in the R-filter

(d) Numerical model P_L in the R-filter

Figure 6.5: 1: Comparison of the observed and modelled P_L for the V and R-filter

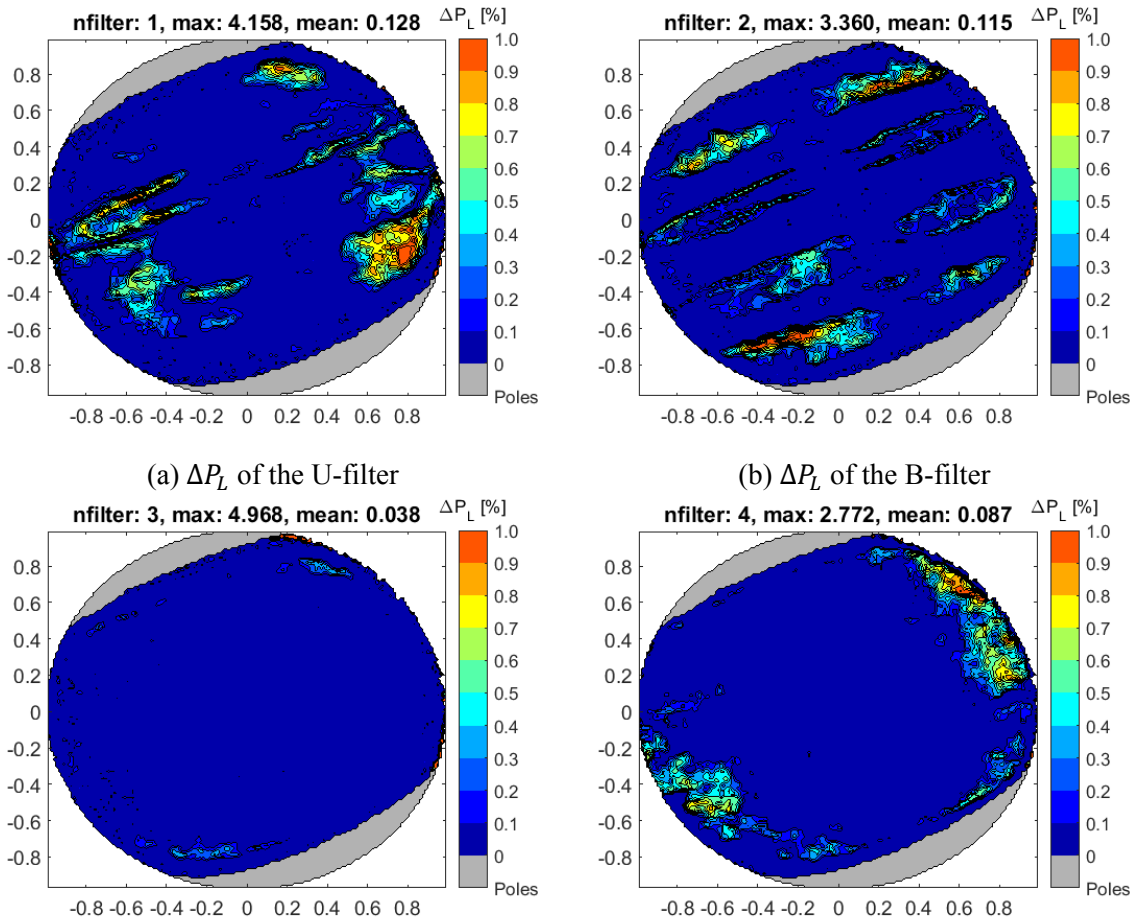

(a) ΔP_L of the U-filter

(b) ΔP_L of the B-filter

(c) ΔP_L of the V-filter

(d) ΔP_L of the R-filter

Figure 6.6: 2: P_L-difference between the observations and the numerical model

6.4. Situation 3

Situation 3 regards the smaller particles of table 6.3 and uses an approximation of the UV-absorption at lower wavelength using the imaginary part of the refractive index (nri) that approximates the geometric albedo of Jupiter. Note that the nri-values of this case are indicated in the rows with (3) added after the parameters in table 6.3.

6.4.1. The P_L Comparison

The observed and modelled P_L are visualised in Figure 6.7 and 6.8 for situation 3 for all wavelength filters. The left sub-figures show the observations and the right sub-figures the result of the numerical model. The P_L-difference between these two is shown more clearly in Figure 6.9.

Figure 6.7 and 6.9 show that the observed P_L in the U-filter is better matched compared to situation 2 due to the added approximation of UV-absorption. The low P_L-regions of the observations are now better matched, though still some ΔP_L remains. The low observed P_L-regions in the B-filter are matched well now, but the high P_L region near the great red spot (GRS) is not captured well anymore. As holds for situation 1 and 2 as well, the P_L observations in the V-filter are fitted well for the entire disk. Due to the decreased absorption of the particles

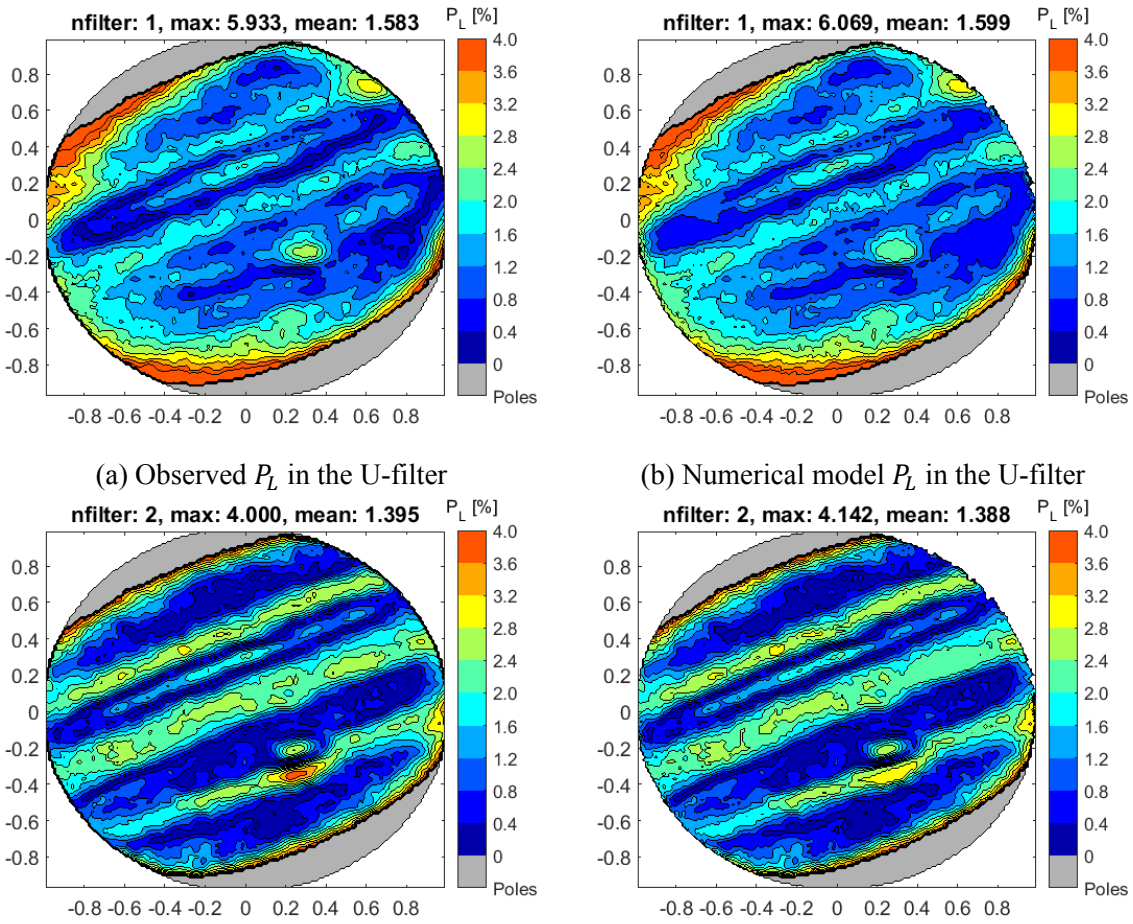

(a) Observed P_L in the U-filter

(b) Numerical model P_L in the U-filter

(c) Observed P_L in the B-filter

(d) Numerical model P_L in the B-filter

Figure 6.7: 3: Comparison of the observed and modelled P_L for the U and B-filter

at higher wavelength to approximate the geometric albedo, the high P_L region in the R-filter cannot be matched well by the model. Also, some low P_L-regions near the edges show a relative large ΔP_L.

The P_L-comparison for situation 3 shows that the particle properties are able to fit the low P_L regions of the observations well apart from some regions in the U and R-filter near the edges. The high P_L-regions are matched well except for the high P_L region near the GRS in the B-filter and the relative high P_L-region in the middle of the disk for the R-filter. It can be concluded that the addition of the approximation of UV-absorption has a positive effect on the lower P_L-regions which are generally fitted better. On the other hand, the high P_L-regions become more difficult to fit, especially the region in the middle of the disk of the R-filter.

More conclusions regarding the P_L-differences for the four wavelength filters for this situation and the corresponding variable atmospheric parameters plc and baerh are given in section 6.5.

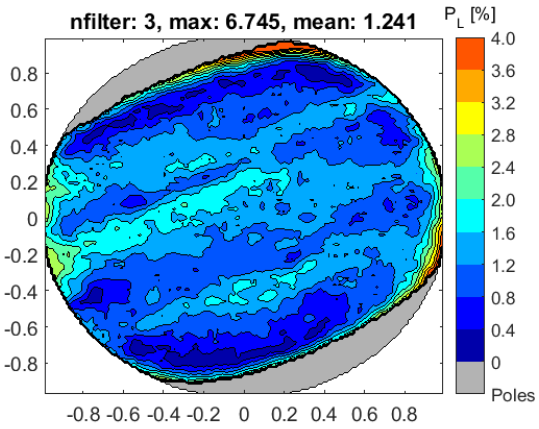

(a) Observed P_L in the V-filter

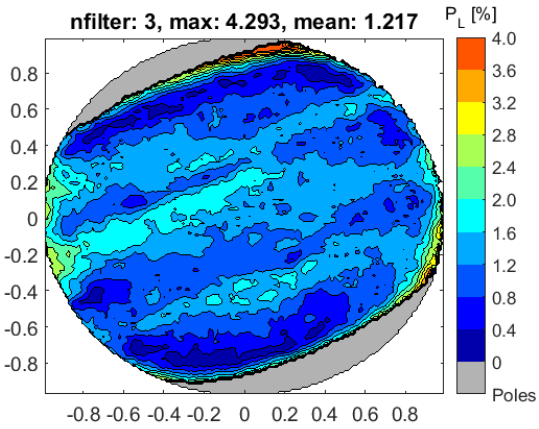

(b) Numerical model P_L in the V-filter

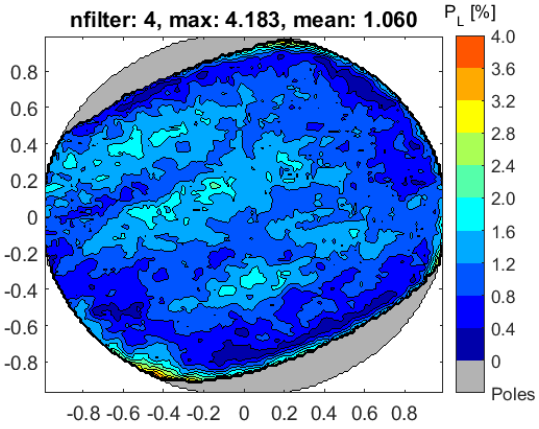

(c) Observed P_L in the R-filter

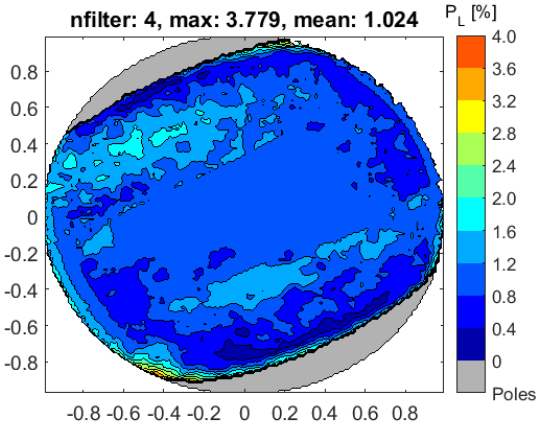

(d) Numerical model P_L in the R-filter

Figure 6.8: 3: Comparison of the observed and modelled P_L for the V and R-filter

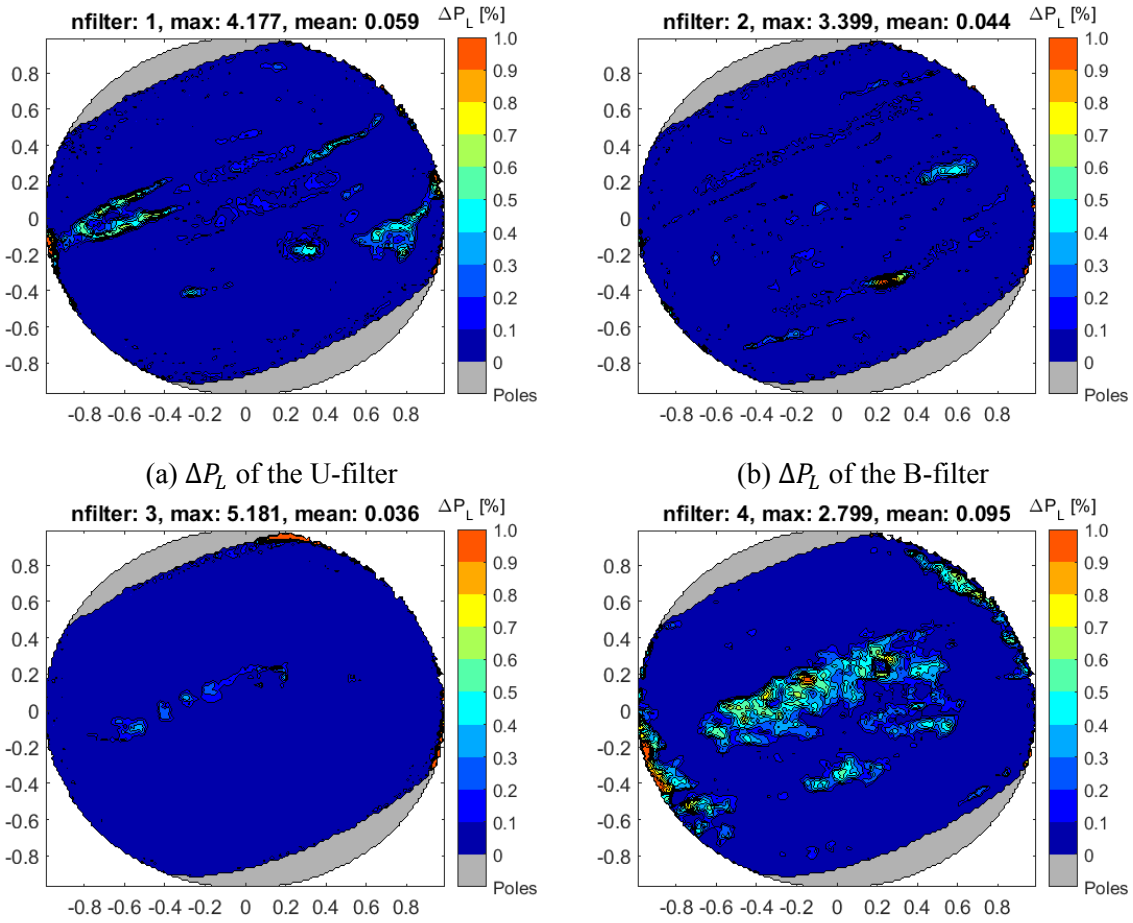

(a) ΔP_L of the U-filter

(b) ΔP_L of the B-filter

(c) ΔP_L of the V-filter

(d) ΔP_L of the R-filter

Figure 6.9: 3: P_L-difference between the observations and the numerical model

6.5. Comparison of the Three Situations

In this section the three situations are compared to each other. First, the P_L-difference is analysed in subsection 6.5.1. Afterwards, the variable atmospheric parameters of the three situations are compared against each other in subsection 6.5.2. The values of the variable atmospheric parameters based on previous research are discussed in subsection 6.5.3. The final conclusion of this comparison can be found in subsection 6.5.4.

6.5.1. Comparison of the P_L-difference

Firstly, the P_L-difference or the so-called ΔP_L is compared for the three situations per wavelength filter. The result for the U-filter is shown in figure 6.10. It can be seen that the particle properties of situation 1 and 3 fit the observed P_L better than situation 2, as the particle properties of situation 2 have difficulties fitting the lower P_L regions at higher longitude.

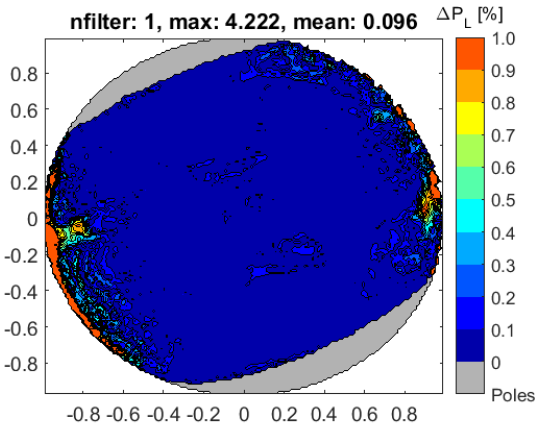

(a) Situation 1: ΔP_L of the U-filter

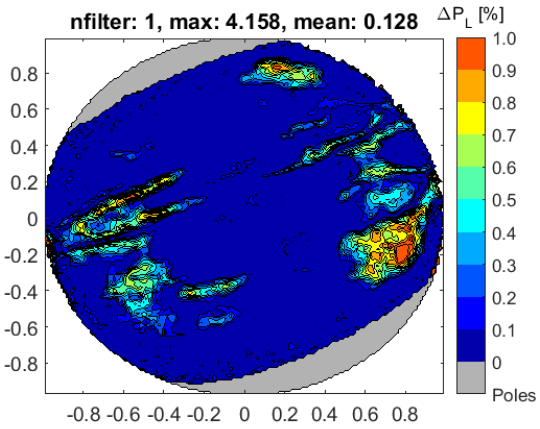

(b) Situation 2: ΔP_L of the U-filter

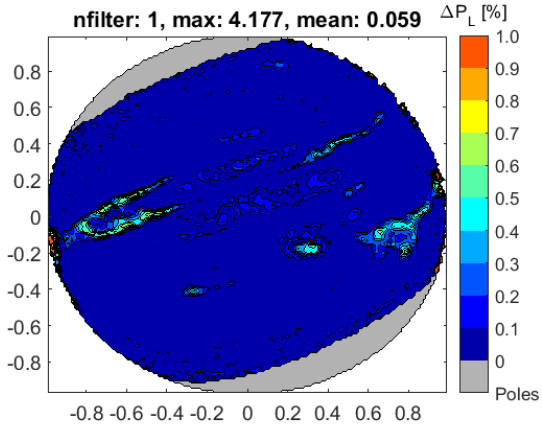

(c) Situation 3: ΔP_L of the U-filter

Figure 6.10: ΔP_L for all 3 situations in the U-filter

The B-filter is an interesting wavelength filter as it shows most visible features w.r.t. the other wavelength filters, namely, the belts, zones and the great red spot are all well visible in this wavelength filter only. It can be observed that the first situation has difficulties fitting the high P_L-regions, while situation 2 does not match the observations well for the low P_L-regions towards higher longitude. Situation 3 is able to match the observed P_L well for almost the entire

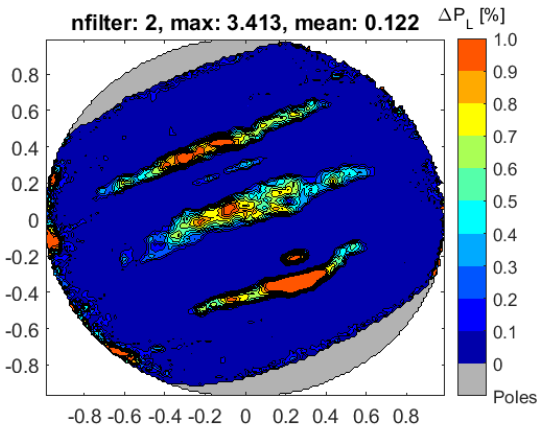

(a) Situation 1: ΔP_L of the B-filter

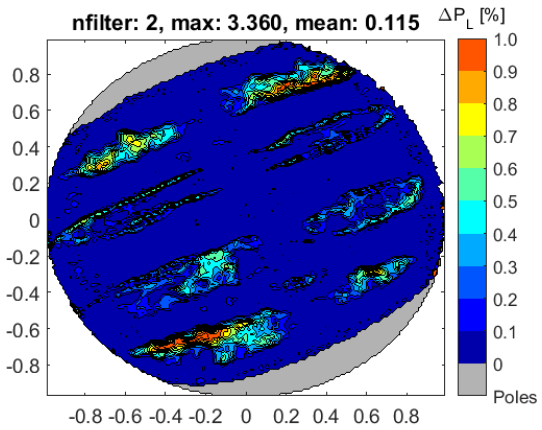

(b) Situation 2: ΔP_L of the B-filter

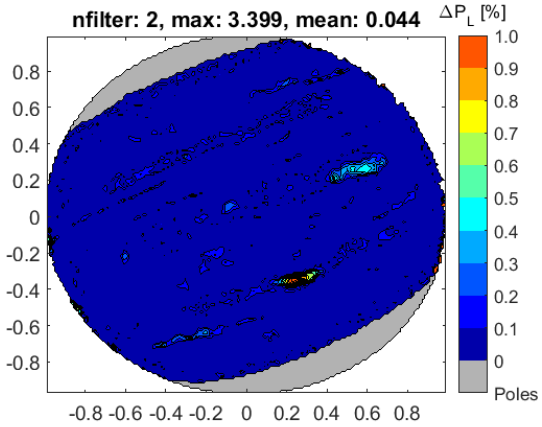

(c) Situation 3: ΔP_L of the B-filter

Figure 6.11: ΔP_L for all 3 situations in the B-filter

planet, except for the high P_L-region near the GRS and a small high P_L-region on the right of the disk near the equator. For this wavelength filter only, the particle properties of situation 3 are able to match the observations best.

The ΔP_L results for the V-filter are not shown in this comparison as the particle properties of all three situations are able to match the observed P_L well for the entire planet, except for some very small areas near the edges. These results of the V-filter are shown previously in the analyses per situation.

The ΔP_L results for the R-filter are shown in Figure 6.12 for all three situations. The R-filter is best fitted by the particle properties of situation 1, which are able to fit the observed P_L except for some small relative high P_L regions towards the left edge. The particle properties of situation 2 have difficulties with matching the low P_L regions at higher longitude and situation 3 cannot fit the middle high P_L-region well.

It turns out that it is difficult to find particle properties matching the observed P_L well for all wavelength filters along the entire disk. It is possible to include more cloud and haze particles in the analysis, as is analysed in appendix D, but this makes it more difficult to draw conclusions from the variable cloud top pressure and haze optical thickness.

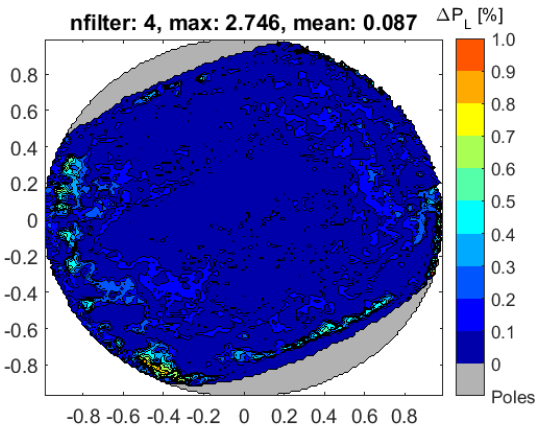

(a) Situation 1: ΔP_L of the R-filter

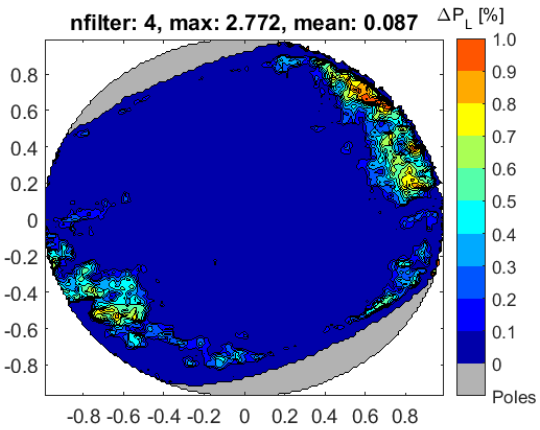

(b) Situation 2: ΔP_L of the R-filter

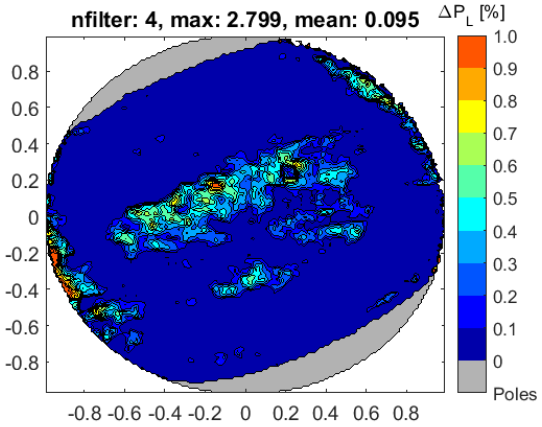

(c) Situation 3: ΔP_L of the R-filter

Figure 6.12: ΔP_L for all 3 situations in the R-filter

6.5.2. Comparison of the Variable Atmospheric Parameters

The best combination of variable atmospheric parameter values; the cloud pressure (plc) and haze optical thickness (baerh) values, are indicated per wavelength filter per situation in Figure 6.13, 6.14, 6.15 and 6.16.

The result of the U-filter is visualised in Figure 6.13. This result shows that the low P_L-regions at the edges are captured best by high altitude (low pressure) clouds for both situation 1 and 3, but low altitude clouds for situation 2. The higher ΔP_L for situation 2 at the low P_L-regions indicates that the low altitude clouds cannot fit these regions well. Consequently, this would indicate that high altitude clouds are present for the low P_L-regions at higher longitude. The haze optical thickness of the low P_L-regions towards the edges shows a different pattern; situation 1 regards an optically thin haze while situation 2 and 3 regard a significant thicker haze. The difference likely relates to the different particles used for the different situations. Again, it has to be noted that the particles of situation 2 and 3 based on [McLean et al., 2017] have been derived for the mid-longitude only, such that deviations towards higher longitude may arise. Also, it can be observed that the lower P_L regions at higher longitude are fitted by a high haze optical thickness for situation 2 and 3. This relates to the depolarising effect of the haze in this case, such that an optically thicker haze results in lower P_L values. The fit of these low P_L regions is likely better for situation 3 due to the added approximation of UV-absorption.

On the middle of the disk the higher observed P_L-regions correspond to the zones and the great red spot. For situation 1 these higher P_L-regions correspond to a higher optical thickness of the haze, while the lower P_L-regions have a lower haze optical thickness. The cloud altitude of situation 1 does not show clear patterns for the middle of the disk, which likely relates to over-fitting of the observed P_L. The same high observed P_L-regions at the centre part correspond to high altitude clouds and a thin overlaying haze for situation 2 and 3, while the lower P_L belts have lower clouds and a thicker haze.

The U-filter in combination with situation 2 and 3 shows patterns for the mid-longitudes revealing that the higher P_L zones correspond to low pressure/high altitude clouds and a thin haze layer while the lower P_L belts show lower altitude clouds and an optically thicker haze layer.

The analysis of the B-filter is depicted in Figure 6.14. As mentioned previously, the B-filter shows most features w.r.t. the other wavelength filters; the belts, zones and GRS. The high observed P_L regions corresponding to the zones are best fitted for all situations by low pressure, high altitude clouds. For situation 1 and 3 this is only true up to a certain longitude. The low P_L regions, the belts, are matched by low altitude clouds for situation 2, while situation 1 and 3 show less distinct patterns but lower altitude clouds compared to the zones. Situation 1 and 3 show a zero valued haze optical thickness (no haze) for the high P_L regions corresponding to the zones and GRS and a higher value for the belts. This again relates to the depolarising effect of the haze layer in this case. Therefore, no haze at all provides the highest P_L response. The particles of situation 2 can capture the highest P_L values with a low but non-zero valued haze optical thickness. This indicates that the particles of situation 2 have the potential to reach the highest P_L values compared to situation 1 and 3. On the other hand, the lower P_L regions become more difficult to match. Also, from the results of the B-filter it can be seen that the particle properties of situation 2 cannot match the low P_L belts at high longitude, while the particle properties of situation 3 can. The only difference in particle properties between these situations is the added approximation of UV-absorption to situation 3. This likely indicates that UV-absorption is at least partially caused by absorption of the haze layer.

From the B-filter and the three different situations it is observed that the zones and GRS having a larger P_L are matched by low pressure/high altitude clouds and a low haze optical thickness. The belts having a lower P_L are fitted by lower clouds and an optically thicker haze. Towards higher longitude, these patterns become less distinct.

The P_L observations of the V-filter show some P_L-variation between the belts and zones, but significantly less compared to the B-filter. For situation 1 and 2 no distinct patterns in the cloud pressure/altitude can be seen. Situation 3 shows a low pressure/high altitude cloud for the zone around the equator, but on the rest of the disk no clear patterns can be distinguished as well. Situation 1 shows a high haze optical thickness in the high P_L regions, and a lower value for the lower P_L regions. This indicates that P_L in the V-filter for the particle properties of situation 1 is more sensitive to baerh than to plc. Situation 2 shows generally an optical thick haze for the low P_L regions and a lower baerh for the high P_L regions. This again relates to the depolarising effect of the haze in this case. Note that the baerh values are significant for situation 2 along the entire disk. Situation 3 shows no haze in the centre region, which likely relates to the lower nri-value of the cloud w.r.t. situation 2.

From the V-filter it is difficult to draw conclusions regarding all three situations as the re-

sults deviate significantly. All three situations are able to match the observed P_L closely, such that over-fitting of the observations occurs. The lower sensitivity of P_L to this wavelength filter and to the cloud pressure and haze optical thickness in this wavelength filter makes it difficult to derive distinct patterns as well. The P_L result for the higher wavelength filters is more sensitive to the particle properties and three different particle properties are used. The combination of all these aspects makes that no consistent results can be derived from this wavelength filter.

The P_L observations of the R-filter show some P_L variation between the belts and zones for the mid-longitudes, but again significantly less compared to the B-filter. The low P_L regions at the edges and towards the poles are fitted by high pressure/low altitude clouds for situation 1 and low pressure/high altitude clouds for situation 2 and 3. For the lower longitudes, no distinct patterns in cloud pressure can be distinguished. Note that the high altitude clouds of situation 3 result in a relative high ΔP_L such that it is questionable whether that profile is realistic. Situation 1 matches the low P_L regions by not considering a haze layer (baerh=0) while the centre region is fitted by an optically thicker haze. This indicates that for situation 1 the R-filter is more sensitive to baerh than to plc. For situation 2 and 3, the lower P_L regions near the edges and poles correspond to a haze optical thickness that increases towards the centre part up to a certain extent. For the centre region no haze (baerh=0) is considered for situation 3, while for situation 2 no distinct patterns in haze optical thickness can be observed.

From the R-filter it is difficult to draw conclusions regarding the three situations as well. The reasons for that are very similar to the conclusions drawn from the U-filter, mentioned in the previous paragraph.

6.5.3. Previous Research on the Variable Atmospheric Parameters

In the past, several research has been performed on the atmospheric parameters of Jupiter, including the cloud pressure and haze optical thickness. This sub-section touches upon a selection of the findings to be able to compare these with the found results in this analysis.

Based on an assortment of ground-based and spacecraft observations, research of [West et al., 1986] suggests the highest ammonia-ice cloud pressure to range approximately between 0.3 and 0.7bar. [Sromovsky and Fry, 2002] regards the measurements of the Galileo probe and interpreted the observations with a probe-compatible cloud model with an upper cloud with a cloud top pressure of 0.44bar. [McLean et al., 2017] found a cloud top pressure of 0.56bar for the zones using polarimetric analysis. Also, polarimetric research performed by [Fernández Jiménez, 2018] resulted in cloud top pressures up to 0.750bar. From these results, it can be seen that the found maximum cloud top pressure of 0.36bar is not extremely high and is in conformance with previous research. The cloud pressure of the lower clouds in the belts which range from 1.778bar to 1.000bar are in conformance with previous research as well. The cloud top pressure for the lower clouds in [McLean et al., 2017] is up to 1.778bar, which is the case for this analysis as well. [Fernández Jiménez, 2018] finds cloud top pressures of the upper clouds of 2.371, 1.334 and 1.000bar in the analysis as well as the previously mentioned 0.750bar. Research by [Sromovsky and Fry, 2002]) considers more than one cloud and the middle cloud (supposing in the belts no upper thinner cloud used in [Sromovsky and Fry, 2002] is present) has a top pressure in the order of magnitude of 1.0 to 1.35bar. It can indeed be noted that the cloud top pressure found in this analysis is similar to the values found in previous related research.

The optical thickness values of the haze layer are chosen in conformance with previous research performed by (among others) [West et al., 2004], [McLean et al., 2017] and [Fernández Jiménez, 2018]. [West et al., 2004] found an optical thickness of the haze of about 0.05 to 0.1 for the centre region and a thicker haze of about 2 to 7 at the poles. [McLean et al., 2017] found a haze optical thickness of 0.1 to 0.225 at low and mid latitude and of 3 for the polar latitudes. Finally, [Fernández Jiménez, 2018] found an optical thickness of the haze of 0.2 for the great red spot which is situated in a region of similar haze optical thickness found in this analysis.

6.5.4. Conclusion of the Comparison

The analysis of the difference in degree of linear polarisation of the observations and the numerical model shows that it is difficult to fit Jupiter's entire disk well with one type of cloud and haze particle. Despite this fact, it is chosen to do so in order to be able to make a valuable comparison in terms of the two variable atmospheric parameters being the cloud pressure and the haze optical thickness.

The particle properties of situation 1 cannot capture the high P_L regions appearing in the B-filter and the outer edge of low P_L values in the U-filter. The rest of the disk can be matched well in all wavelength filters when optimising per wavelength filter. The cloud pressure shows most distinct patterns in the U and B-filter where low pressure/high altitude clouds are suggested for the low P_L regions at higher longitude and for the high P_L regions at lower longitude. Note that the clouds at high P_L regions at lower longitude cannot match the observed P_L well although they are the best possible match. The V and R-filter are not sensitive enough to plc to show distinct patterns. According to the V and R-filter, the optical thickness of the haze has a high value for higher P_L in these filters and a lower (or zero) value at lower P_L (up to a certain longitude). This observation is in conformance with the baerh-result of the U-filter.

The particle properties of situation 2 are in conformance with [McLean et al., 2017] and therefore fit the observed P_L around zero longitude particularly well as this analysis optimises the parameter values at zero longitude. On the other hand, the observed P_L at higher longitude is more difficult to fit with these particles. Still, the parameter values around zero longitude provide useful information. The high P_L regions at lower wavelength which correspond to the zones are matched by low pressure/high altitude clouds and low haze optical thickness. The low P_L regions corresponding to the belts are fitted by high pressure/low altitude clouds. The haze optical thickness does not show distinct patterns besides the high values at higher longitude, which are unrealistic due to the high ΔP_L.

The particle properties of situation 3 are in conformance with [McLean et al., 2017] except for the value of nri which is approximated using the geometric albedo as explained in section 4.4. The observed P_L can be matched well for most of the wavelength filters, except for the high P_L region in the R-filter and some small low P_L regions in the U-filter. The results show low pressure/high altitude clouds in combination with a low (or zero) valued haze optical thickness for the high P_L-regions known as the zones in all wavelength filters. Additionally, the belts are fitted by higher pressure/lower altitude clouds and a higher optical thickness of the haze. At higher longitude the plc and baerh values start to deviate from the afore-mentioned patterns,

which is related to the lower accuracy of the numerical model towards higher longitude.

The three situations complement to each other and show some general aspects. Firstly, it is important to note that P_L is highly sensitive to both the particle properties and the wavelength, which makes it difficult to draw conclusions for the optimisation per wavelength filter.

From the V and R-filter it is difficult to draw conclusions regarding all three situations as the results deviate significantly. The lower sensitivity of P_L to these wavelength filters and to the cloud pressure and haze optical thickness in these wavelength filters makes it difficult to derive distinct patterns in cloud pressure and haze optical thickness. The P_L result for the higher wavelength filters is more sensitive to the particle properties and three different particle properties are used. The combination of all these aspects makes that no consistent results can be derived from both the V and R-filter.

From the B-filter which is most P_L sensitive, it can be seen that the high P_L regions corresponding to the zones and GRS show low pressure/high altitude clouds and low or zero valued haze optical thickness. The lower P_L regions corresponding to the belts consists of lower pressure/higher altitude clouds in combination with an optically thicker haze. The same can be seen from the mid-longitude part of the U-filter which shows the belts and zones as well. These observations are in conformance with previous research of subsection 6.5.3. Furthermore, the low P_L belts at higher longitude cannot be matched by the particle properties of situation 2 while the particle properties of situation 3 can. The only difference between these situations is the added UV-absorption approximation to situation 3. This likely indicates that UV-absorption is at least partially causes by absorption of the haze layer.

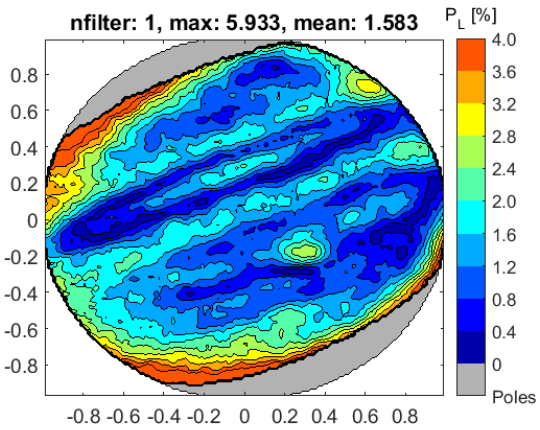

(a) Observed P_L in the U-filter

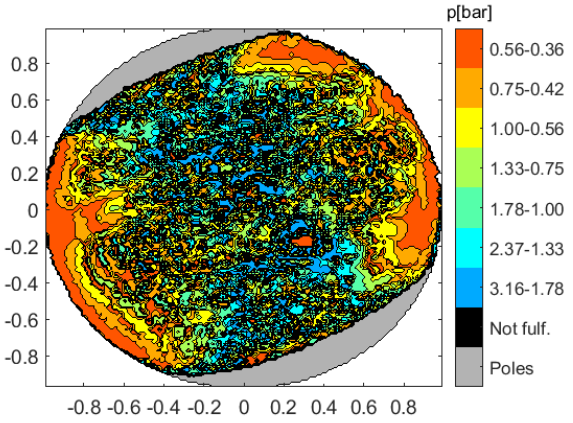

(b) 1: plc minimising ΔP_L for the U-filter

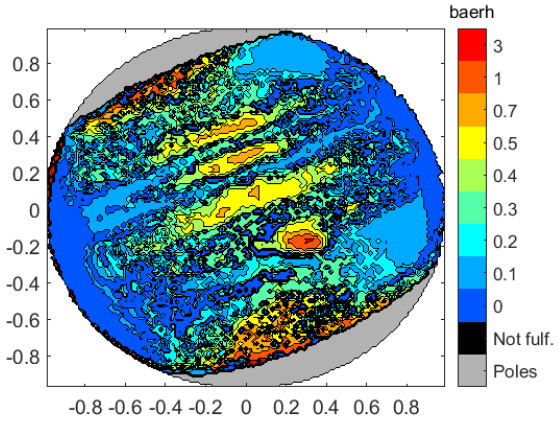

(c) 1: baerh minimising ΔP_L for the U-filter

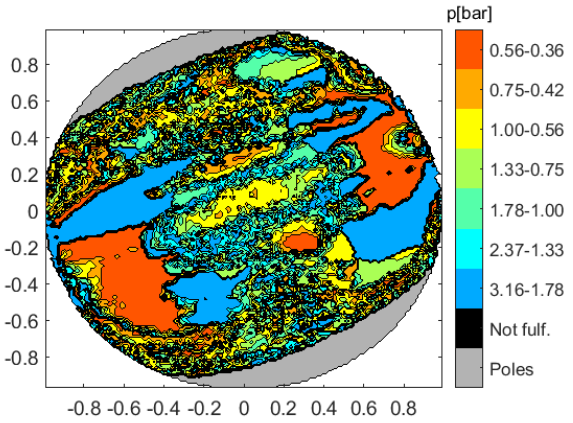

(d) 2: plc minimising ΔP_L for the U-filter

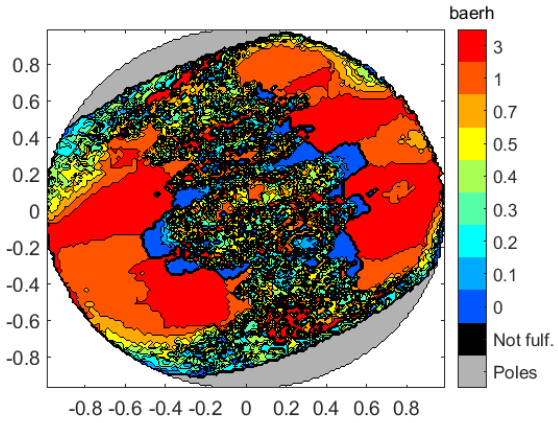

(e) 2: baerh minimising ΔP_L for the U-filter

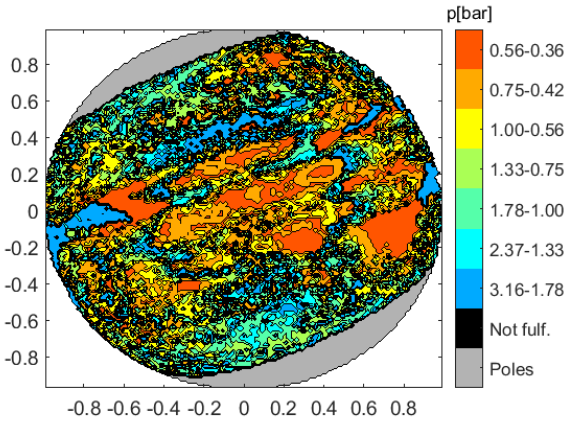

(f) 3: plc minimising ΔP_L for the U-filter

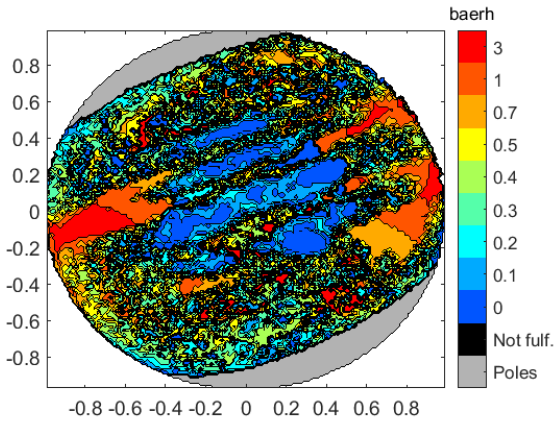

(g) 3: baerh minimising ΔP_L for the U-filter

Figure 6.13: The plc and baerh values minimising ΔP_L for the U-filter

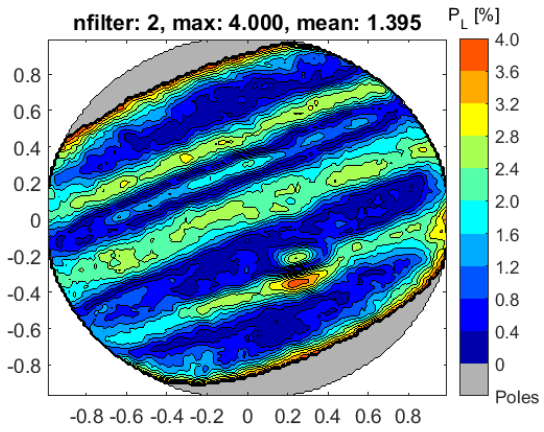

(a) Observed P_L in the B-filter

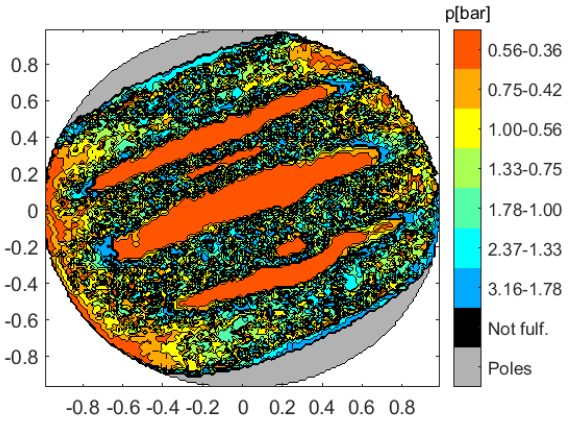

(b) 1: plc minimising ΔP_L for the B-filter

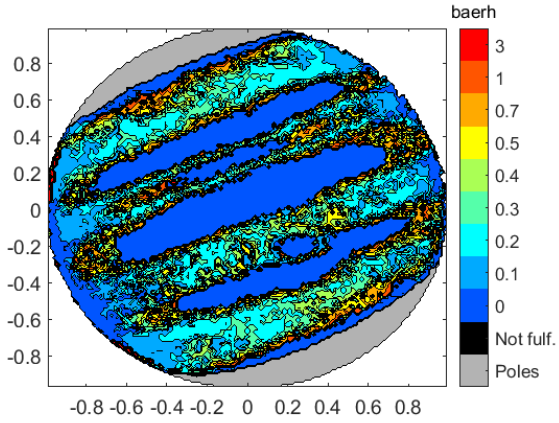

(c) 1: baerh minimising ΔP_L for the B-filter

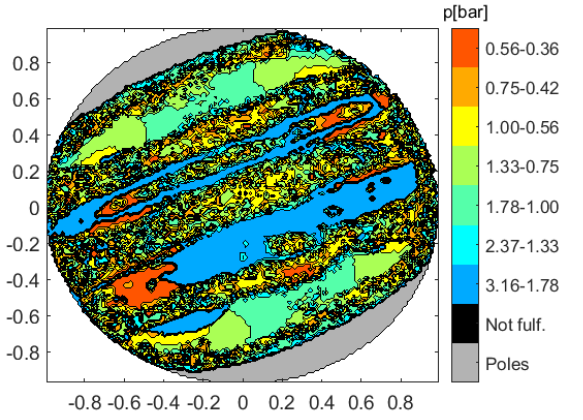

(d) 2: plc minimising ΔP_L for the B-filter

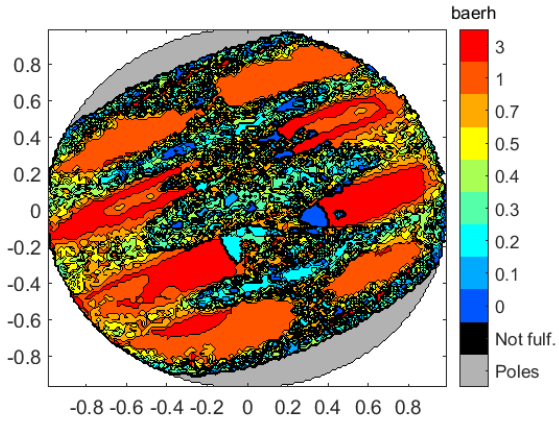

(e) 2: baerh minimising ΔP_L for the B-filter

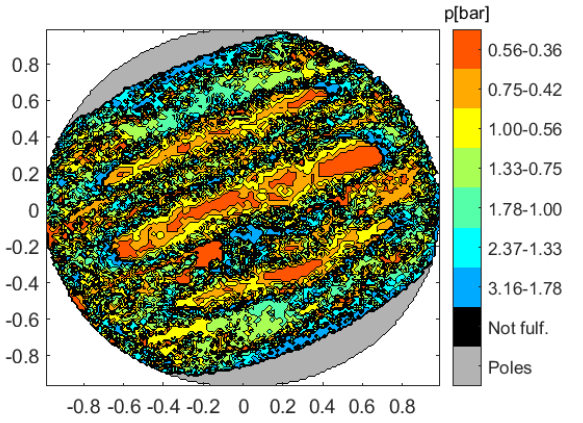

(f) 3: plc minimising ΔP_L for the B-filter

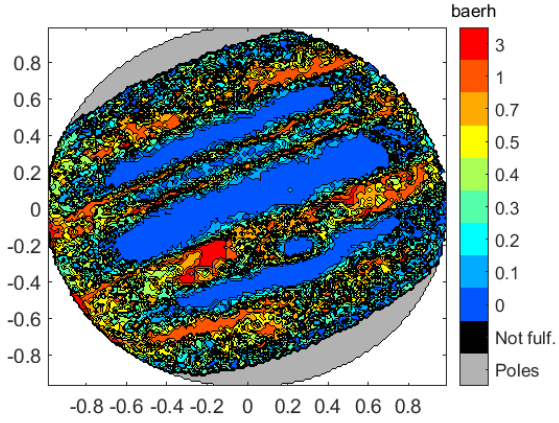

(g) 3: baerh minimising ΔP_L for the B-filter

Figure 6.14: The plc and baerh values minimising ΔP_L for the B-filter

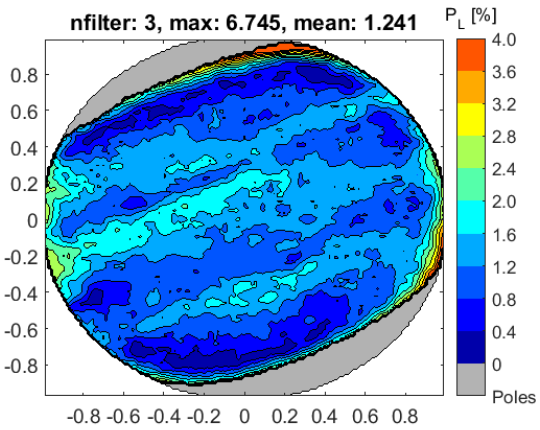

(a) Observed P_L in the V-filter

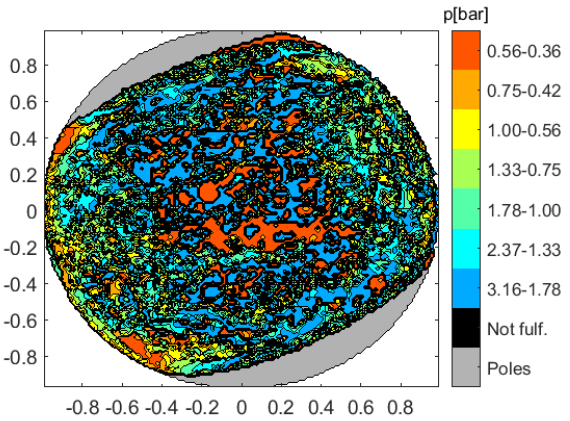

(b) 1: plc minimising ΔP_L for the V-filter

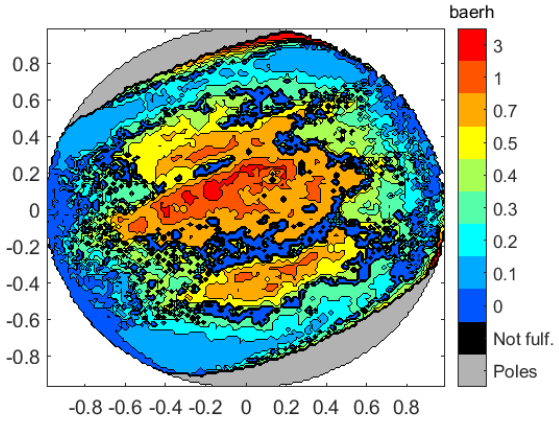

(c) 1: baerh minimising ΔP_L for the V-filter

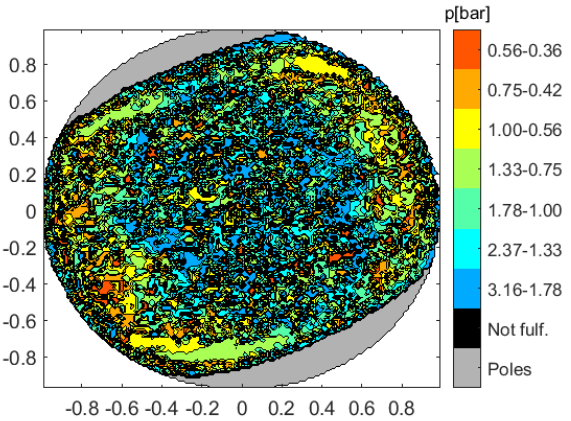

(d) 2: plc minimising ΔP_L for the V-filter

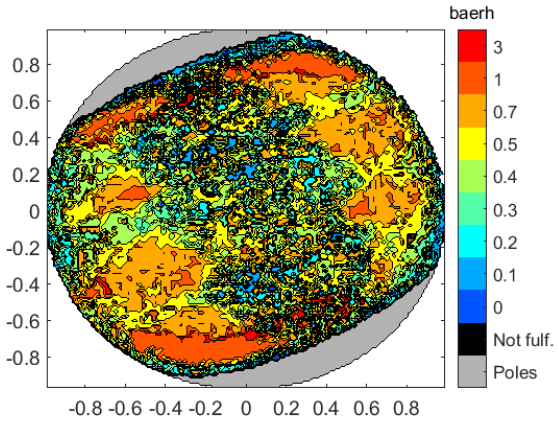

(e) 2: baerh minimising ΔP_L for the V-filter

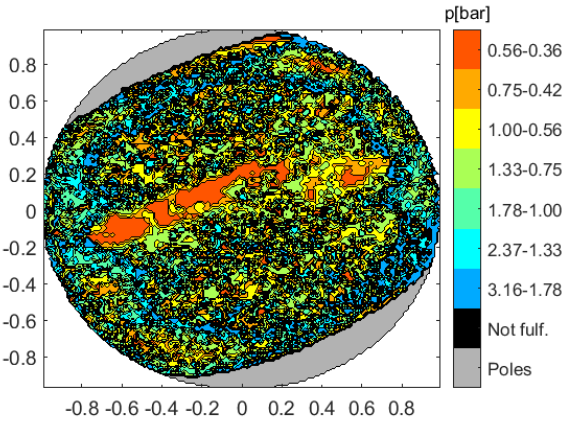

(f) 3: plc minimising ΔP_L for the V-filter

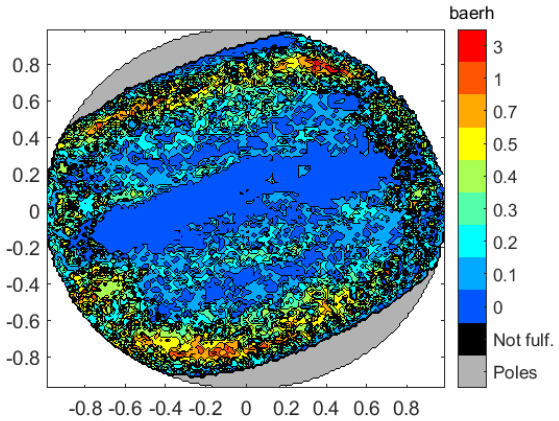

(g) 3: baerh minimising ΔP_L for the V-filter

Figure 6.15: The plc and baerh values minimising ΔP_L for the V-filter

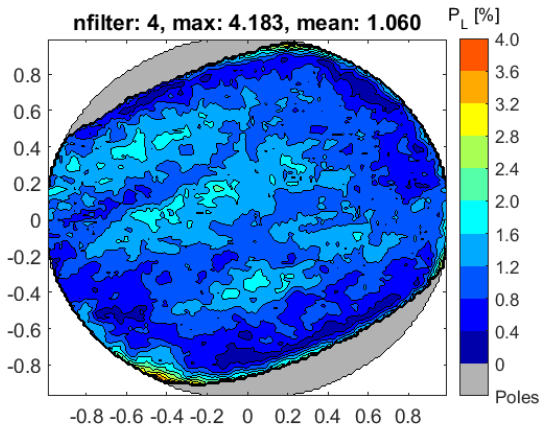

(a) Observed P_L in the R-filter

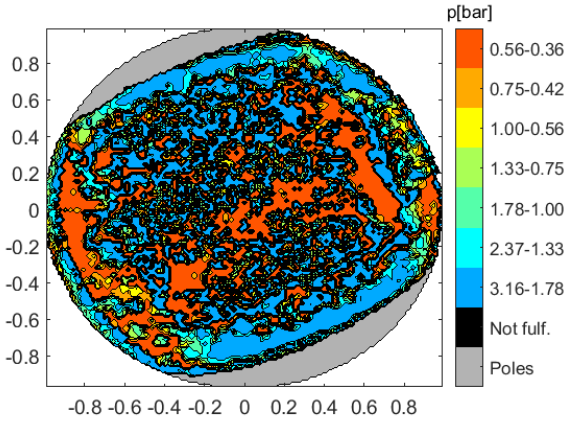

(b) 1: plc minimising ΔP_L for the R-filter

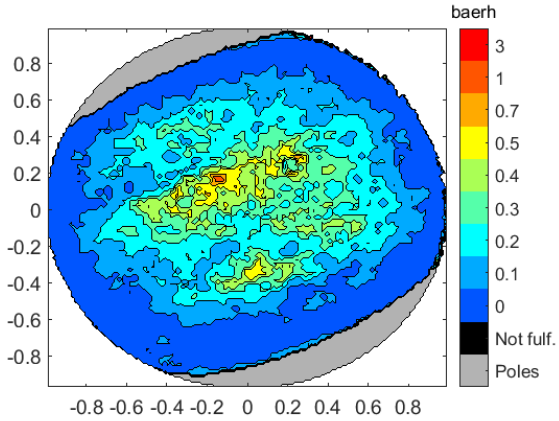

(c) 1: baerh minimising ΔP_L for the R-filter

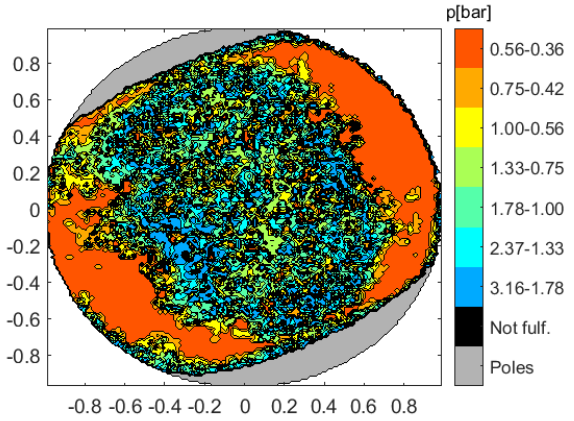

(d) 2: plc minimising ΔP_L for the R-filter

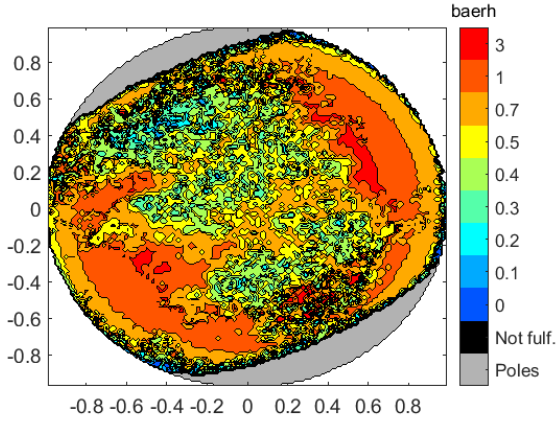

(e) 2: baerh minimising ΔP_L for the R-filter

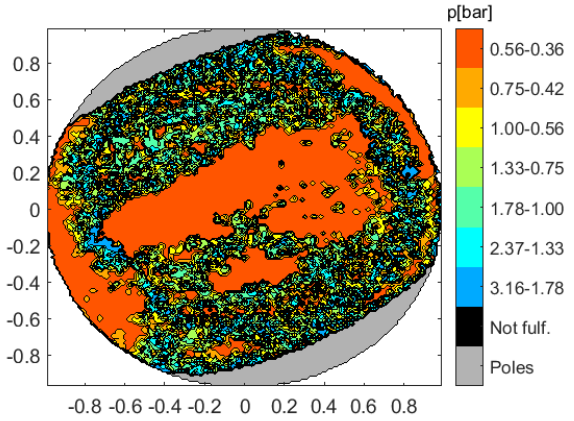

(f) 3: plc minimising ΔP_L for the R-filter

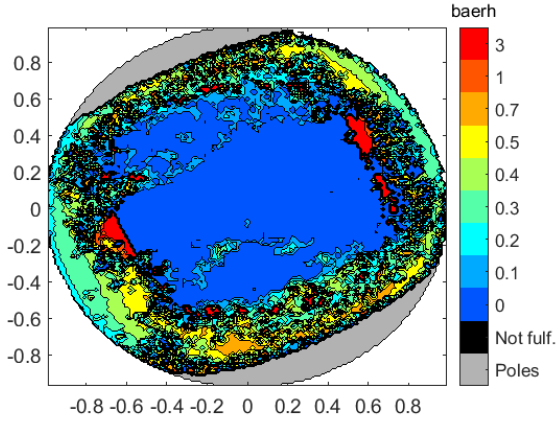

(g) 3: baerh minimising ΔP_L for the R-filter

Figure 6.16: The plc and baerh values minimising ΔP_L for the R-filter

6.6. Comparison of the Flux

Besides the comparison of the observed P_L with the numerical model, the observed non-calibrated flux values can be compared to the flux of the numerical model as well. In this way, it can be shown that the atmospheric properties are more sensitive to polarimetry than to spectrometry alone.

The non-calibrated and normalised flux of the observations is shown in Figure 6.17 on the left. The normalised flux indicates that the sum of all flux values along the disk equals one. The observed non-calibrated flux is namely given as a number of photons falling on the detector, which cannot be compared directly to the numerical model flux. The non-calibrated state of the flux means that the flux results are not calibrated w.r.t. standard distant stars with known flux output. Additionally, variation along the detector pixels due to different sensitivity is unknown, which holds as well as for the instrument transmission. From the observations only, it can directly be seen that the sensitivity is lower compared to the polarimetric observations as the variation with wavelength and the variation along the disk are much lower.

The flux results from the numerical model for situation 3 with variable plc and baerh along the disk are shown in Figure 6.17 on the right. Although due to accuracy reasons (calibration) only a quantitative comparison is possible, it can be seen that the lower and higher flux values occur at approximately the same locations.

The non-calibrated observed flux shows less detail compared to the numerical model flux as the observations are performed through Earth's atmosphere which causes the pixel values to have a spread out effect. It can be seen that the non-calibrated flux variation with wavelength is much smaller compared to the P_L-variation. In this way, it is possible that similar atmospheric property values of the numerical model result in a good match of the observations and thereby not constraining the atmospheric properties. On the other hand, as polarimetry is much more sensitive to the atmospheric properties, the atmospheric property optimisation procedure becomes much more complicated.

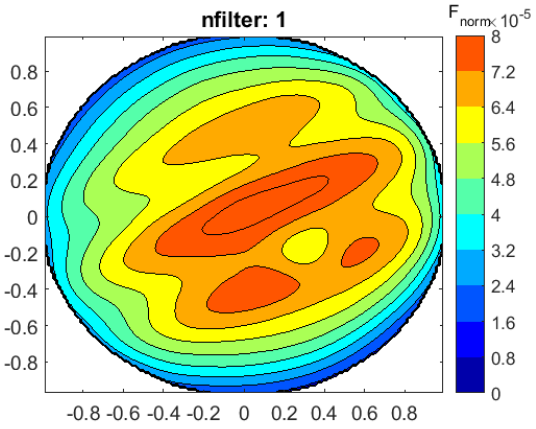

(a) Observed Flux in the U-filter

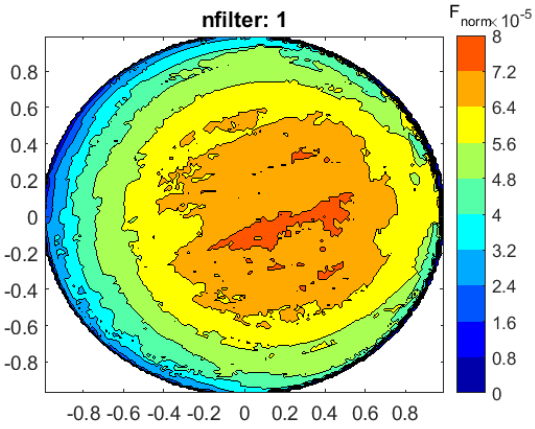

(b) Modelled Flux in the U-filter

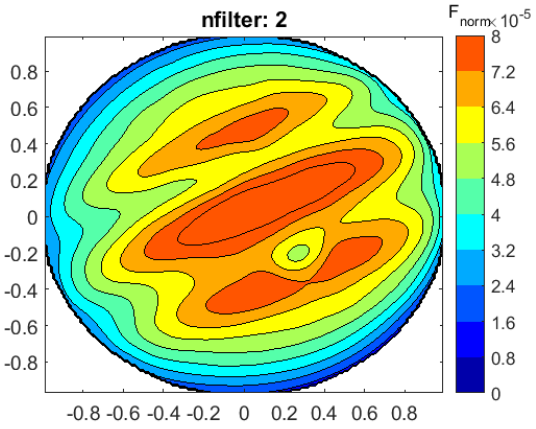

(c) Observed Flux in the B-filter

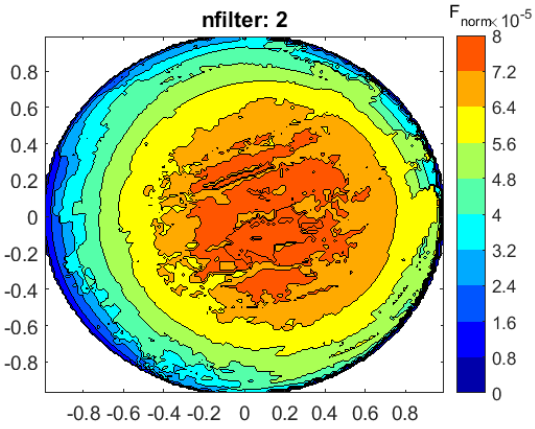

(d) Modelled Flux in the B-filter

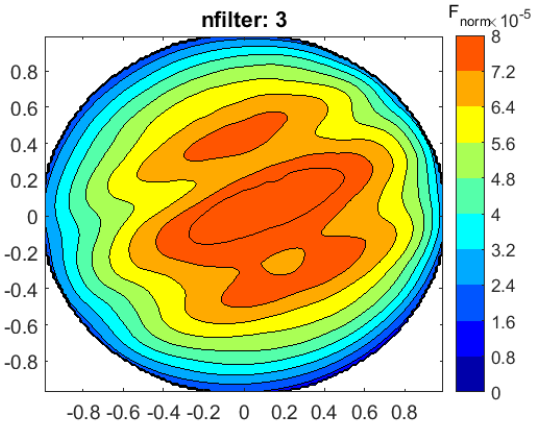

(e) Observed Flux in the V-filter

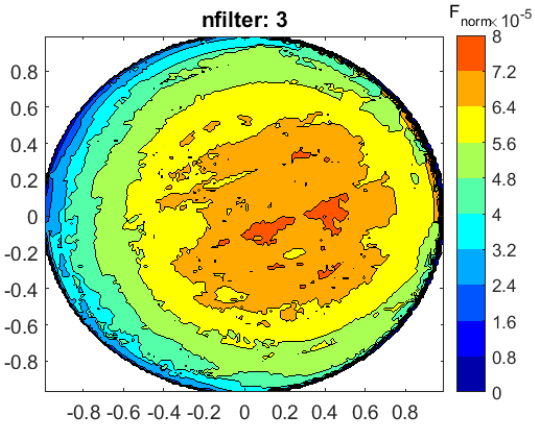

(f) Modelled Flux in the V-filter

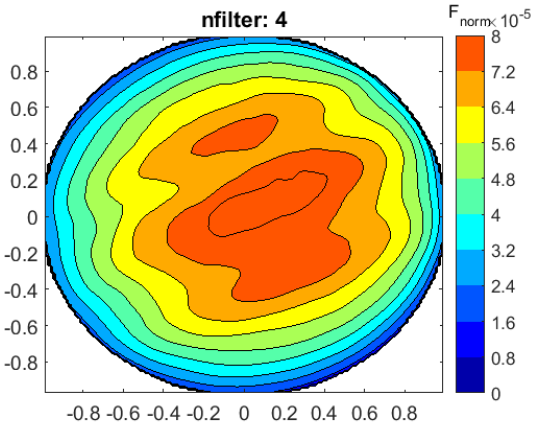

(g) Observed Flux in the R-filter

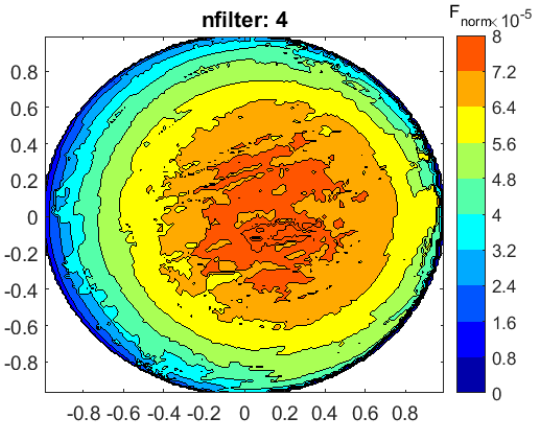

(h) Modelled Flux in the R-filter

Figure 6.17: Observed and modelled Flux

7

Conclusions

Disk resolved polarimetric observations in four wavelength filters are compared to results from the numerical atmospheric model for three different situations. Situation 1 regards larger particles w.r.t. situation 2 and 3, and situation 3 uses an approximation of UV-absorption.

The cloud pressure layer (plc) and optical thickness of the haze (baerh) are kept variable to model the P_L variation along Jupiter's disk. The best combination of these plc and baerh minimising the P_L-difference per wavelength filter is evaluated per pixel.

It is shown that the high P_L regions in the B-filter corresponding to Jupiter's zones and the GRS are modelled by high altitude clouds with a top pressure up to 0.36bar, while the lower P_L belts are modelled by lower altitude clouds with a bottom pressure up to 3.16bar. The cloud top pressures are in compliance with research of [West et al., 1986], [Sromovsky and Fry, 2002], [McLean et al., 2017] and [Fernández Jiménez, 2018]. The patterns in cloud pressure can mainly be seen from the lower wavelength filters as the cloud pressure is most sensitive at lower wavelength, due to the influence of the gas via scattering. This answers the research question regarding the pressure profile of the aerosol layers.

For situation 1 and 3, the high P_L regions of the B-filter show a low (or zero) valued haze optical thickness, while the lower P_L regions show an optically thicker haze. This result is in conformance with previous research of [West et al., 2004], [McLean et al., 2017] and [Fernández Jiménez, 2018].

Situation 2 shows a significantly high haze optical thickness for the low P_L belts at higher longitude as it is tried to match the low P_L values this way. Due to the depolarising effect of the haze a higher haze optical thickness results in a lower P_L value. Even with this high haze optical thickness value the particle properties of situation 2 cannot match these regions, while the particle properties of situation 3 can. The only difference between these situations is the approximation of UV-absorption added to situation 3. This observation therefore likely indicates that the UV-absorption is at least partially caused by absorption of the haze particles.

Towards higher longitude, it becomes more difficult to distinguish distinct patterns in both plc and baerh matching the observed P_L best. This is possibly related to the decreased accuracy of the numerical model at high longitude as the twilight zone is not considered in the numerical model.

The exact particle properties of the cloud and haze layer are more difficult to pinpoint than the cloud pressure and the haze optical thickness. From this research it is found that no particular particle fits the polarimetric observations significantly better than other particles.

This relates to the fact that the exact sensitivity of P_L to the wavelength filters and the position on the disk is unknown. In this way, a difference in ΔP_L between the wavelength filters and positions along the disk cannot be compared one-to-one. Therefore, three different situations are regarded to compare the results of different particle property combinations.

The optimisation procedure in which the observed P_L is compared to the results of the numerical model per wavelength filter per pixel, shows a good fit for most of the visible disk. All three situations show some higher P_L-difference regions for particular wavelength filters, which relate to the particular particle properties that cannot capture some low or high P_L regions. Despite the aforementioned, these results still provide useful information.

Jupiter's upper atmospheric structure derived from the polarimetric observations thus indicates higher altitude clouds in the higher P_L zones and lower altitude clouds in the lower P_L belts, which is in conformance with previous research. Additionally, the haze optical thickness is low or zero in the zones and higher in the belts, which is confirming previous research as well.

8

Recommendations

Jupiter is situated in the outer solar system and although the fact that nine satellite missions collected data of the red gas giant, still the current knowledge of its atmosphere is limited. The observational polarisation data of the ToPol is compared to the data generated by the numerical atmospheric model. However, due to various unknowns, assumptions and approximations the accuracy of the comparison can be significantly improved. Therefore, this chapter touches upon the most prominent improvements possible to better characterise Jupiter's upper atmosphere.

First of all, more research can be performed to constrain the particle and atmospheric properties even more. This aspect is bound by the available time, especially when generating higher accuracy data. Therefore, it can be useful to link the Fortran and Matlab code to directly suggest new parameter values and use them as new input to decrease the computation time. With this link even automation of the optimisation procedure becomes possible. However, which relates directly to the next recommendation, the added value of such an optimisation procedure is limited as it is difficult to compare the performance of different parameter value combinations. This relates to the fact that the exact sensitivity of P_L to the wavelength filters and the position along the disk is unknown. In this way, a difference in ΔP_L between the wavelength filters and positions along the disk cannot be compared one-to-one. Consequently, it is difficult to attribute accurate weight factors to the different wavelength filters and positions along the disk to consider this effect. Therefore, it is essential to investigate the exact sensitivity of P_L to the wavelength filters and the position on the disk. To mitigate this effect, the optimisation is performed per wavelength filter per pixel in this case.

The observations of the ToPol are not fully accurate due to various sources. By analysing these error sources and quantifying them in more detail, the error boundaries can be determined. This information is important in the comparison of the observations with the numerical model to define the comparison accuracy.

To gain information about the atmospheric properties along the entire disk, a space mission carrying a polarimeter on board can help a lot. Several missions in the past carried a photo-polarimeter on-board; the Pioneer missions (1972,1973 [Opp, 1974]), the Voyager missions (1977, [Stone, 1981] data analysis among others in [West, 1981], [West et al., 1981]) and the Galileo orbiter (1989, [Taylor, 2001], data analysis among others in [Atreya et al., 2003]) In this way, the planetary phase angle range would be extended from about 12° (for ground-based observations) to the full range (0 to 180°) which provides additional information, which helps

constraining the atmospheric properties of the upper atmosphere. Additionally, with a space mission larger variations in polarisation can be measured. Furthermore, the noise error due to the close distance of the orbiter to Jupiter can be diminished and the seeing limitation of a ground-based instrument is mitigated. Additional collected data might help in other ways, as to identify the high P_L variation regions or to take both UV and methane absorption more accurately into account in the numerical model.

Additionally, a space mission carrying several probes on board can help. With a probe going down in Jupiter's atmosphere, which is done in the past, the atmospheric properties could be measured directly. However, it is difficult to penetrate into the deeper atmospheric layers due to the high pressure and temperature. Also, the variation in atmospheric properties can only be deduced by penetrating the atmosphere at many different locations, which makes it a suitable option for obtaining local atmospheric properties only.

One cloud and haze particle are regarded per situation in this analysis to identify the variable cloud pressure and haze optical thickness patterns clearly. It turns out that some P_L-regions that do not fit well for a particular wavelength filter can be modelled better by other aerosol particles for that filter (see appendix E). In future research, the particle variation along the disk can be investigated further to allow for better matching of the observations. Note that in the analysis of the variable cloud pressure and haze optical thickness it becomes more difficult to draw conclusions due to over-fitting as more particles and therefore more variables are introduced. (see appendix D).

Also, the absorption at both the higher wavelengths due to methane and at the lower wavelengths (UV) can only be considered approximately with the current knowledge. The methane absorption coefficients from [Karkoschka, 1998] are derived from observations which contain inaccuracies and errors as well. About absorption in the UV-spectrum much more is unknown, the exact source has not yet been identified. The contribution of the gaseous layers, cloud layers and haze layer is yet unknown. Therefore, more research about the origin and effect of the UV-absorption at Jupiter is strongly recommended as it would significantly help in the development of more accurate results of the numerical model in the considered wavelength range.

Finally, the inclusion of aggregates of particles can be used in the numerical model to take into account the polar regions in the analysis, which is already done in among others [Karalidi et al., 2013] and [McLean et al., 2017].

All in all, a lot of improvement of various aspects with different nature is possible to characterise Jupiter's atmosphere more accurately in the upcoming decades.

Bibliography

Atreya, S. K., Mahaffy, P. R., and et al, H. B. N. (2003). Composition and origin of the atmosphere of jupiter - and implications for the extrasolar giant planets. *Planetary and Space Science*, 51:105–112.

Bagnulo, S., Landolfi, M., Landstreet, J. D., Landi Degl'Innocenti, E., Fossati, L., and Sterzik, M. (2009). Stellar Spectropolarimetry with Retarder Waveplate and Beam Splitter Devices. *Publications of the Astronomical Society of the Pacific*, 121(883):993.

Bessell, M. S. (1990). UBVRI passbands. *Publications of the Astronomical Society of the Pacific*, 102:1181–1199.

Bessell, M. S. (2005). Standard Photometric Systems. *Annual Review of Astronomy and Astrophysics*, 43:293–336.

de Haan, J. F., Bosma, P. B., and Hovenier, J. W. (1987). The adding method for multiple scattering calculations of polarized light. *Astronomy and Astrophysics*, 183(2):371–391.

de Rooij, W. A. and van der Stap, C. C. A. H. (1984). Expansion of Mie scattering matrices in generalized spherical functions. *Astronomy and Astrophysics*, 131(2):237–248.

Devogèle, M., Cellino, A., Bagnulo, S., Rivet, J. P., Bendjoya, P., Abe, L., Pernechele, C., Massone, G., Vernet, D., and Tanga, P. (2017). The Calern Asteroid Polarimetric Survey using the Torino polarimeter: assessment of instrument performances and first scientific results. *Monthly Notices of the Royal Astronomical Society*, 465(4):4335–4347.

Fernández Jiménez, M. (2018). *Characterization of the Amtosphere in Jupiter's Great Red Spot*. Master's thesis, Delft University of Technology.

Gehrels, T., Herman, B. M., and Owen, T. (1969). Wavelength dependence of polarization. atmosphere of jupiter. *Astronomical Journal*, 74:190.

Hansen, J. E. and Travis, L. D. (1974). Light scattering in planetary atmospheres. *Space Science Reviews*, 16(4):527–610.

Hovenier, J. W. and van der Mee, C. V. M. (1983). Fundamental relationships relevant to the transfer of polarized light in a scattering atmosphere. *Astronomy and Astrophysics*, 128(1):1–16.

Ingersoll, A. P., Dowling, T. E., and et al, P. J. G. (2004). Dynamics of jupiter's atmosphere. *Cambridge planetary science*, 1:105–128.

Karalidi, T., Stam, D. M., and Guirado, D. (2013). Flux and polarization signals of spatially inhomogeneous gaseous exoplanets. *Astronomy & Astrophysics*, 555:A127.

Karkoschka, E. (1994). Spectrophotometry of the Jovian Planets and Titan at 300- to 1000-nm Wavelength: The Methane Spectrum. *Icarus*, 111(1):174–192.

Karkoschka, E. (1998). Methane, Ammonia, and Temperature Measurements of the Jovian Planets and Titan from CCD-Spectrophotometry. *Icarus*, 133:134–146.

Karkoschka, E. and Tomasko, M. G. (2009). Methane Absorption Coefficients for the Jovian Planets and Titan. In *AAS/Division for Planetary Sciences Meeting Abstracts #41*, AAS/Division for Planetary Sciences Meeting Abstracts, page 10.11.

Kemp, J. C., Henson, G. D., Steiner, C. T., and Powell, E. R. (1987). The optical polarization of the sun measured at a sensitivity of parts in ten million. *Nature*, 326:270–273.

Kemp, J. C., Wolstencroft, R. D., and Swedlund, J. B. (1971). Circular polarization: Jupiter and other planets. *Nature*, 232:165–168.

Lindal, G. F. (1992). The Atmosphere of Neptune: an Analysis of Radio Occultation Data Acquired with Voyager 2. *Astronomical Journal*, 103:967.

Lissauer, J. J. and de Pater, I. (2013). *Fundamental Planetary Science*. Cambridge University Press.

Lyot, B. and Tessier, H. (1929). recherches sur la polarisation de la lumière des planètes et de quelques substances terrestres; 2me thèse: propositions données. *translated to English by NASA 1964*.

Martonchik, J. V., Orton, G. S., and Appleby, J. F. (1984). Optical properties of NH_3 ice from the far infrared to the near ultraviolet. *Applied Optics*, 23:541–547.

McLean, W., Stam, D. M., and et al, S. B. (2017). A polarimetric investigation of jupiter: disk-resolved polarimetry and spectropolarimetry. *Astronomy & Astrophysics*, 601(A142).

Militzer, B., Soubiran, F., Wahl, S. M., and Hubbard, W. (2016). Understanding Jupiter's interior. *Journal of Geophysical Research (Planets)*, 121(9):1552–1572.

Niemann, H. B., Atreya, S. K., and et al, P. R. M. (1996). The galileo probe mass spectrometer: Composition of jupiter's atmosphere. *Science (New Series)*, 272(5263):846–849.

Oliva, E. (1997). Wedged double wollaston, a device for single shot polarimetric measurements. *Astronomy & Astrophysics*, 123(3):589–592.

Opp, A. G. (1974). Pioneer 10 Mission: Summary of Scientific Results from the Encounter with Jupiter. *Science*, 183(4122):302–303.

Ortiz, V. L., Orton, G. S., and et al., A. F. (1998). Evolution and persistence of 5-μm hot spots at the galileo probe entry latitude. *Journal of Geophysical Research*, 103(10):23,051–23,069.

Peck, E. R. and Huang, S. (1977). Refractivity and dispersion of hydrogen in the visible and near infrared (E). *Journal of the Optical Society of America (1917-1983)*, 67:1550.

Romanescu, C., Marschall, J., Kim, D., Khatiwada, A., and Kalogerakis, K. S. (2010). Refractive index measurements of ammonia and hydrocarbon ices at 632.8 nm. *icarus*, 205(2):695–701.

Rossi, L., Berzosa-Molina, J., and Stam, D. M. (2018). PYMIEDAP: a Python-Fortran tool for computing fluxes and polarization signals of (exo)planets. *Astronomy & Astrophysics*, 616:A147.

Sromovsky, L. A. and Fry, P. M. (2002). Jupiter's Cloud Structure as Constrained by Galileo Probe and HST Observations. *icarus*, 157(2):373–400.

Stam, D. M. (2015). Lecture notes: Planetary exploration, practical exercises 2.

Stam, D. M., de Rooij, W. A., Cornet, G., and Hovenier, J. W. (2006). Integrating polarized light over a planetary disk applied to starlight reflected by extrasolar planets. *Astronomy and Astrophysics*, 452(2):669–683.

Stam, D. M., Hovenier, J. W., and Waters, L. B. F. M. (2004). Using polarimetry to detect and characterize jupiter-like extrasolar planets. *Astronomy & Astrophysics*, 428:663–672.

Stoll, C. P. (1980). *Polarimetry of Jupiter at Large Phase Angles.* PhD thesis, Arizona Univ., Tucson.

Stone, E. C. (1981). The Voyager mission through the Jupiter encounters. *Journal of Geophysical Research*, 86(A10):8123–8124.

Sun, Z. and Rikus, L. (1999). Improved application of exponential sum fitting transmissions to inhomogeneous atmosphere. *Journal of Geophysical Research*, 104(D6):6291–6303.

Sánchez-Lavega, A. (2011). *An Introduction to Planetary Atmospheres*. CRC Press, Taylor & Francis Group.

Taylor, F. W. (2001). The Jovian System from the Galileo Jupiter Orbiter. *Journal of the British Interplanetary Society*, 54:147–152.

Tomasko, M. G., Bézard, B., Doose, L., Engel, S., and Karkoschka, E. (2008). Measurements of methane absorption by the descent imager/spectral radiometer (DISR) during its descent through Titan's atmosphere. *Planetary and Space Science*, 56(5):624–647.

Tomasko, M. G., West, R. A., and Castillo, N. D. (1978). Photometry and polarimetry of jupiter at large phase angles. i - analysis of imaging data of a prominent belt and a zone from pioneer 10. *Icarus*, 33(197):558–592.

van de Hulst, H. C. (1957). *Light Scattering by Small Particles*. John Wiley & Sons Inc.

West, R. A. (1981). Sunlight absorption by aerosols in Jupiter's upper atmosphere. *Geophysical Research Letters*, 8(7):847–849.

West, R. A., Baines, K. H., and et al., F. (2004). *Jovian clouds and haze*, volume 1. Cambridge University Press.

West, R. A., Hord, C. W., Simmons, K. E., Coffeen, D. L., Sato, M., and Lane, A. L. (1981). Near-ultraviolet scattering properties of Jupiter. *Journal of Geophysical Research*, 86(A10):8783–8792.

West, R. A., Strobel, D. F., and Tomasko, M. G. (1986). Clouds, aerosols, and photochemistry in the jovian atmosphere. *Icarus*, 65:161–217.

Wong, M. H., Simon, A. A., and Orton, G. (2015). First results from the hubble opal program: Jupiter in 2015. *The Astrophysical Journal*, 812(1).

A

The Effect of the Accuracy Parameters

Besides the afore-mentioned input parameters ($r_{eff}, v_{eff}, nr, nr_i, pl, baer$) which are defnined for every aerosol layer, also accuracy parameters play a role. These parameters define the level of accuracy of the data generated by the numerical model (Fortran code). However, a higher accuracy comes with a price, namely, the computation time will increase as well. Therefore, an analysis regarding the accuracy and computation time has been made.

Table A.1: Accuracy parameters

Parameter	Fortran code part	Default value	New value	Time saving factor
# subintervals for r	Mie	250	-	-
# Gauss points in sub	Mie	200	-	-
# Gauss points (nmug)	Dap	50	20	6-10, 4-8[1]
# Pixels	Geos	100	50	4.0[2]
#λ-points (λp, all filters)	All	61	21	$61/21 \approx 2.9$

[1]: influence on computation time of Dap and Geos respectively [2]: influence on computation time of Geos

The main accuracy parameters are listed in table A.1 together with their default value (the initial value in the code). The Fortran code parts that mostly contribute to the computation time are the Dap and Geos part. The exact computational time per file (so per wavelength value) relates closely to the particle radius and variance beside the already mentioned parameters in table A.1. To give an indication, for $r_{c,eff}$=0.5 and $r_{h,eff}$=0.2 the computational times for the Mie, Dap and Geos part are about 1s, 15-30s and 30s respectively (for nmug=50 and npix=100), while for $r_{c,eff}$=1.0 and $r_{h,eff}$=0.5 the computational times for the Mie, Dap and Geos part are about 3s, 30-90s and 30-90s respectively (for nmug=50 and npix=100). These computational times are indicated per wavelength file. Consequently, the accuracy parameters in the Mie part are kept on the default value as it will not save much time.

The time saving factor is an indicator for the time that can be saved (for a specific part of the code: Mie, Dap or Geos) by using the 'new value' instead of the 'default value'. A time saving factor of X means that the data is generated X's times as fast compared to the nominal case. It has to be noted that this parameter only provides an indication for the new computation time as more parameters have influence, such as the particle size and variance (r_{eff}, v_{eff})

as well as the wavelength (generally, the higher the wavelength, the lower the computation time). The difference in computation time between the lowest (300nm) and highest (900nm) wavelength can differ from a few seconds up to a factor of 2 for both Dap and Geos part (again depending on r_{eff}, v_{eff}, nmug, npix, etc.).

It turns out that the main accuracy parameters are the number of Gauss points (nmug in the Dap code), the number of pixels and the number of wavelength points considering all filters. Note again that the number of Gauss points needed to maintain the accuracy within certain boundaries depends on other parameters (as r_{eff} and v_{eff}). In this appendix the aim is to find accuracy parameter values that bring the computation time significantly down for a relative small decrease in accuracy as later on the accuracy can be increased again for the generation of the final results.

The number of Gauss points (or Gaussian abscissae) is used in the doubling adding algorithm and defines the number of illumination (μ_0) and viewing geometry (μ) combinations used. The required number of Gauss points to achieve a certain accuracy depends strongly on the single scattering properties which in turn depend on the aerosol particle properties. The Fourier coefficients are determined for nmug+1 values of μ and μ_0 (so for $(nmug+1)^2$ combinations of μ and μ_0). In this way an increasing number of Gauss points results in more Fourier coefficients such that the viewing geometry is more accurately represented in the Fourier coefficient file. (based on [Rossi et al., 2018]) This parameter thus really brings the computation time down (see table A.1) but the effect on the accuracy is difficult to quantify and has to be analysed for the specific parameter values.

[Rossi et al., 2018] has investigated the effect of the number of Gaussian points (nmug) and found that for a model planet without aerosol layers a relative small number of Gaussian abscissae (nmug=20) already provides a very accurate result. This model planet has thus a purely gaseous atmosphere with $b_{sca}^{m} = 5.75$, $b_{sca}^{m} = 0.0$, a surface albedo (a_s) of 0.0 and a depolarisation factor (ρ) of 0.02 and the calculations are performed for a wavelength of 550nm [Rossi et al., 2018]. The result found in this analysis using the same parameter values is in conformance with this result from [Stam et al., 2006] and [Rossi et al., 2018] as can be seen in figure A.1. Note that the red and blue line of sub-figure A.1b show P_L for two calculation methods. When assuming that the visible disk is mirror-symmetric w.r.t. the reference plane, U becomes zero for the disk-integrated P_L [Stam et al., 2004]. The blue line is thus a simplification of the red line using this assumption and it can be seen that this assumption is justified as the curves coincide.

[Rossi et al., 2018] states that for a model planet with an aerosol layer containing large particles ($x_{eff} = 19.747, v_{eff} = 0.070$) with r_{eff} up to about $361\mu m$ more Gaussian points are required to get accurate results for the entire phase angle range, a value of nmug=50 is used in that analysis. It is tried to verify the results of this model but the particles are too large to build with the numerical model, the error message *'too many coefficients needed: .... Therefore I cannot do the expansion'* appears. It is possible to bring down the accuracy parameters of the number of sub-intervals for r or the number of Gauss points in these sub-intervals (which is different from nmug). However, it is questionable whether this will yield an accurate result as for larger particles the accuracy parameters have to be larger as well to assure a certain accuracy.

It has to be noted that in this analysis much smaller aerosol particles are used; for the cloud particles an effective radius of around 1.00 and $0.52\mu m$ are regarded. Note that the haze

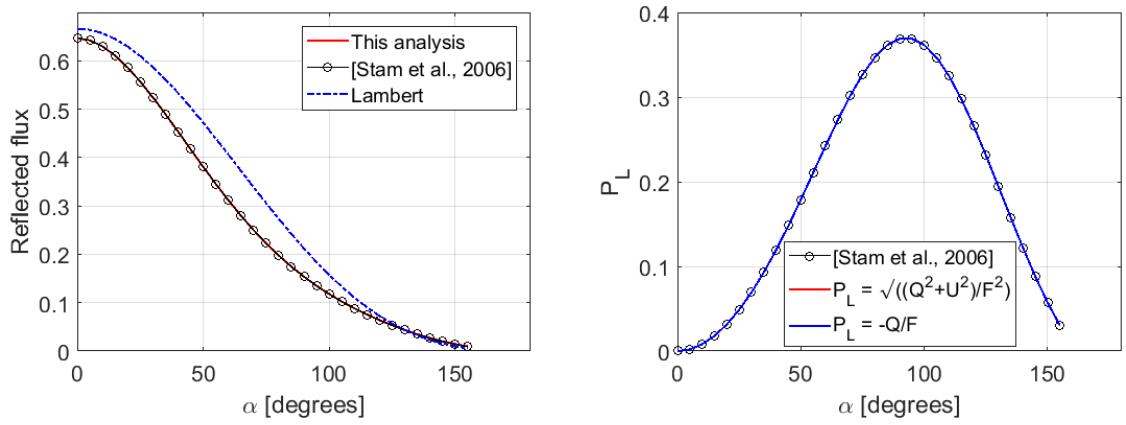

(a) (b)

Figure A.1: Disk-integrated reflected flux and P_L for model planet 1 of [Rossi et al., 2018]

particles are even smaller. It is possible that a smaller number of Gaussian points can be used in this analysis to still ensure a high accuracy.

Therefore, a similar procedure as described in [Rossi et al., 2018] is carried out but instead of the large particles ($x_{eff} = 19.747, v_{eff} = 0.070$) particles with the approximate size of this analysis are used. The particle properties and other parameters used for this nmug-analysis are stated in table A.2. The result of the effect of the number of Gaussian points on the disk-integrated reflected flux (F) and linear degree of polarisation (P_L) for the phase angle range from 0 to 180° for these parameter values is shown in figure A.2.

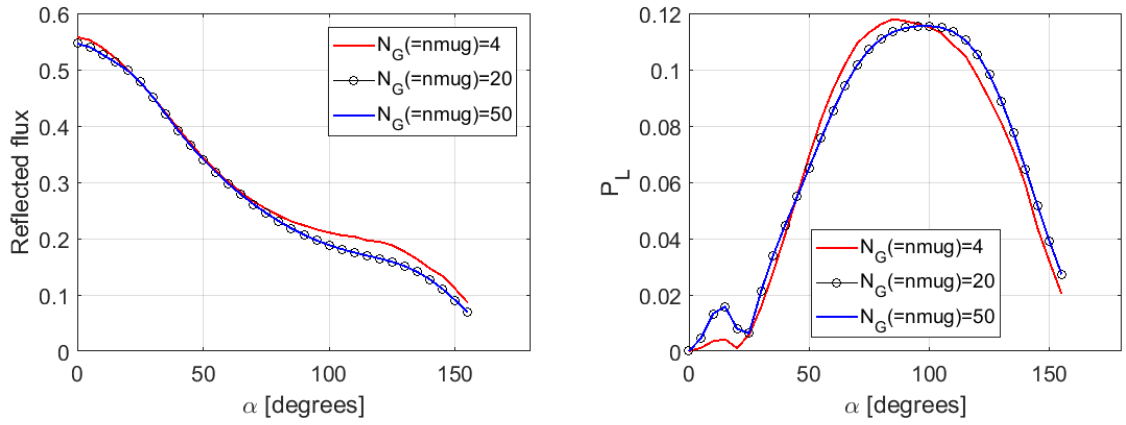

(a) (b)

Figure A.2: Disk-integrated reflected flux and P_L for a case similar to this analysis with a variable phase angle (λ=0.550μm)

From the figure it can be seen that a value for nmug of 20 already gives an accurate result as the difference with nmug=50 cannot be noted from the figure. The disk-integrated P_L has a maximum close to a phase angle of 90° while the phase angle of the observations is 10.73°. Consequently, the wavelength dependence of the disk-integrated reflected flux (F) and degree of linear polarisation (P_L) for a phase angle of 10.73° is investigated and shown in Figure A.3.

Again, it can be seen that a value for nmug of 20 already yields accurate results (the curves lie on top of each other).

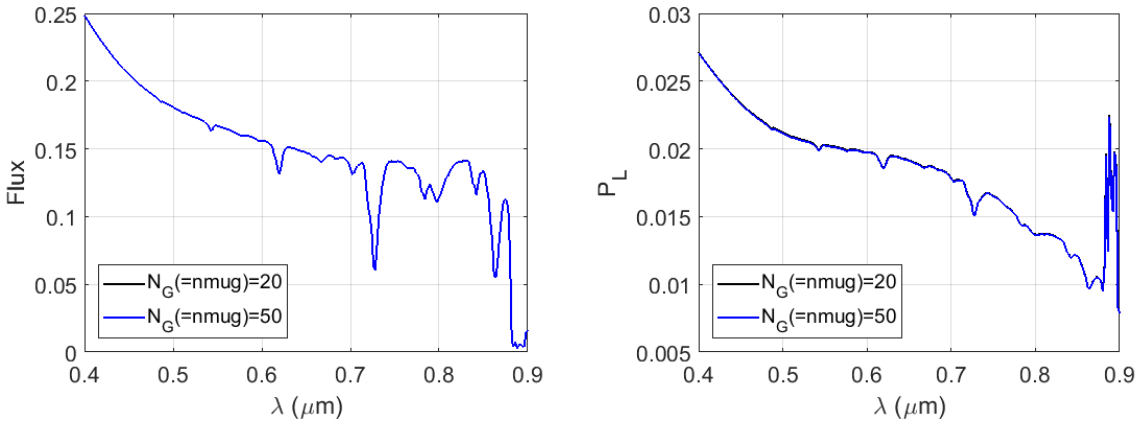

(a) (b)

Figure A.3: Disk-integrated reflected flux and P_L for a case similar to this analysis with a variable wavelength (α=10.73°)

Besides the comparison with the analysis of [Rossi et al., 2018], also other P_L figures are presented in this appendix to additionally show the effect on disk-resolved data on top of the disk-integrated data.

Note that in the figures showing the phase angle range from 0 to 180 °, the numerical model only generates data up to a phase angle of 155 °.

The next accuracy parameter is the number of pixels which is relative easy to grab, the more pixels, the higher the accuracy (until reaching the observational data size). The observational data is given as a matrix of 151x151 pixels such that the closer the number of pixels approximates this value, the lower the interpolation error will be. Note that the numerical model data for npix<151 is interpolated to the observational data size of 151x151 pixels to be able to compare the pixel locations one to one. As the data is stored in a square array of pixels, the computation time scales directly to the total number of pixels. Note that npix defines the number of pixels along the planet's equator, so in one direction only. The total matrix containing the data is a npix by npix matrix.

The number of wavelength points directly influences all parts of the numerical model (Mie, Dap, Geos) as the data is generated per wavelength. The wavelength filters used have a total of 61 unique wavelength points for all filters (some wavelength points exist in more than one filter) [Bessell, 2005]. However, a selection of less wavelength points can be made to resemble the filter shapes.

Table A.1 shows that the accuracy parameters can bring down the computation time significantly. However, the accuracy of the polarisation results are more important as finally high accurate results are required to make an as good as possible comparison with the observations. The polarisation results for the Red wavelength filter are shown in Figure A.4 for the four described cases. The R-filter is chosen as methane absorption plays a role in this filter, consequently, the effect on the accuracy by decreasing the number of wavelength points is expected

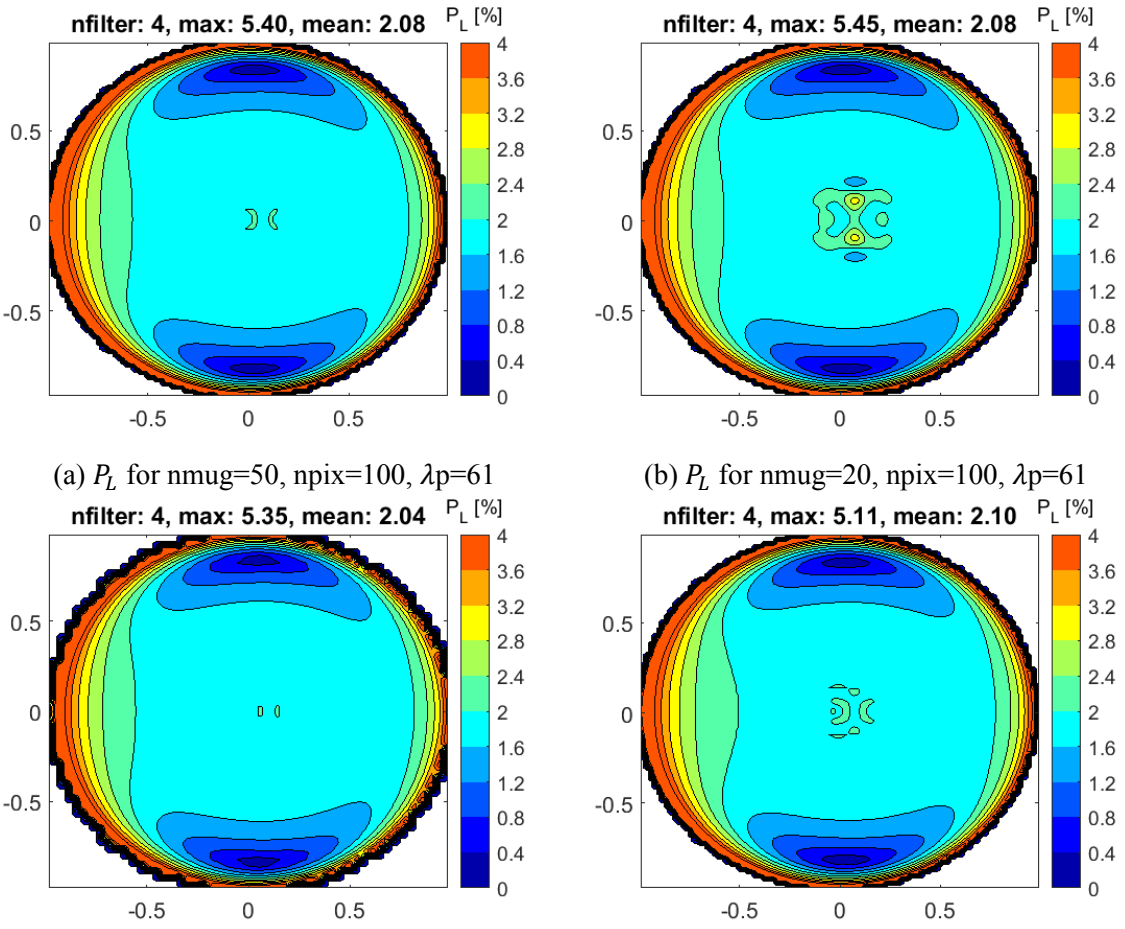

(a) P_L for nmug=50, npix=100, λp=61

(b) P_L for nmug=20, npix=100, λp=61

(c) P_L for nmug=50, npix=50, λp=61

(d) P_L for nmug=50, npix=100, λp=21

Figure A.4: P_L in the R-filter for different accuracy parameters combinations
Note: subfigure A.4a denotes the nominal case

to be most prominent in this filter. The polarisation results of the different cases are similar at first sight, but the exact differences with the nominal case provide additional information as is visualised in Figure A.5. Note that the P_L difference (ΔP_L) is given as an absolute percentage.

The comparison between the accuracy and computation time for the three accuracy parameters (nmug, npix and λp) with the nominal case is done for the constant parameters shown in table A.2. It is important to keep the rest of the parameters the same for a fair comparison. On the other hand, note that both the computation time and accuracy depend on these parameters. Therefore, parameters based on [McLean et al., 2017] are used for this purpose as this research regards a similar analysis as is presented in [McLean et al., 2017].

Figure A.5 shows the P_L difference between the nominal case and the case with one accuracy parameter adapted. For the sub-figures related to the parameters nmug and npix two different scales (0-0.1% and 0-0.5%) are used for clarification.

Sub-figures A.5a and A.5b show that the number of Gauss points (nmug) mainly influences the central region of Jupiter's visible disk where for the given parameters (Table A.2) ΔP_L is in the range of 0.1-0.9%. On the other hand, most of the disk has a ΔP_L lower than 0.01% and the mean value is only 0.02%. Note that the P_L values of the numerical model are shown in figure A.4, to place the P_L-difference in perspective for the shown accuracy parameters. Additionally,

Table A.2: Accuracy parameter comparison values

Parameter	Cloud	Haze
$r_{eff}(\mu m)$	0.50	0.20
v_{eff}	0.05	0.01
nr	1.42+0.015i	1.50+0.001i
baer	50	0.2
p (bar)	1.334-1.000	0.178-0.100

Note: a phase angle of 10.73° is used.

this accuracy parameter brings the computation time down by the largest factor (about 5 or 6 times). Again, note that the accuracy depends on other parameters as r_{eff}, v_{eff} and the other accuracy parameters as well.

The effect of the number of pixels (npix) on ΔP_L is given in Sub-figures A.5c and A.5d. Again, the numerical model data is interpolated from the indicated size (npix by npix) to the observational data size of 151x151 pixels. It can be argued that it is least worthwhile to change the number of pixels as ΔP_L is relatively large and the computation time can only be brought down for the Geos part (Fortran code). The maximum (5.26) and mean (0.21) are significantly large as well.

Finally, ΔP_L due to the number of wavelength points used (λp) is visualised in Sub-figure A.5e (it is shown for one scale only as it visualises the data well). The number of wavelength points brings the entire computation time significantly down (with a factor of about 2.9) while the accuracy penalty is limited. The maximum difference is 0.42% and occurs at the edge (probably as the P_L values are highest there, see figure A.4) , while the mean difference is relative low and the difference more or less constant along the disk.

All three cases show a relative high ΔP_L at the edges. This relates to the fact that the P_L values are largest at the edge as well. Furthermore, the assumption of plane parallel layers of the numerical model is not valid anymore at the edges. Also, the alignment error (see chapter 3) of the observations is largest at the edges.

So, first the accuracy parameter values limiting the computation time and preserving a reasonable high accuracy (low ΔP_L) are used to narrow down the parameter search space. In a later stadium, when a small parameter search space remains, the accuracy can be increased to find the best numerical model for a certain region.

As mentioned previously, the effect of the number of Gauss points (nmug) on the accuracy relates to (among others) the parameters r_{eff} and v_{eff}. Figure A.6, which uses a larger cloud particle with $r_{eff} = 1\mu m$, shows that the impact on the accuracy becomes larger for larger particles. As the computation time increases significantly with increasing particle size (for constant parameter values except $r_{c,eff} = 0.5\mu m$ and $r_{c,eff} = 1.0\mu m$ the computation time of the DAP part is about 15-45s and 30-80s respectively), it is chosen not to generate figures of the effect on even larger particles. Generally, when larger particles are used more Gauss points are required to maintain the accuracy within a certain required level. Moreover, when a too low number of Gauss points for the particular particle properties is used, the doubling adding code gives the warning: *'repeated reflections did not converge after X steps'*. This indicates that the variation in total and polarised fluxes with single scattering angle θ cannot be captured by the number of Gaussian integration points (based on [Rossi et al., 2018]). It can be shown

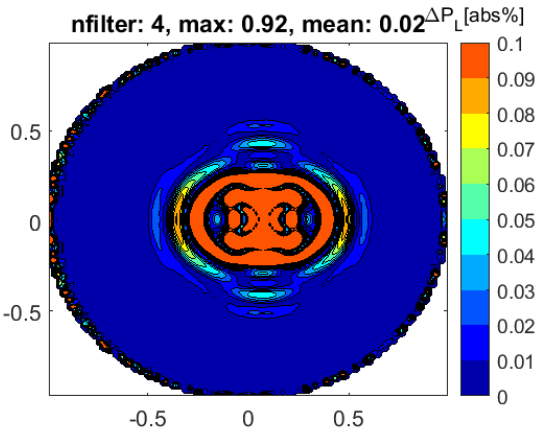

(a) ΔP_L for nmug = 20 and 50

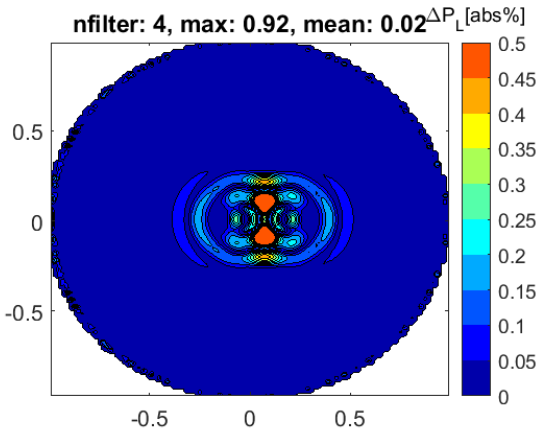

(b) ΔP_L for nmug = 20 and 50

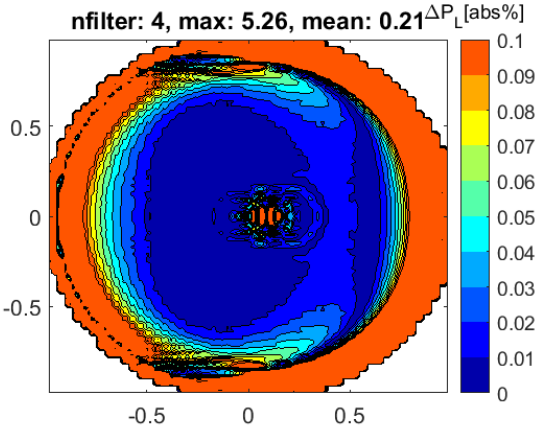

(c) ΔP_L for npix = 50 and 100

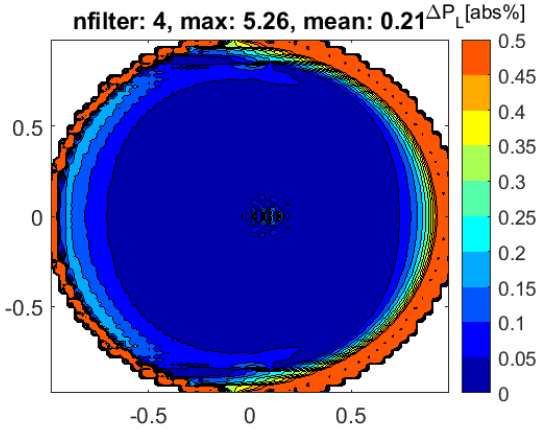

(d) ΔP_L for npix = 50 and 100

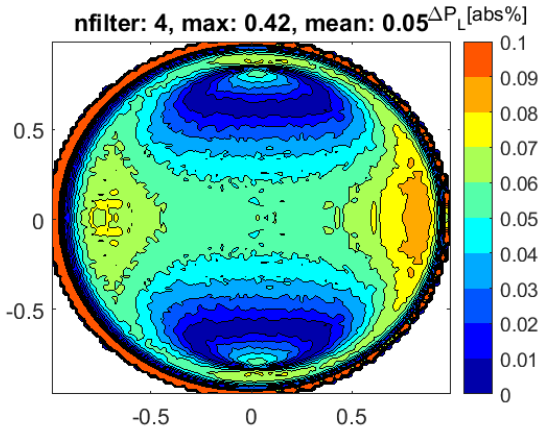

(e) ΔP_L for λp = 21 and 61

Figure A.5: ΔP_L in the R-filter for different accuracy parameters combinations

that with nmug=20 particles up to $r_{eff} = 2.5\mu m$ can be modelled (with the used cloud optical thickness of 25, which is sufficient for this research).

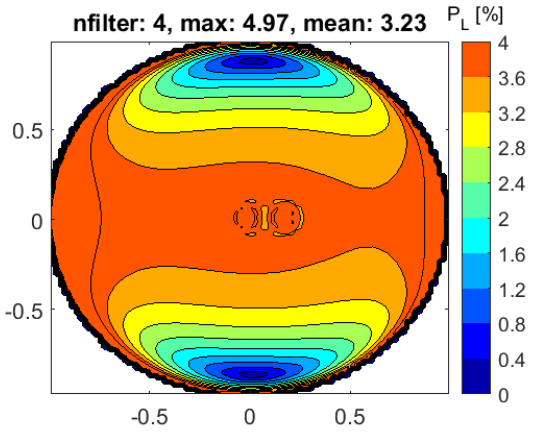

(a) P_L for nmug=50, npix=100, λp=61

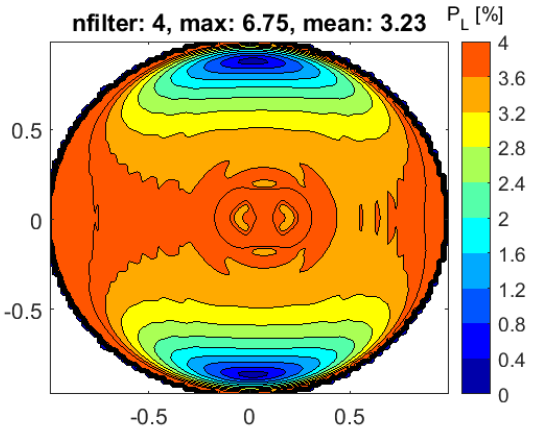

(b) P_L for nmug=20, npix=100, λp=61

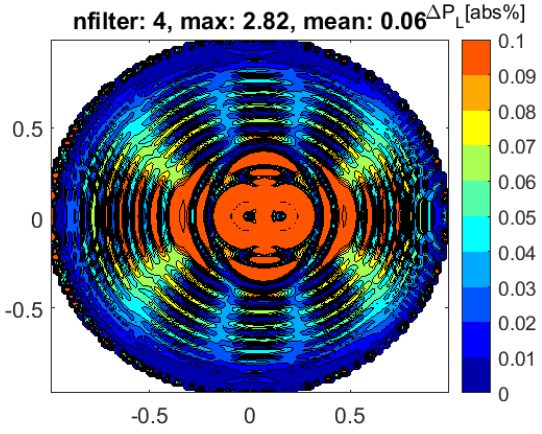

(c) ΔP_L for nmug=20 and 50

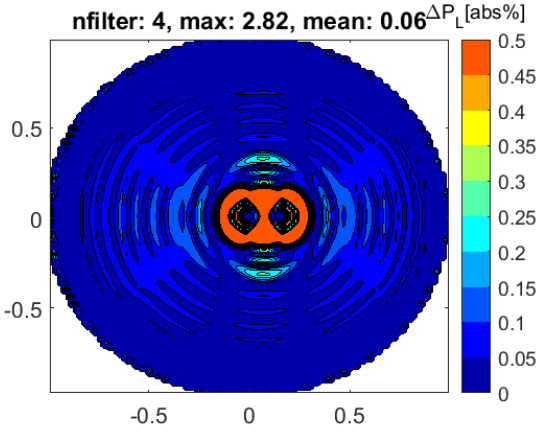

(d) ΔP_L for nmug=20 and 50

Figure A.6: The effect of nmug on P_L and ΔP_L in the R-filter for $r_{eff} = 1\mu m$

B

Sensitivity to the Atmospheric Input Parameters

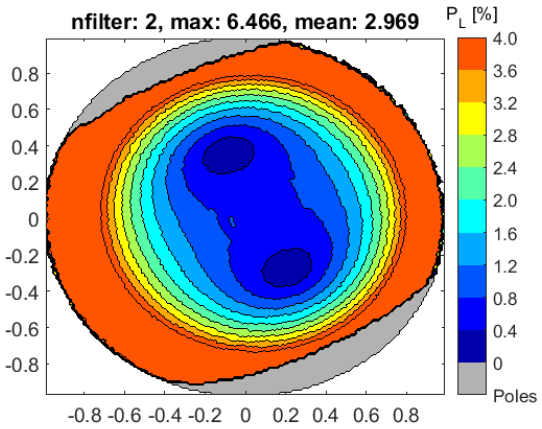

(a) P_L for a cloud pressure of 1.334-2.371bar

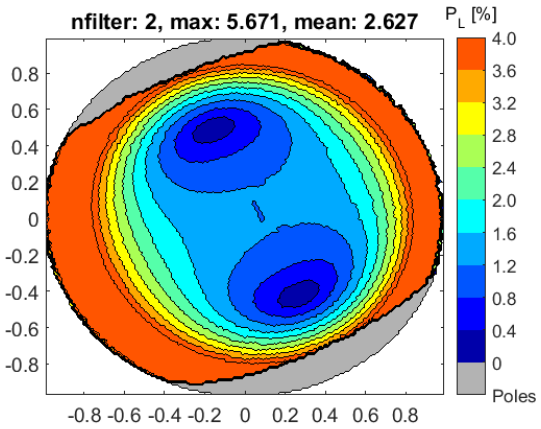

(b) P_L for a cloud pressure of 1.000-1.778bar

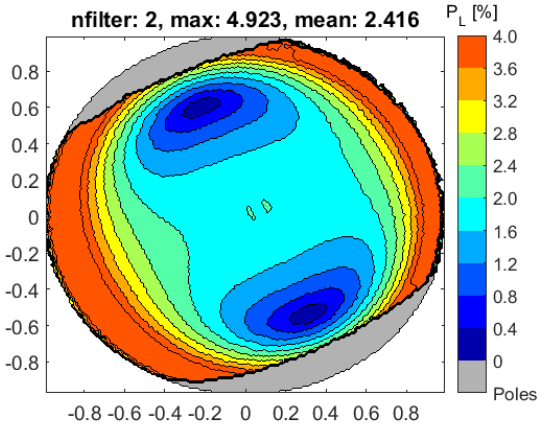

(c) P_L for a cloud pressure of 0.7499-1.334bar

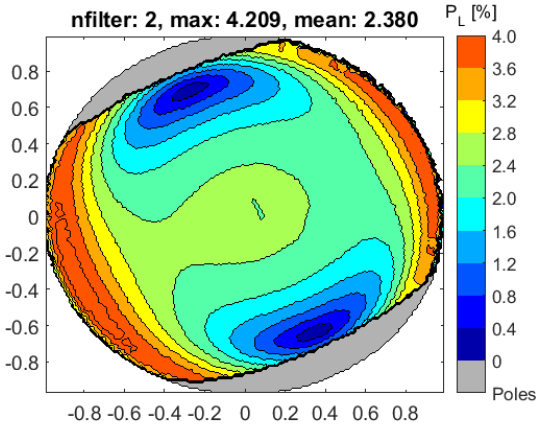

(d) P_L for a cloud pressure of 0.5623-1.000bar

Figure B.1: P_L for different cloud pressures

This appendix shows the sensitivity of the degree of linear polarisation to the atmospheric input parameters. The regarded input parameters are the pressure (layer) and the optical thick-

ness which are evaluated for both the cloud and the haze. To limit the amount of information, the comparison is done for the B-filter only, as this filter is most sensitive to P_L. The analysis regards every time four values for a specific input parameter while the rest of the input parameters is kept constant according to the values of table B.1.

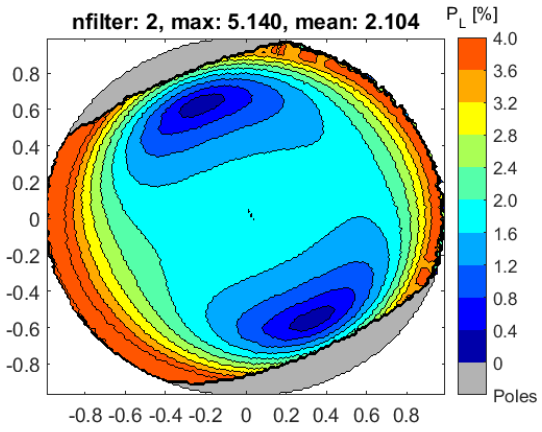

(a) P_L for a haze pressure of 0.2371-0.3612bar

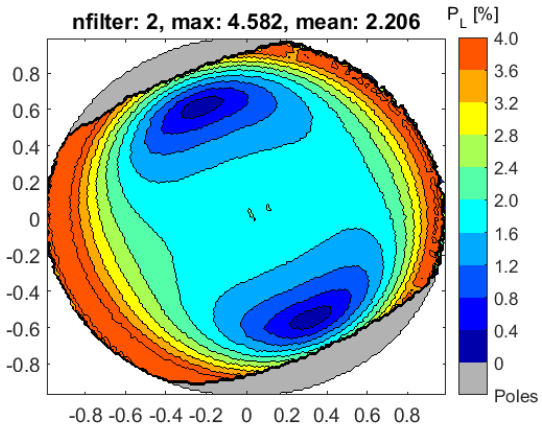

(b) P_L for a haze pressure of 0.1778-0.2371bar

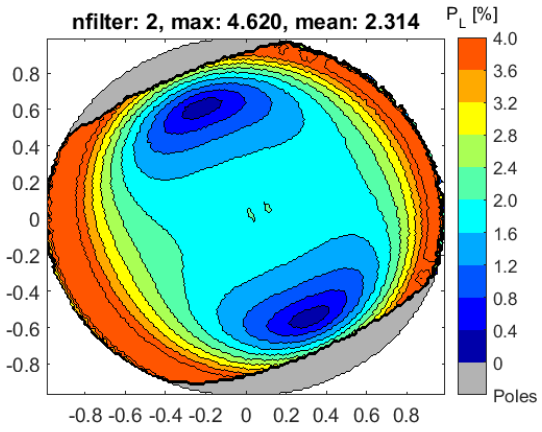

(c) P_L for a haze pressure of 0.1334-0.1778bar

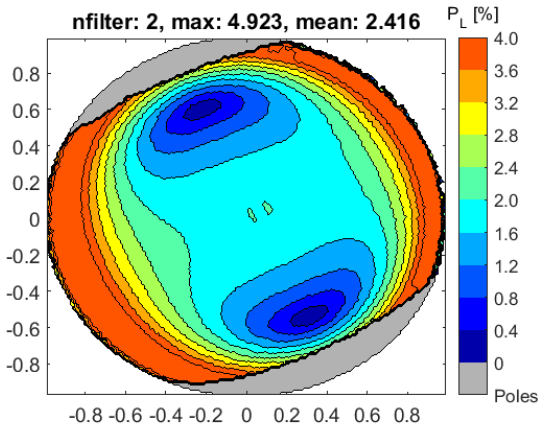

(d) P_L for a haze pressure of 0.1000-0.1334bar

Figure B.2: P_L for different haze pressures

First, the P_L-sensitivity to the pressure of the cloud and haze are evaluated in figure B.1 and B.2. It can be seen that P_L is significantly more sensitive to the cloud pressure than to the haze pressure. Therefore, the cloud pressure is regarded as a variable in this analysis. P_L is less sensitive to the haze pressure, especially at the mid-longitudes. On the other hand, it can be seen that towards the left and right edges the haze pressure has different values for different input values.

Secondly, the optical thickness of the cloud and haze are compared using figure B.3 and B.4 respectively. The optical thickness of the cloud shows only a marginal effect on P_L as an optically thick cloud layer is regarded in this analysis. Above a certain optical thickness practically no light will penetrate the cloud layer such that the result will remain approximately the same. The degree of linear polarisation is sensitive to the optical thickness of the haze layer as significant lower values are used in accordance with previous research. It can be seen that a

Table B.1: The constant values of the atmospheric input parameters

Parameter	Cloud	Haze
r_{eff}	$0.50\mu m$	$0.20\mu m$
v_{eff}	0.05	0.01
nr	1.42+0.015i	1.50+0.001i
plc	6-7 (0.7499-1.334bar)	14 (0.1000-0.1334bar)
baer	25	0.2

higher haze optical thickness generally decreases P_L as the haze has a depolarising effect. Due to the high sensitivity to P_L, the haze optical thickness is also used as a variable in the analysis.

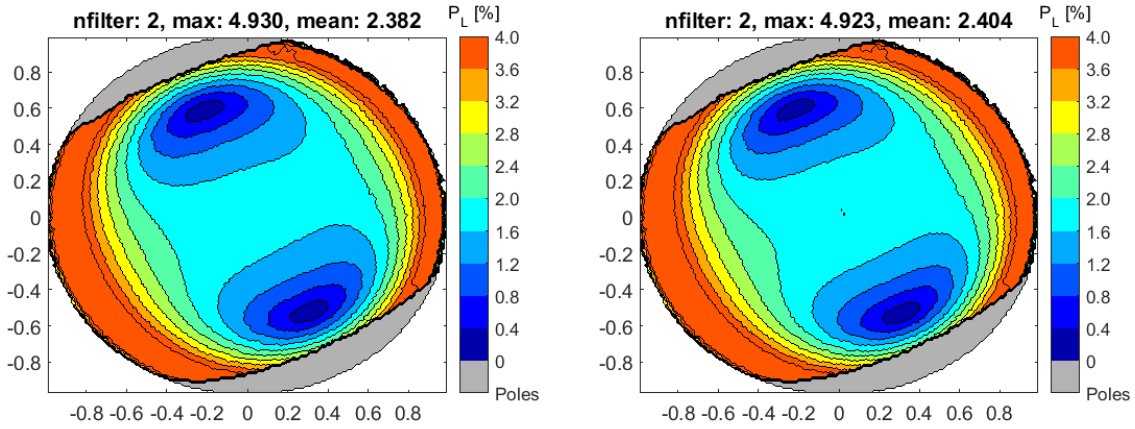

(a) P_L for an optical thickness of the cloud of 5.0 (b) P_L for an optical thickness of the cloud of 10.0

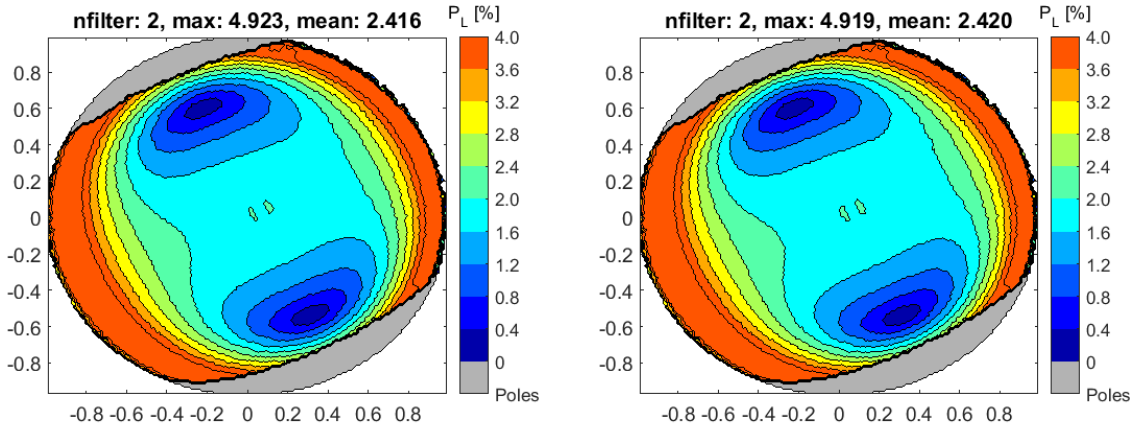

(c) P_L for an optical thickness of the cloud of 25.0 (d) P_L for an optical thickness of the cloud of 50.0

Figure B.3: P_L for different cloud optical thickness

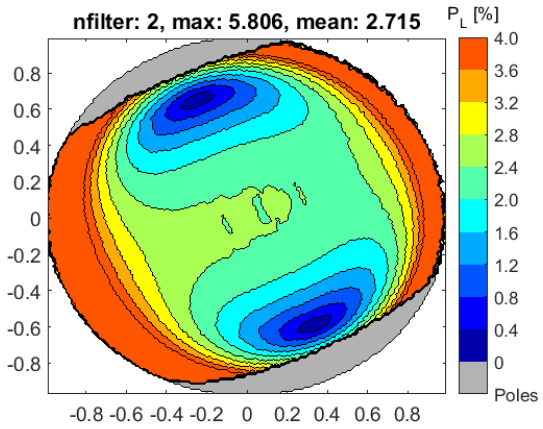

(a) P_L for an optical thickness of the haze of 0.1

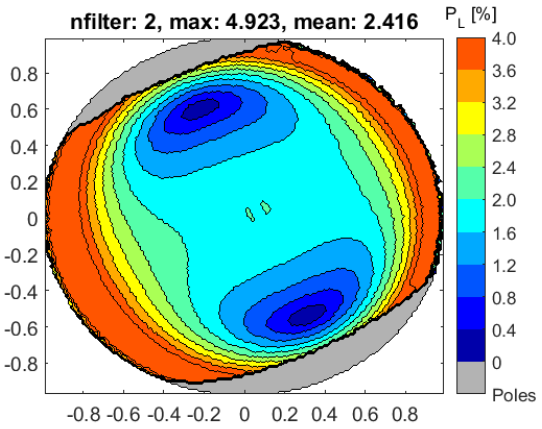

(b) P_L for an optical thickness of the haze of 0.2

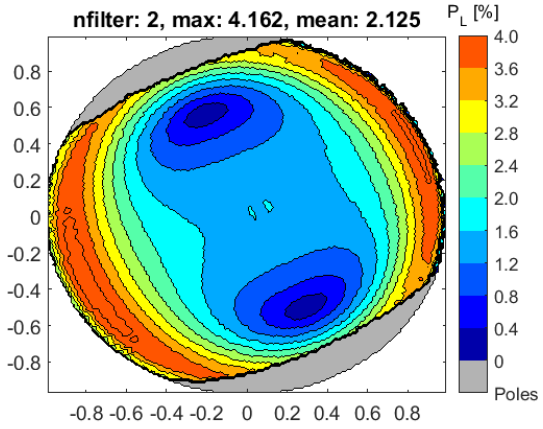

(c) P_L for an optical thickness of the haze of 0.3

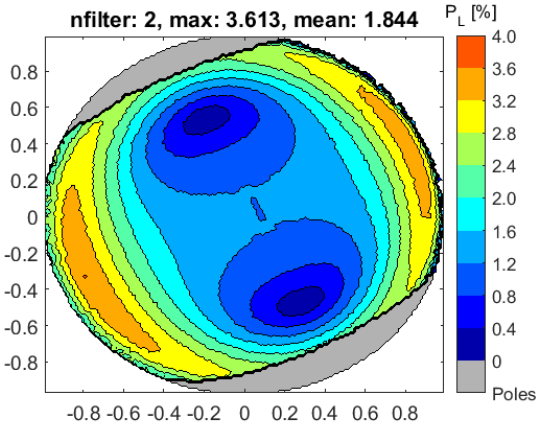

(d) P_L for an optical thickness of the haze of 0.4

Figure B.4: P_L for different haze optical thickness

C

P_L Response of the Different Situations

This appendix shows some test cases consisting of degree of linear polarisation plots for Jupiter's visible disk for the different situations, wavelength filters and variable atmospheric parameters. In this way, it is possible to clearly see the P_L response to the particle properties, cloud pressure and haze optical thickness. To limit the amount of information, the sensitivity of P_L for the different wavelength filters to the cloud pressure and haze optical thickness are shown by a low pressure (3.16-1.78bar) and high pressure cloud (0.56-0.36bar) and a low (0.1) and higher (0.5) haze optical thickness.

This analysis is carried out before the results presented in chapter 6 were generated and therefore the number of Gaussian points (nmug) is set to 20 to get approximate results. This can be seen in the Figures by the patterns of deviating P_L that appear in the centre region of the planet. Still, the results give a good indication of the effect of plc and baerh on the P_L-response. The more detailed results of chapter 6 are generated using nmug=50.

C.1. Situation 1

The particle properties of situation 1 and their corresponding P_L response is shown in Figures C.1, C.2, C.3 and C.4.

From the V- and R-filter it can be seen that the P_L response to these particle properties is more sensitive to the haze optical thickness (baerh) than to the cloud pressure (plc). The U- and B-filter show a more nuanced sensitivity as they show significantly different P_L responses for both changes in plc and baerh. Note that the observations described in this section only hold for the particle properties of situation 1. For different particle properties the P_L response and consequently the sensitivity to plc and baerh can differ significantly.

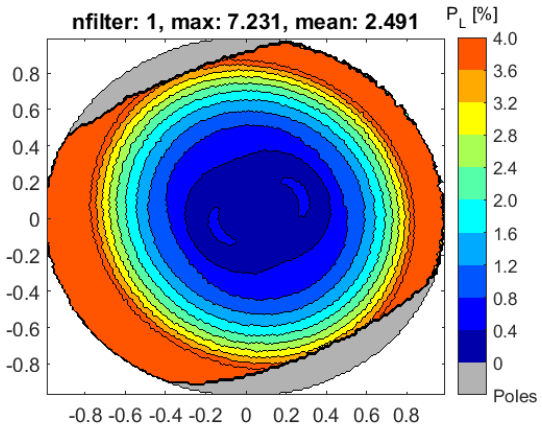

(a) P_L for baerh=0.1, plc=3.16-1.78bar

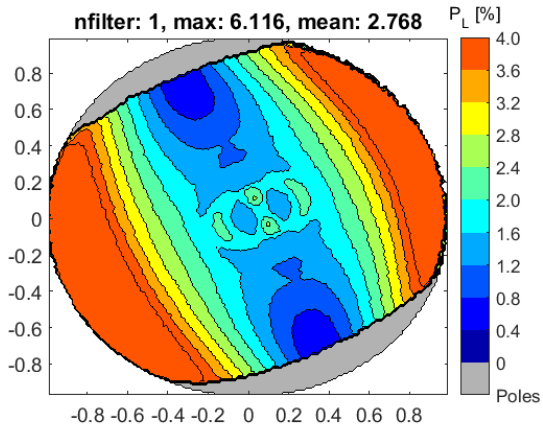

(b) P_L for baerh=0.5, plc=3.16-1.78bar

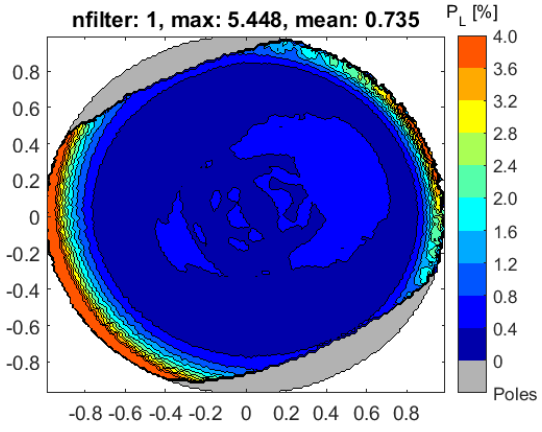

(c) P_L for baerh=0.1, plc=0.56-0.36bar

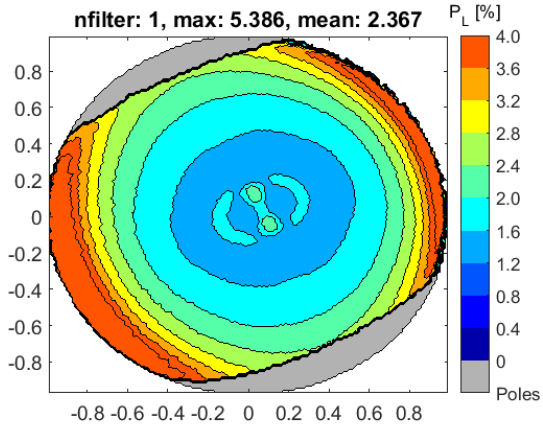

(d) P_L for baerh=0.5, plc=0.56-0.36bar

Figure C.1: Situation 1: P_L in the U-filter

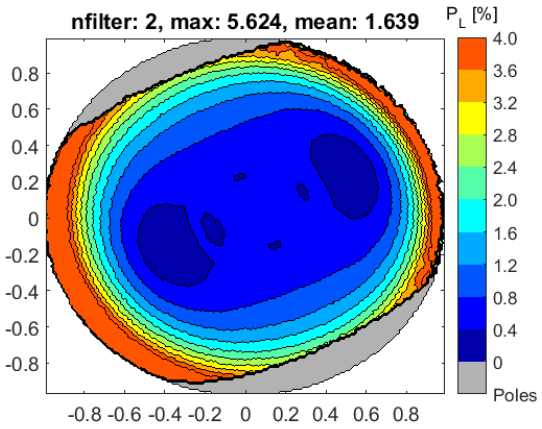

(a) P_L for baerh=0.1, plc=3.16-1.78bar

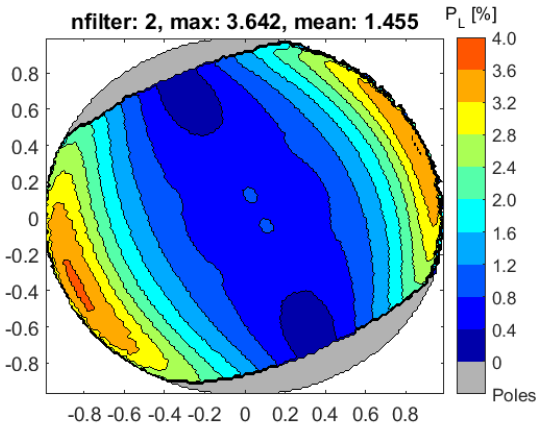

(b) P_L for baerh=0.5, plc=3.16-1.78bar

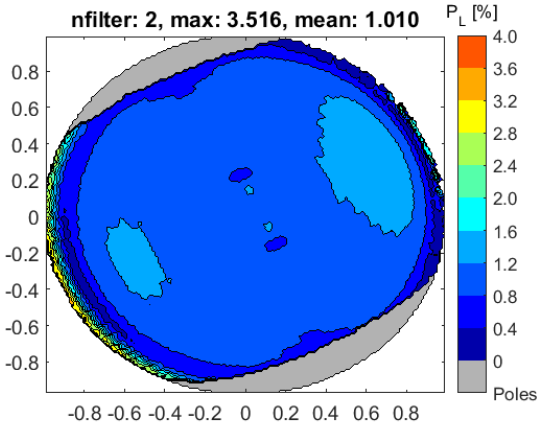

(c) P_L for baerh=0.1, plc=0.56-0.36bar

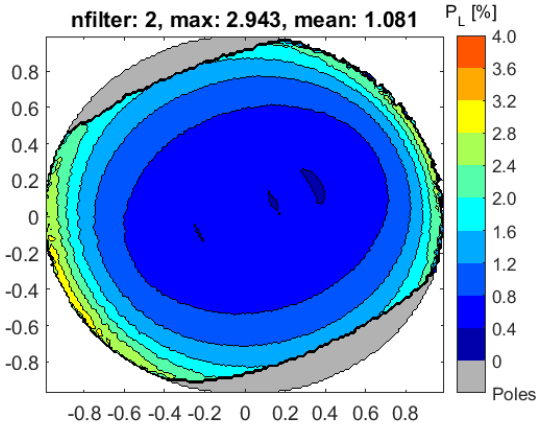

(d) P_L for baerh=0.5, plc=0.56-0.36bar

Figure C.2: Situation 1: P_L in the B-filter

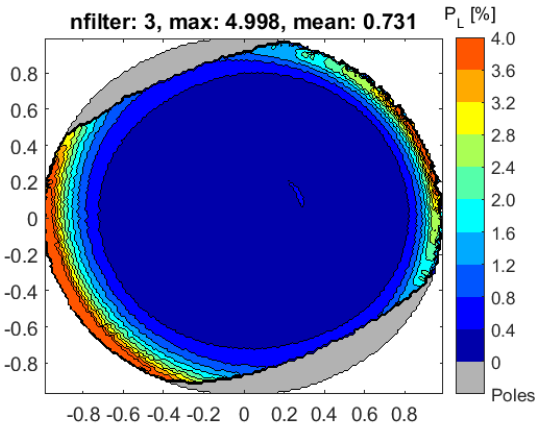

(a) P_L for baerh=0.1, plc=3.16-1.78bar

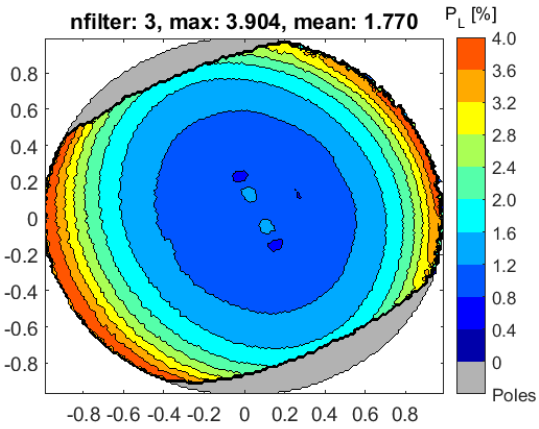

(b) P_L for baerh=0.5, plc=3.16-1.78bar

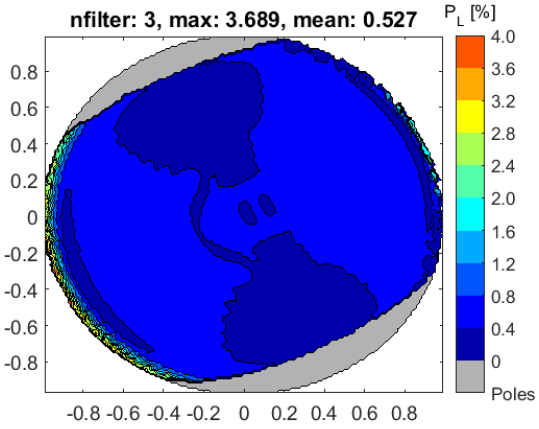

(c) P_L for baerh=0.1, plc=0.56-0.36bar

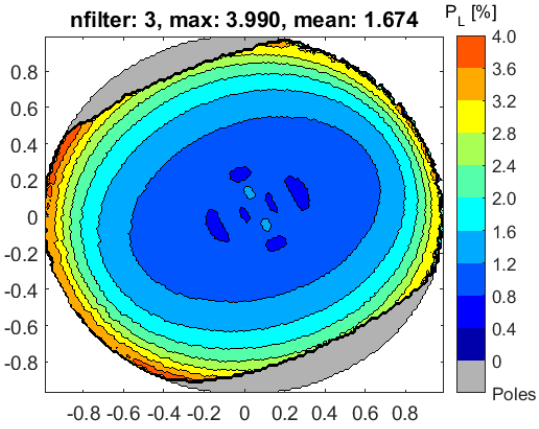

(d) P_L for baerh=0.5, plc=0.56-0.36bar

Figure C.3: Situation 1: P_L in the V-filter

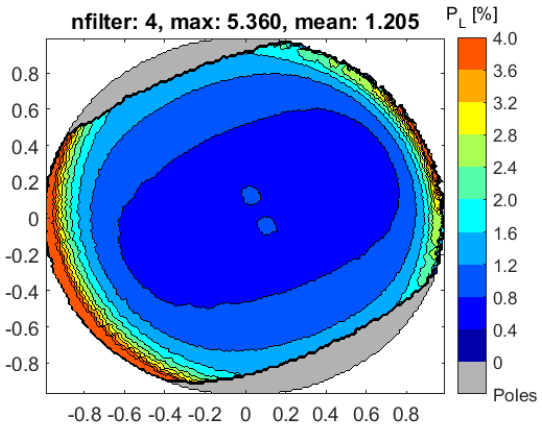

(a) P_L for baerh=0.1, plc=3.16-1.78bar

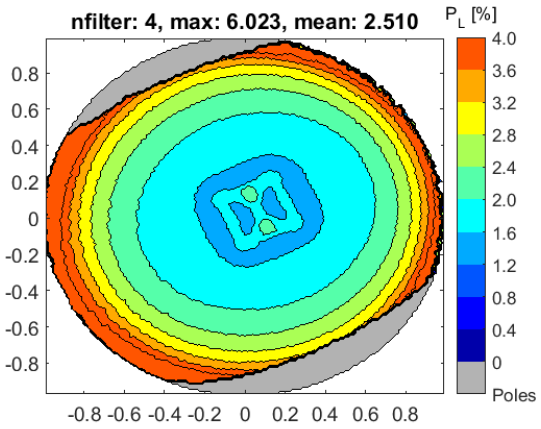

(b) P_L for baerh=0.5, plc=3.16-1.78bar

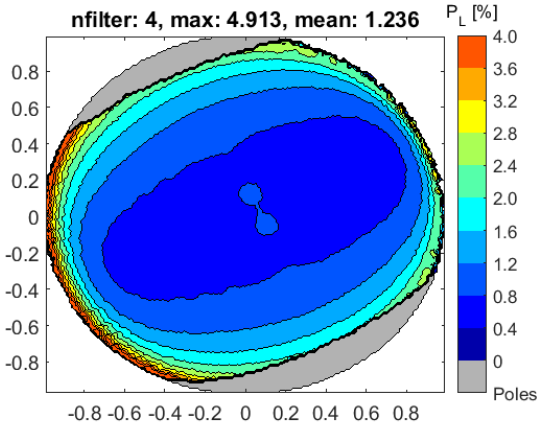

(c) P_L for baerh=0.1, plc=0.56-0.36bar

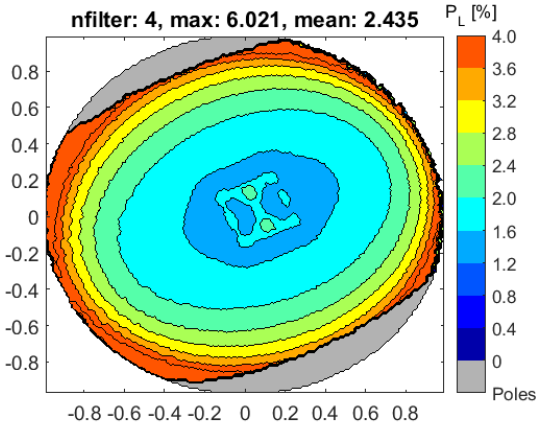

(d) P_L for baerh=0.5, plc=0.56-0.36bar

Figure C.4: Situation 1: P_L in the R-filter

C.2. Situation 2

The particle properties of situation 2 and their corresponding P_L response is shown in Figures C.5, C.6, C.7 and C.8.

The U-filter shows that the P_L response is more sensitive to the cloud pressure (plc) than to the haze optical thickness (baerh). The B-filter is sensitive to plc too, but the higher altitude clouds (0.56-0.36bar) appear to be significantly sensitive to baerh as well. The P_L response of the R- and V-filter is similar to the B-filter; it is sensitive to plc and the higher altitude clouds are sensitive to baerh too.

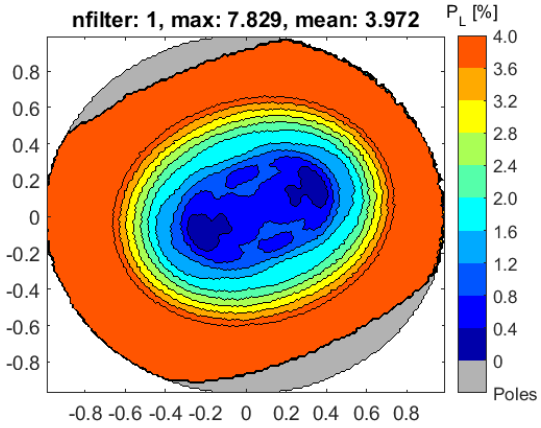

(a) P_L for baerh=0.1, plc=3.16-1.78bar

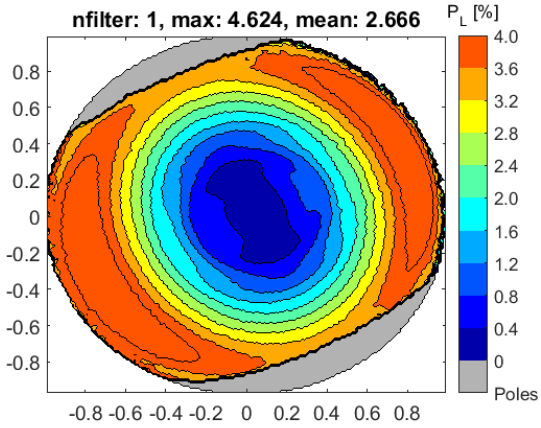

(b) P_L for baerh=0.5, plc=3.16-1.78bar

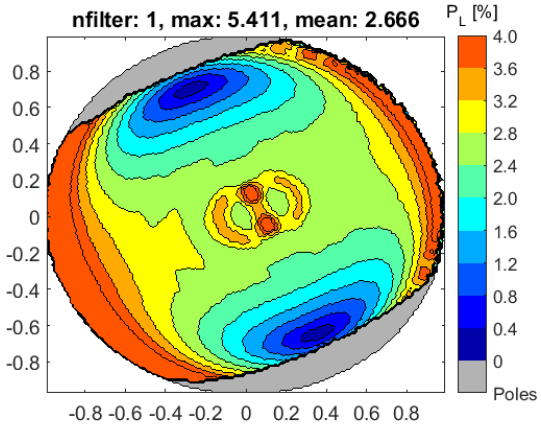

(c) P_L for baerh=0.1, plc=0.56-0.36bar

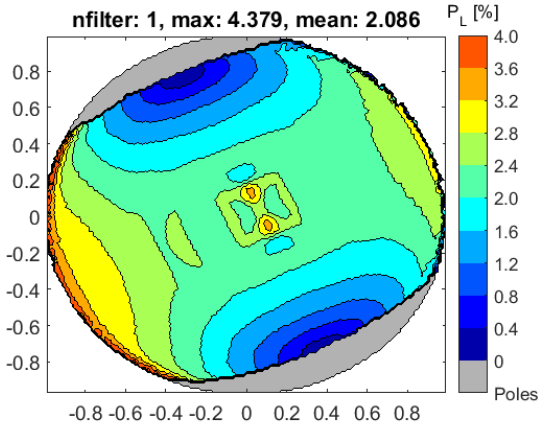

(d) P_L for baerh=0.5, plc=0.56-0.36bar

Figure C.5: Situation 2: P_L in the U-filter

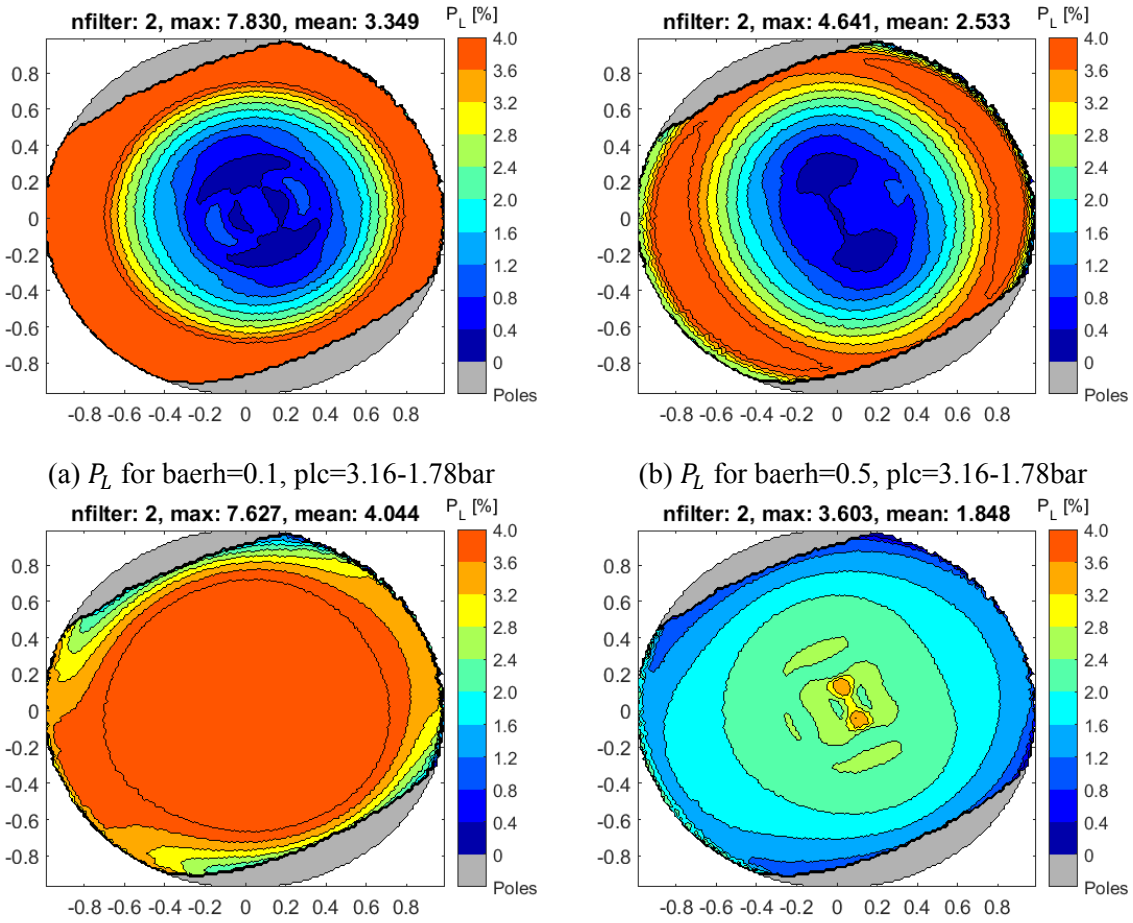

(a) P_L for baerh=0.1, plc=3.16-1.78bar

(b) P_L for baerh=0.5, plc=3.16-1.78bar

(c) P_L for baerh=0.1, plc=0.56-0.36bar

(d) P_L for baerh=0.5, plc=0.56-0.36bar

Figure C.6: Situation 2: P_L in the B-filter

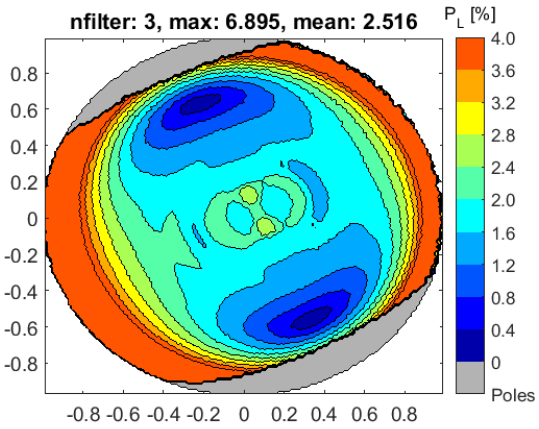

(a) P_L for baerh=0.1, plc=3.16-1.78bar

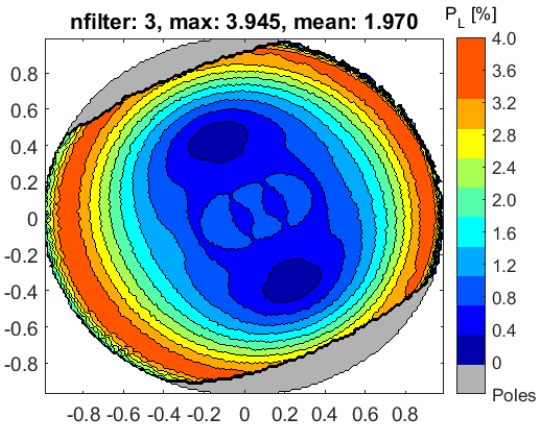

(b) P_L for baerh=0.5, plc=3.16-1.78bar

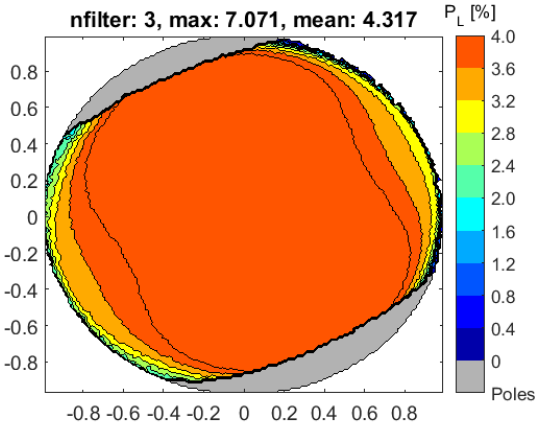

(c) P_L for baerh=0.1, plc=0.56-0.36bar

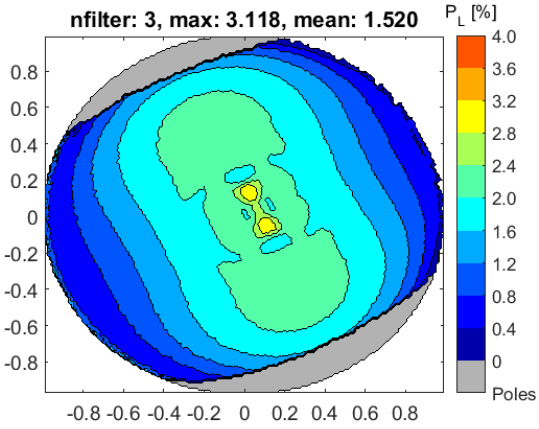

(d) P_L for baerh=0.5, plc=0.56-0.36bar

Figure C.7: Situation 2: P_L in the V-filter

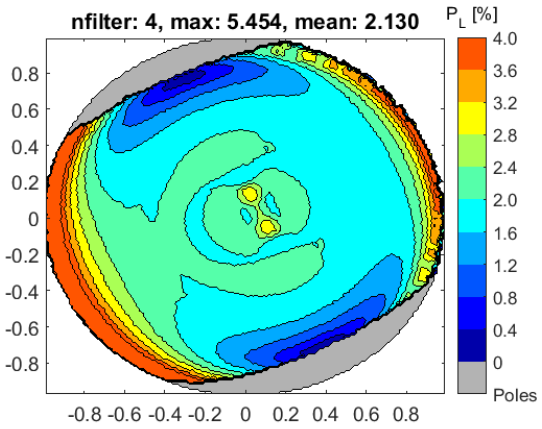

(a) P_L for baerh=0.1, plc=3.16-1.78bar

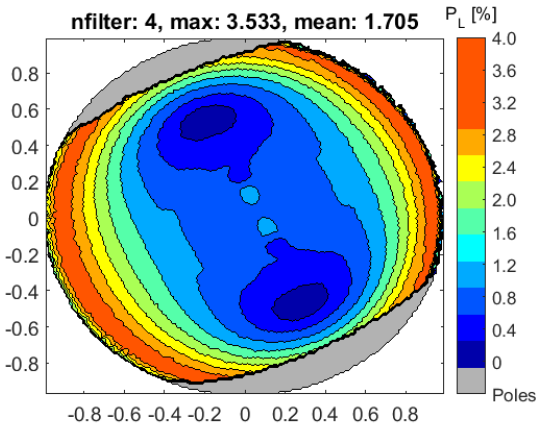

(b) P_L for baerh=0.5, plc=3.16-1.78bar

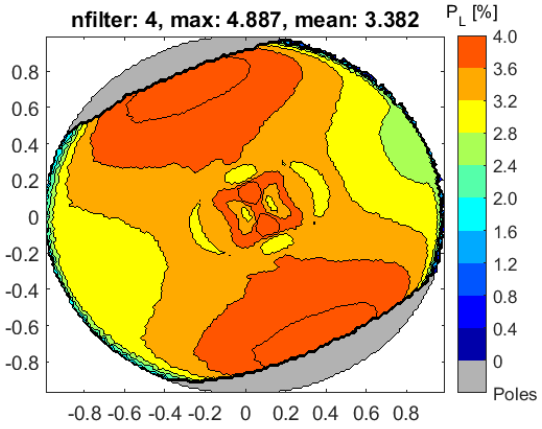

(c) P_L for baerh=0.1, plc=0.56-0.36bar

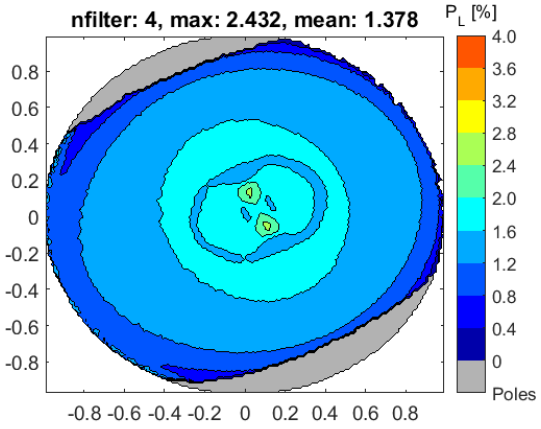

(d) P_L for baerh=0.5, plc=0.56-0.36bar

Figure C.8: Situation 2: P_L in the R-filter

C.3. Situation 3

The particle properties of situation 3 and their corresponding P_L response is shown in Figures C.9, C.10, C.11 and C.12.

The particle properties of situation 3 show a different P_L response compared to situation 2, although the only parameter that has a different value is the imaginary part of the refractive index. The U-filter is almost insensitive to baerh independent of the cloud pressure. The sensitivity to the cloud pressure is limited and is mainly present in the centre region. The B-filter is sensitive to the cloud pressure for both optically thin and thick haze, while the sensitivity of the haze optical thickness itself is small. The V-filter is sensitive to plc as well while the sensitivity to baerh is smaller. The R-filter does not seem to be sensitive to plc except for the outer edges and the sensitivity to baerh is marginal as well.

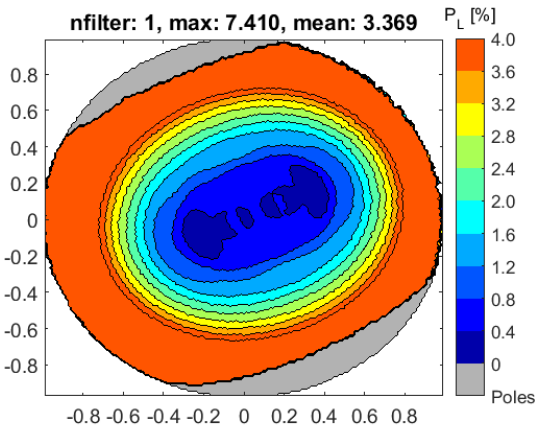

(a) P_L for baerh=0.1, plc=3.16-1.78bar

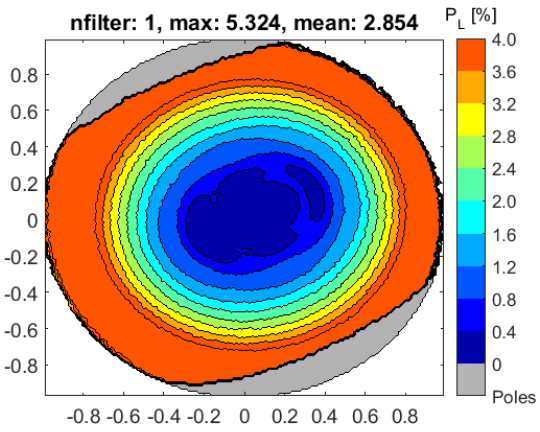

(b) P_L for baerh=0.5, plc=3.16-1.78bar

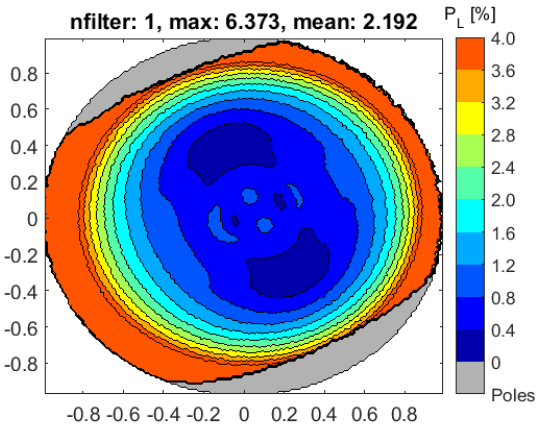

(c) P_L for baerh=0.1, plc=0.56-0.36bar

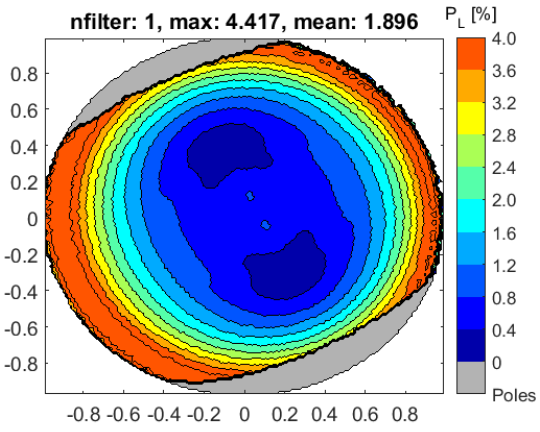

(d) P_L for baerh=0.5, plc=0.56-0.36bar

Figure C.9: Situation 3: P_L in the U-filter

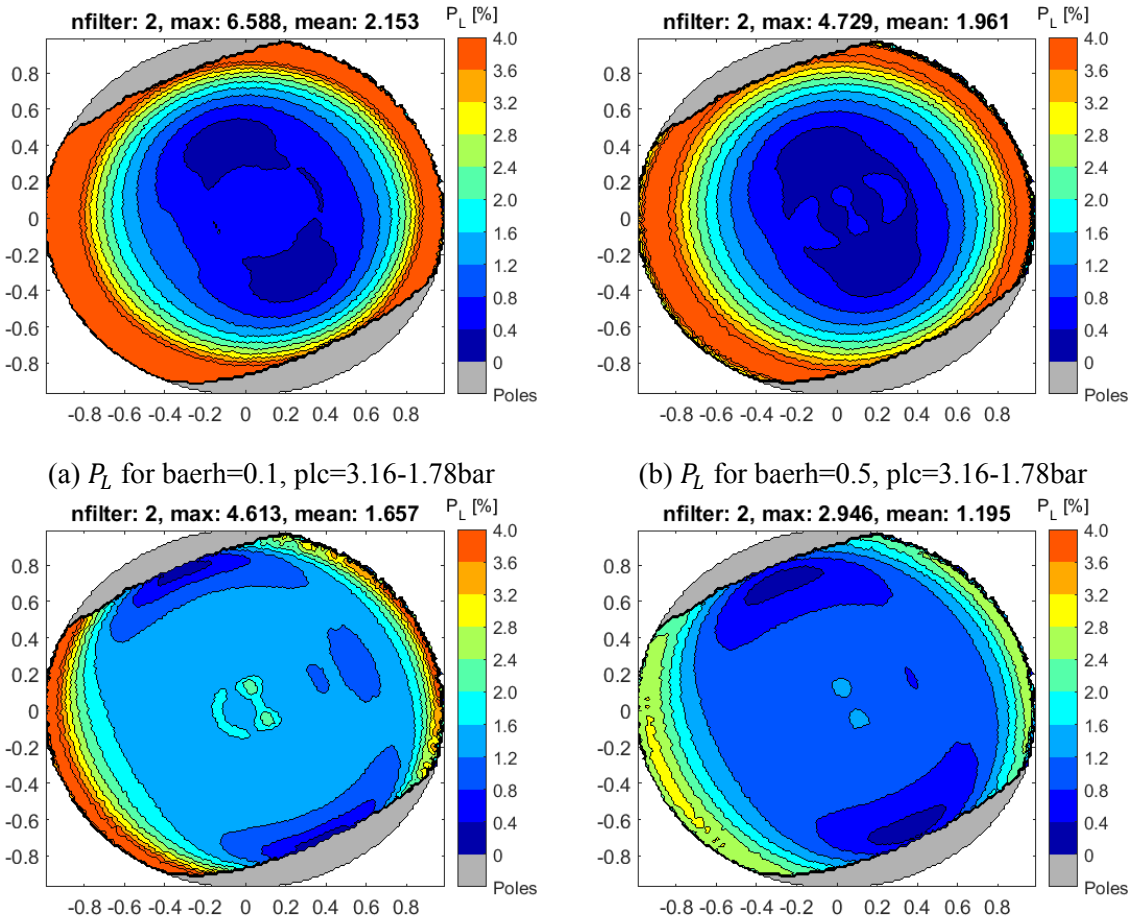

(a) P_L for baerh=0.1, plc=3.16-1.78bar

(b) P_L for baerh=0.5, plc=3.16-1.78bar

(c) P_L for baerh=0.1, plc=0.56-0.36bar

(d) P_L for baerh=0.5, plc=0.56-0.36bar

Figure C.10: Situation 3: P_L in the B-filter

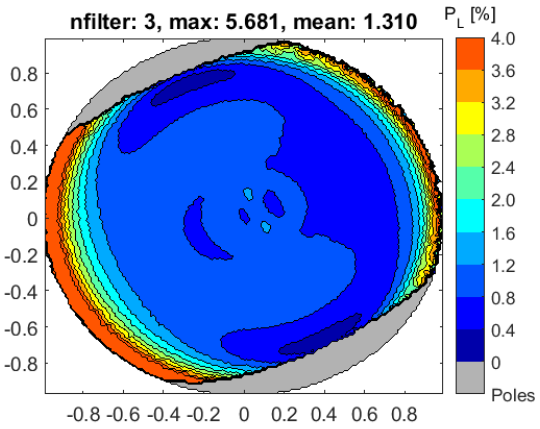

(a) P_L for baerh=0.1, plc=3.16-1.78bar

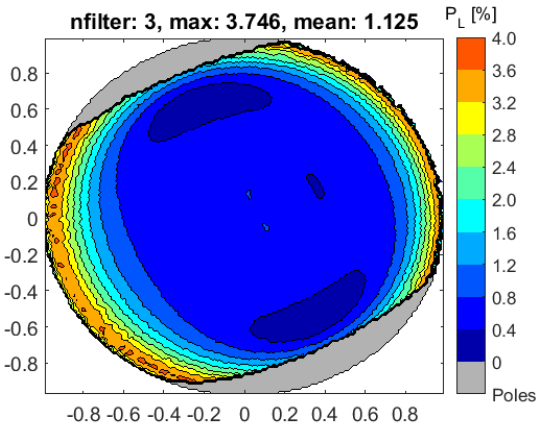

(b) P_L for baerh=0.5, plc=3.16-1.78bar

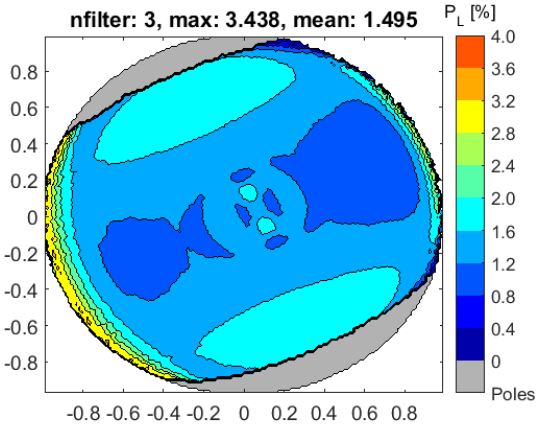

(c) P_L for baerh=0.1, plc=0.56-0.36bar

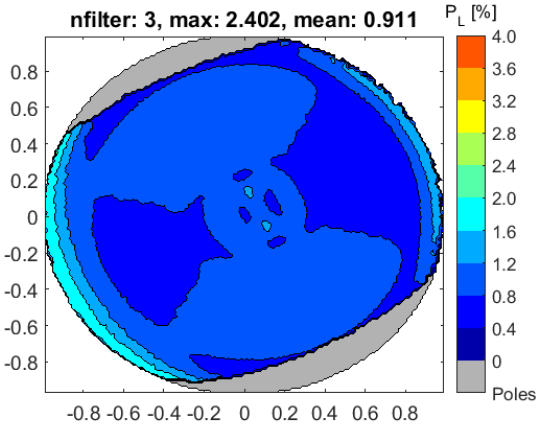

(d) P_L for baerh=0.5, plc=0.56-0.36bar

Figure C.11: Situation 3: P_L in the V-filter

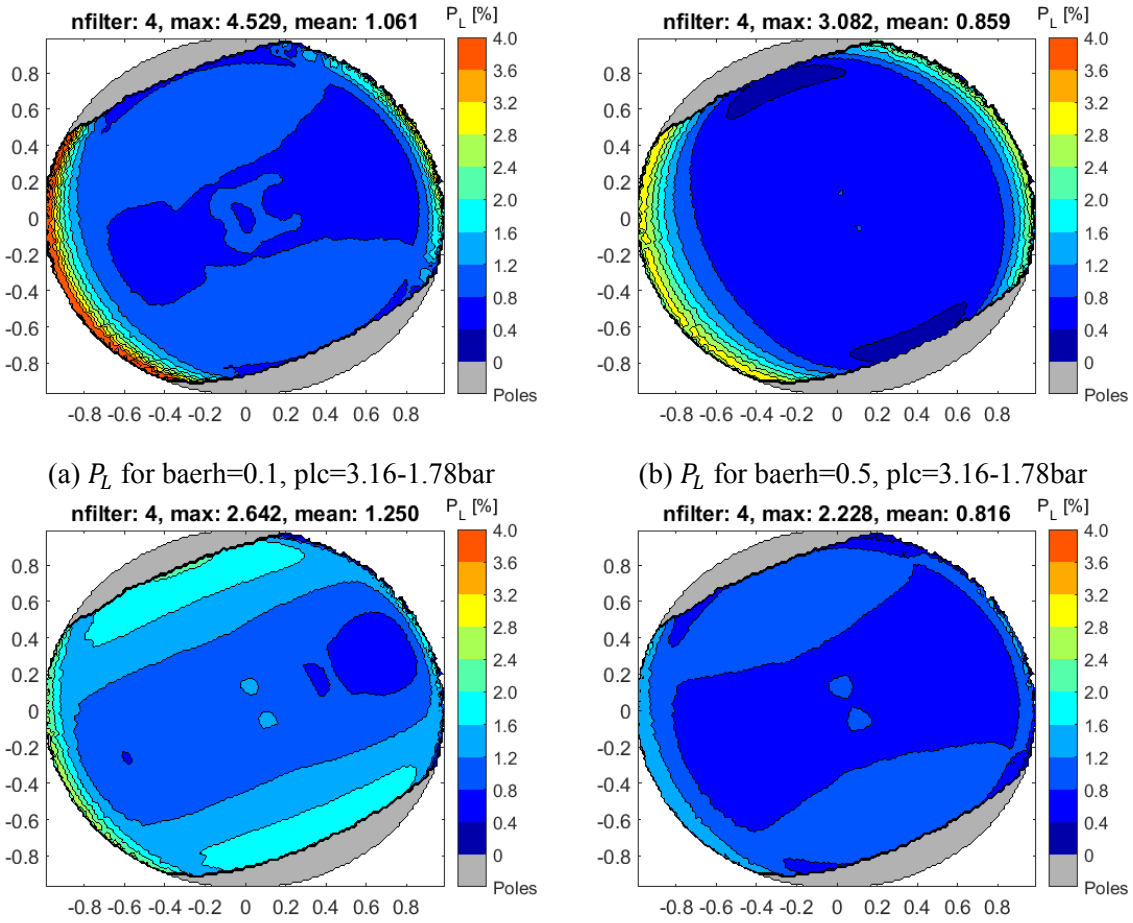

(a) P_L for baerh=0.1, plc=3.16-1.78bar

(b) P_L for baerh=0.5, plc=3.16-1.78bar

(c) P_L for baerh=0.1, plc=0.56-0.36bar

(d) P_L for baerh=0.5, plc=0.56-0.36bar

Figure C.12: Situation 3: P_L in the R-filter

D

Polarisation Difference Optimisation using Different Particles

This appendix shows a comparison of the P_L-difference optimisation per wavelength filter for more than one cloud and haze particle only. The optimisation of ΔP_L per wavelength filter is shown for situation 2 only (the different situations are described in section 5.6) to keep the comparison clear and concise. The parameter values used to generate the figures are displayed in table D.1. The two different particles with r_{eff} as indicated in table D.1 are used to capture the ΔP_L variation along the disk. Note that the amount of variable plc and baerh values are lower for this analysis compared to the results of chapter 6.

Table D.1: Input parameter values

Parameter	Cloud	Haze
$r_{eff}(\mu m)$	0.40, 0.52	0.16, 0.22
v_{eff}	0.05	0.01
nr	1.42+0.015i	1.50+0.001i
p (bar)	variable (4 values [1])	0.1000-0.1334
baer	50	variable (6 values [2])

[1]: from 1.778-3.162bar to 0.3612-0.5623bar [2]: from 0.0-1.0

The P_L comparison of the observations and the numerical model for all wavelength filters is shown in figure D.1 and D.2. From these two figures it is hard to distinguish differences in P_L values with the naked eye for most wavelength filters between the observations and the numerical model. Therefore, the difference in P_L values, which is denoted as ΔP_L, is shown in figure D.3 using the same scale as is used in chapter 6. However, when optimising per wavelength filter and using different particles, ΔP_L per wavelength filter can be kept very low. Consequently, the ΔP_L result is visualised with a more applicable scale in figure D.4.

In fact, the only notable difference in P_L between the observations and the numerical model is that some low P_L regions near the edges of the disk in the R-filter cannot be captured well by the numerical model.

The variable atmospheric parameters being the optical thickness of the haze layer (baerh) and the cloud pressure (plc) corresponding to the minimised ΔP_L values are visualised in figure D.5 and D.6 respectively. From these figures it can be seen that no clear parameter value

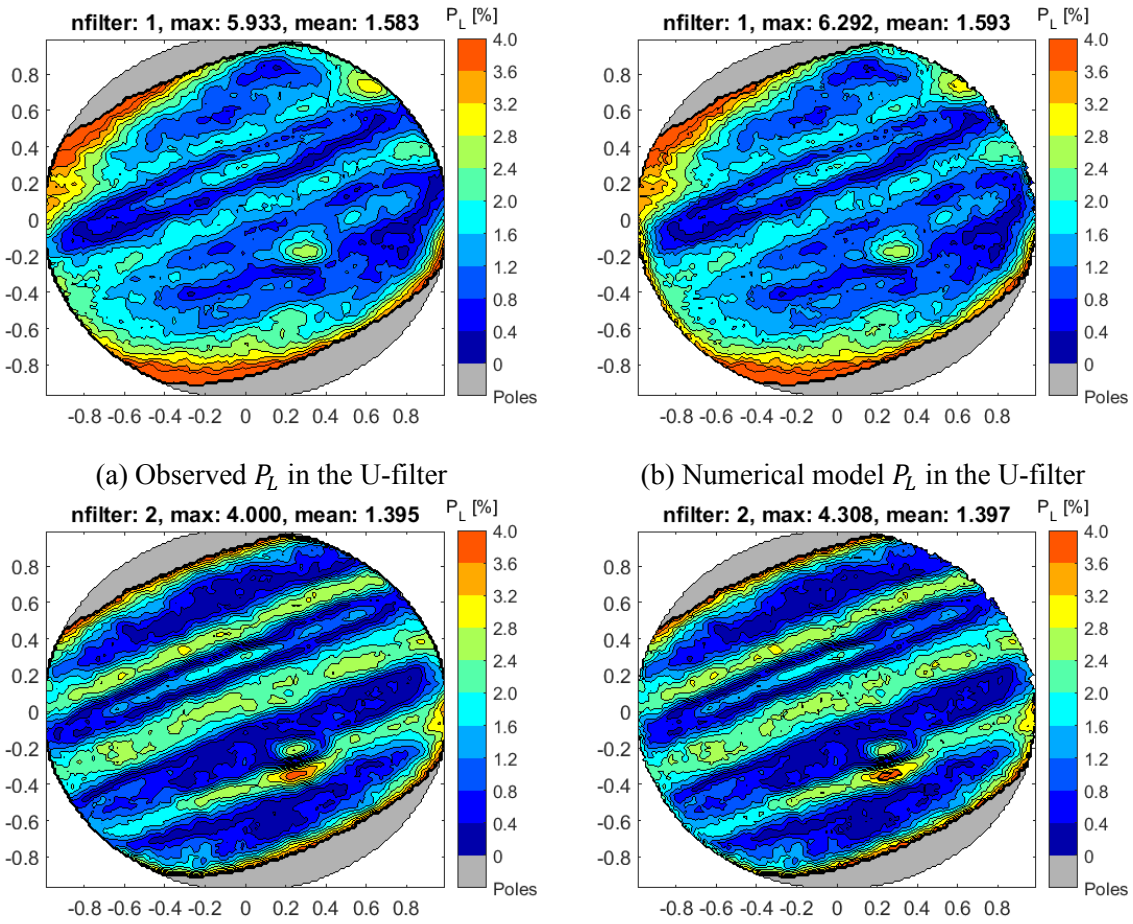

(a) Observed P_L in the U-filter

(b) Numerical model P_L in the U-filter

(c) Observed P_L in the B-filter

(d) Numerical model P_L in the B-filter

Figure D.1: Comparison of the observed and modelled P_L for the U and B-filter

patterns arise. It appears that the variable atmospheric parameters, in combination with the different particles, result in over-fitting when trying to minimise ΔP_L. This result can be expected as no consistency between the four different wavelength filters is implemented. Consequently, the results presented in chapter 6 regard one cloud and haze particle per situation only. In reality, all wavelength filters show the same atmosphere (with the same atmospheric parameter values) but with a different P_L response. That is the advantage of using four different wavelength filters; that the filters add value to the other filters and thus contribute to a more valuable result.

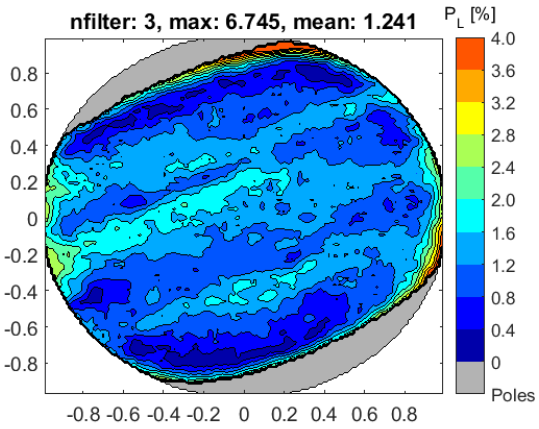

(a) Observed P_L in the V-filter

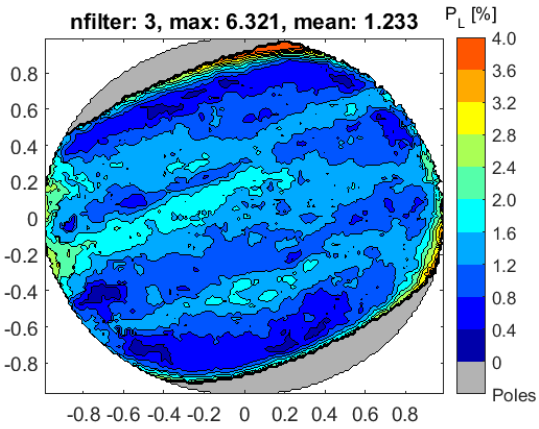

(b) Numerical model P_L in the V-filter

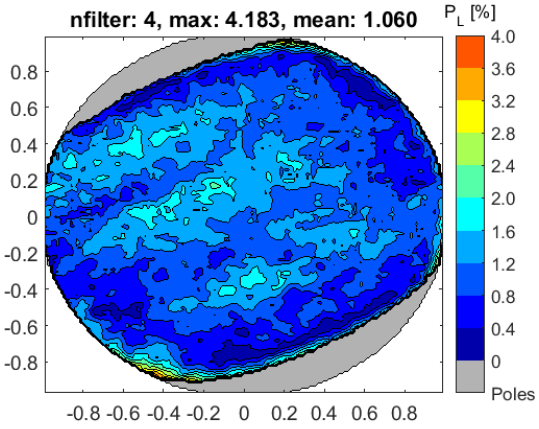

(c) Observed P_L in the R-filter

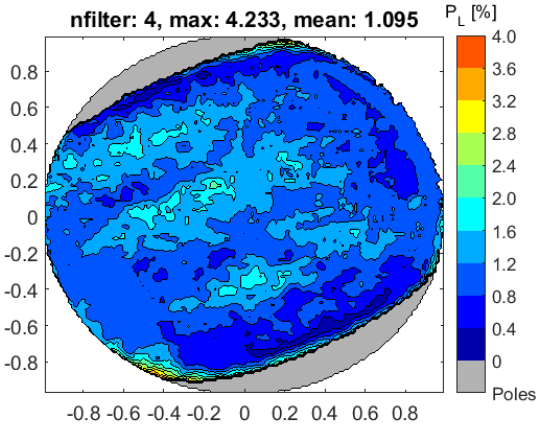

(d) Numerical model P_L in the R-filter

Figure D.2: 1: Comparison of the observed and modelled P_L for the V and R-filter

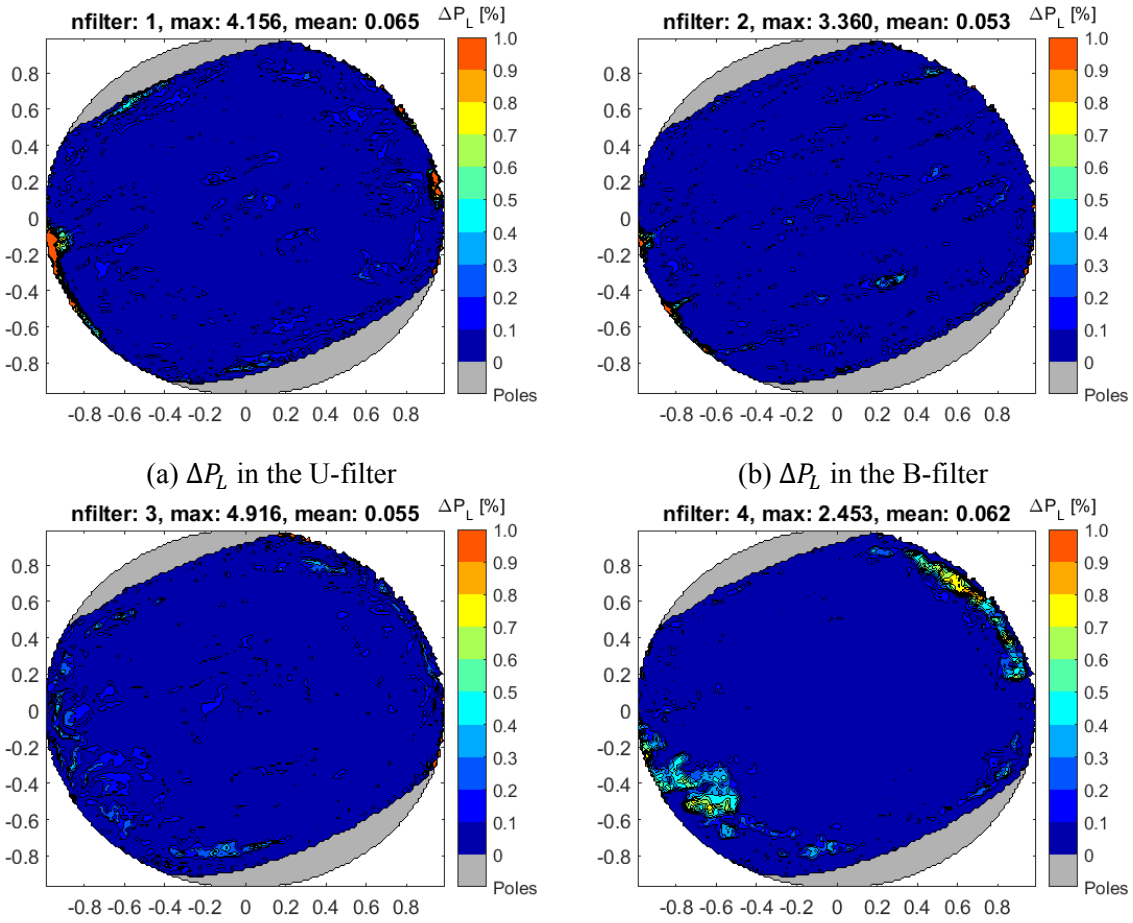

(a) ΔP_L in the U-filter

(b) ΔP_L in the B-filter

(c) ΔP_L in the V-filter

(d) ΔP_L in the R-filter

Figure D.3: 1: P_L-difference between the observations and the numerical model

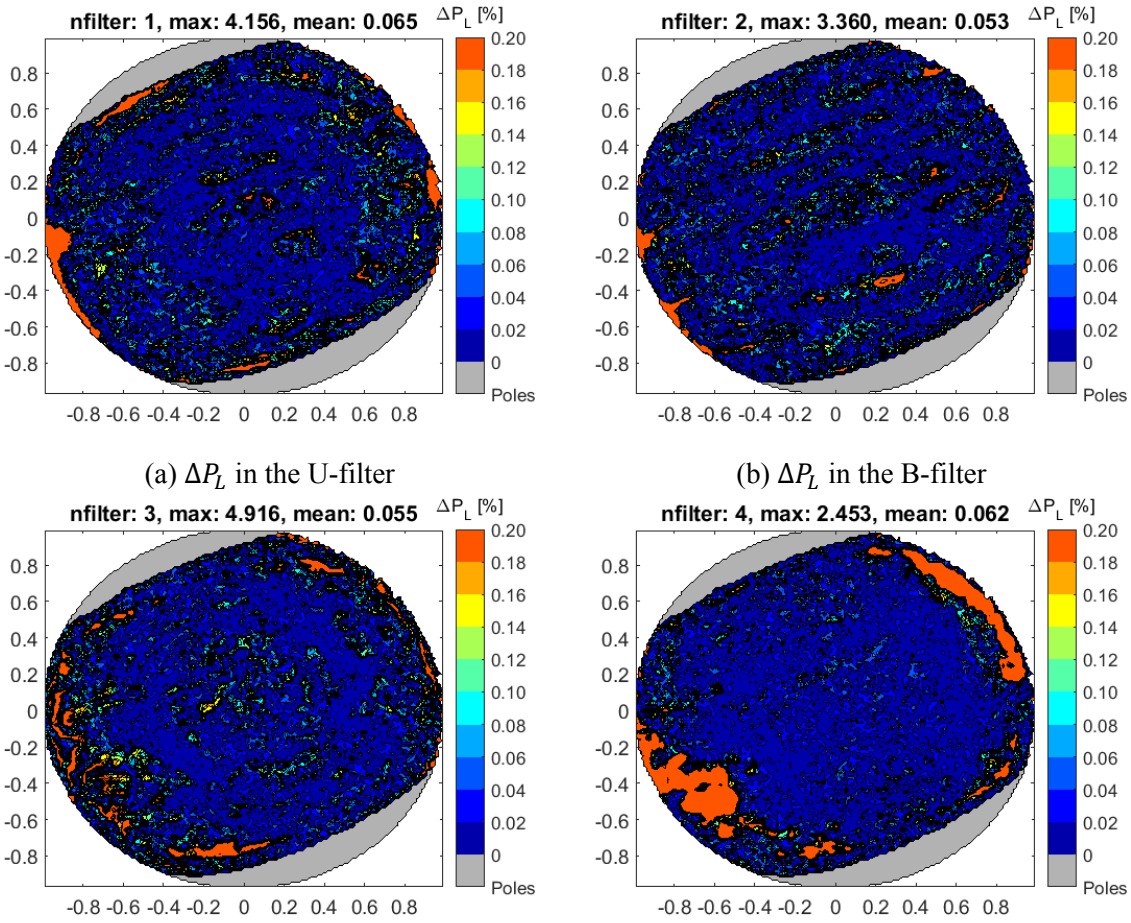

(a) ΔP_L in the U-filter

(b) ΔP_L in the B-filter

(c) ΔP_L in the V-filter

(d) ΔP_L in the R-filter

Figure D.4: 1: P_L-difference plots with a different scale

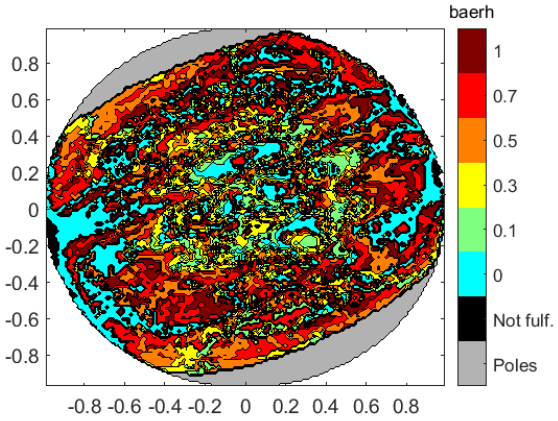

(a) baerh minimising ΔP_L in the U-filter

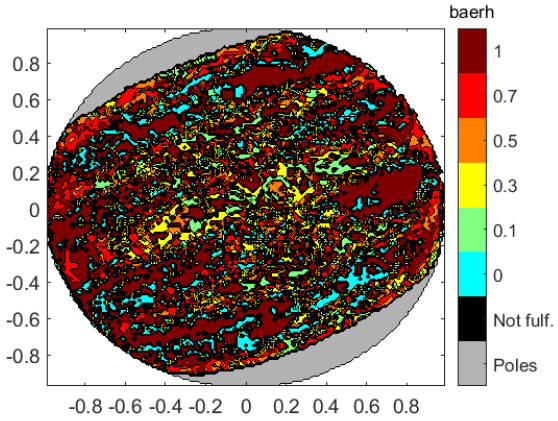

(b) baerh minimising ΔP_L in the B-filter

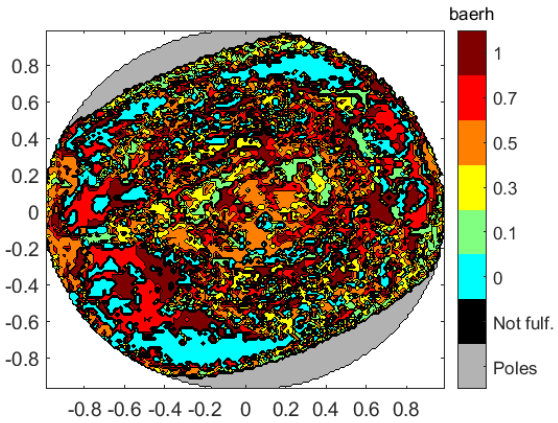

(c) baerh minimising ΔP_L in the V-filter

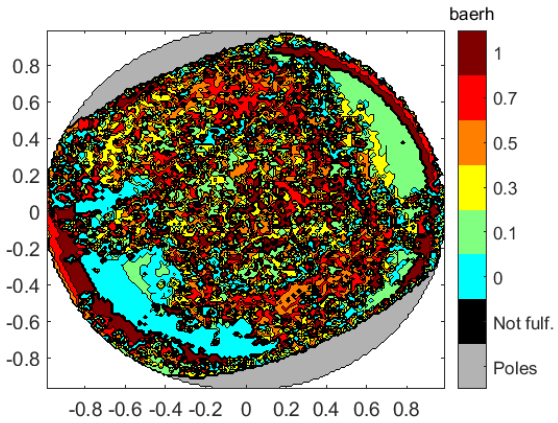

(d) baerh minimising ΔP_L in the R-filter

Figure D.5: 1: baerh result minimising ΔP_L

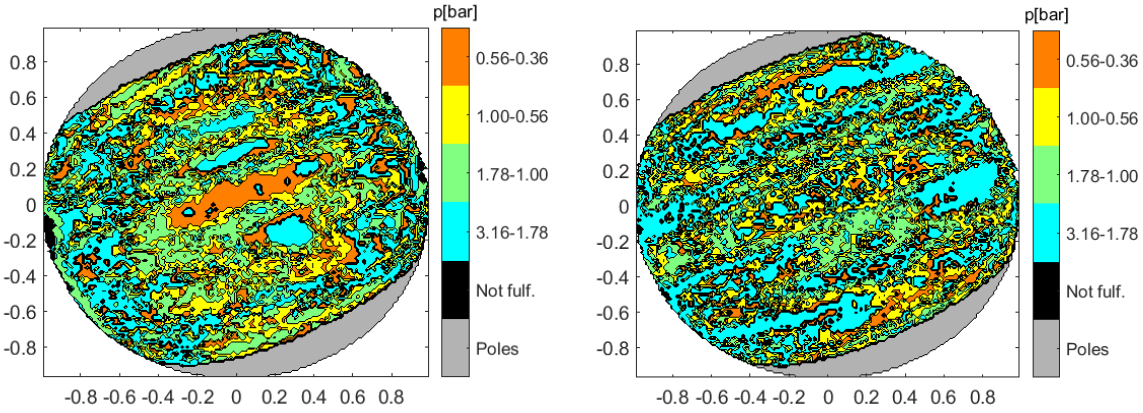

(a) plc minimising ΔP_L in the U-filter

(b) plc minimising ΔP_L in the B-filter

(c) plc minimising ΔP_L in the V-filter

(d) plc minimising ΔP_L in the R-filter

Figure D.6: 1: plc result minimising ΔP_L

E

Fitting the Observations with Different Particle Size

This appendix gives an insight in how the P_L-difference referred to as ΔP_L varies for some different sized cloud and haze particles. This P_L-difference with the observed P_L is minimised per wavelength filter and per pixel for a variable cloud pressure (plc) and haze optical thickness (baerh). The results for different $r_{c,eff}$ and $r_{h,eff}$ for a variable plc and baerh are shown in Figure E.1 to E.7. The other parameters used in this fitting are indicated in table E.1.

Table E.1: The constant values corresponding to the different particles

Parameter	Cloud	Haze
v_{eff}	0.05	0.01
nr	1.42+0.015i	1.50+0.001i
plc	variable (3.16-1.78, 1.78-1.00, 1.00-0.56, 0.56-0.36)bar	14 (0.1000-0.1334bar)
baer	25	variable (0.0, 0.1, 0.3, 0.5, 0.7, 1.0)

[1]: from 1.778-3.162bar to 0.3612-0.5623bar [2]: from 0.0-1.0

The P_L-difference of the particle properties of situation 1 are added to the appendix to have a comparison with the particle properties presented above.

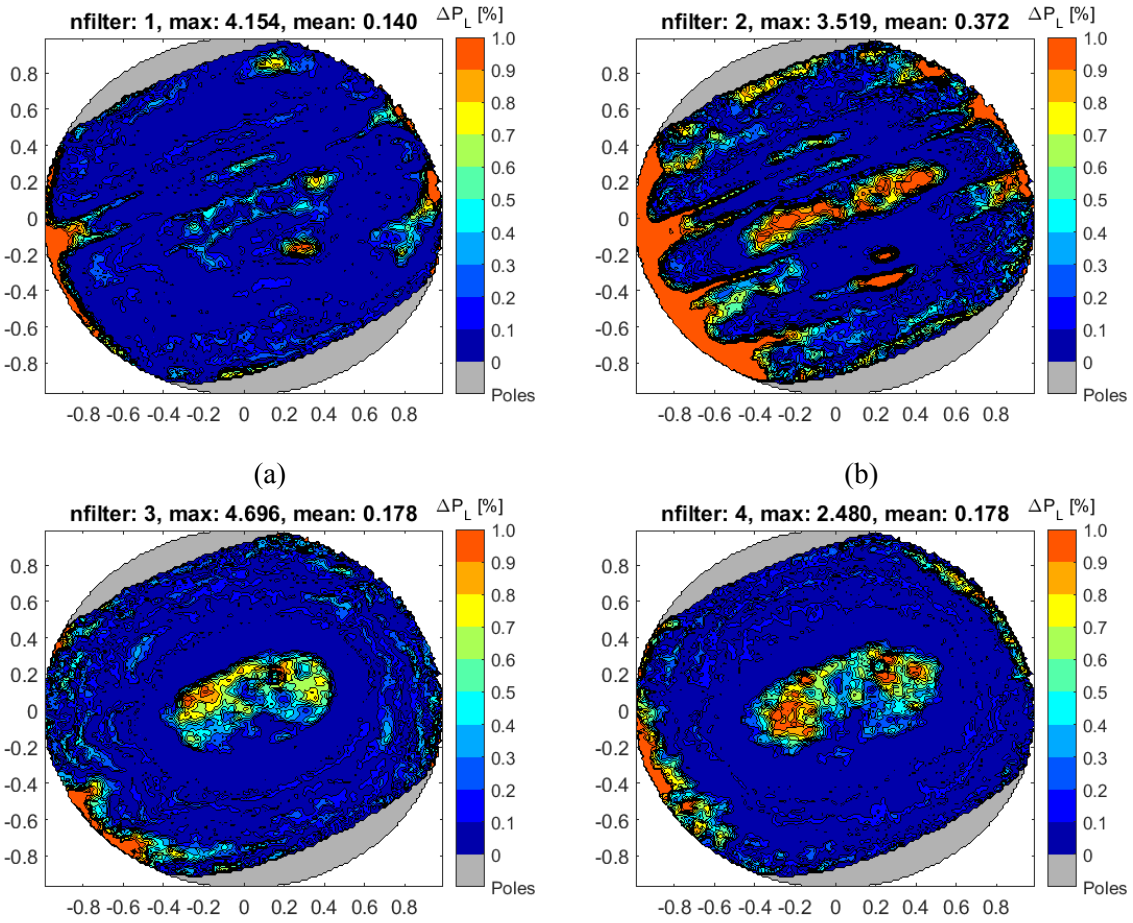

Figure E.1: ΔP_L for $r_{c,eff} = 0.30\mu m$, $r_{h,eff} = 0.12\mu m$

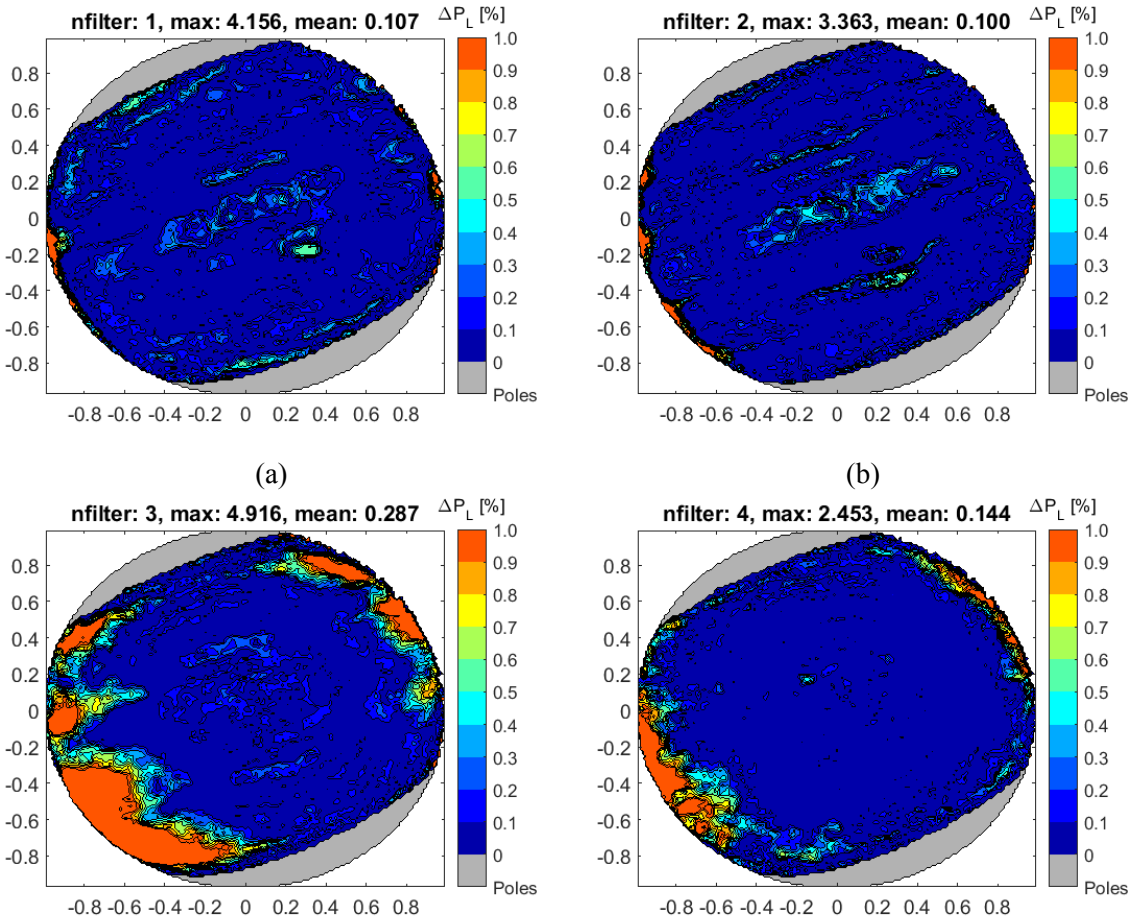

Figure E.2: ΔP_L for $r_{c,eff} = 0.40\mu m$, $r_{h,eff} = 0.16\mu m$

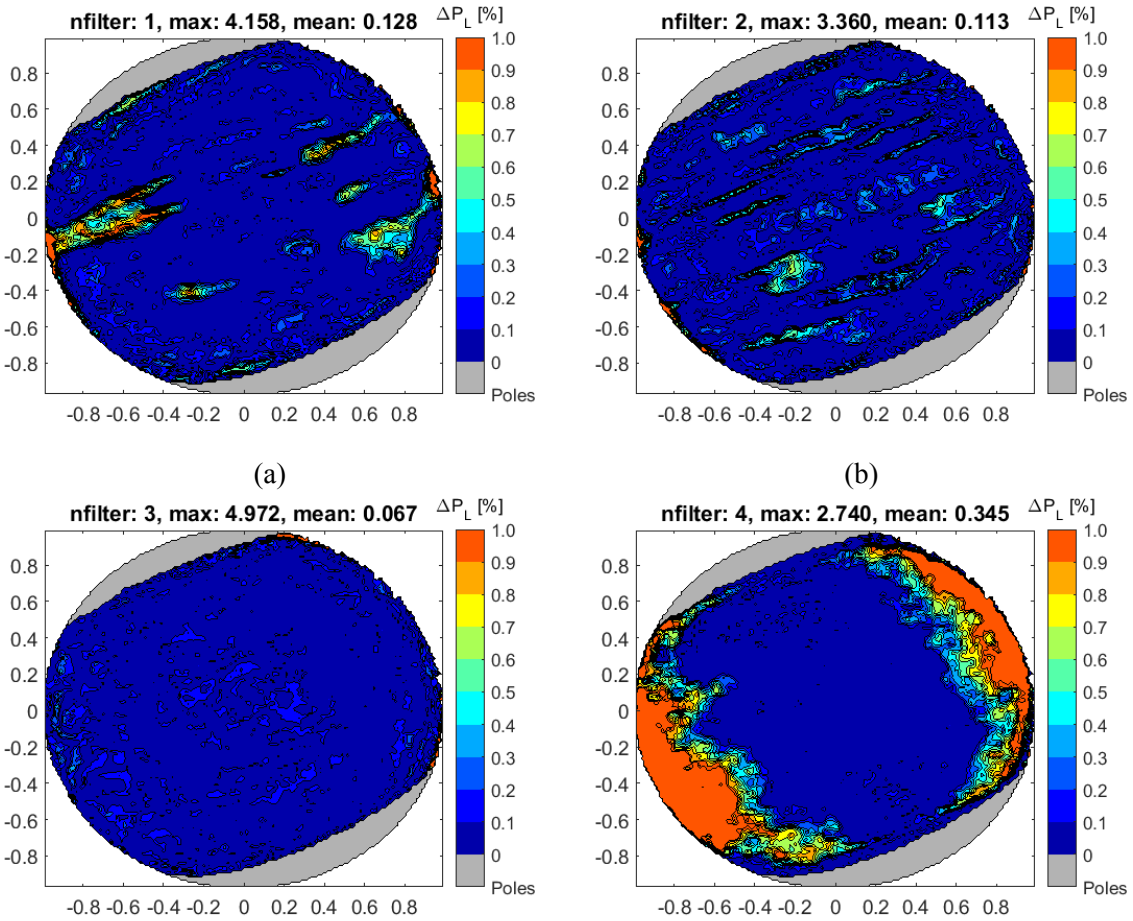

(a) (b)

(c) (d)

Figure E.3: ΔP_L for $r_{c,eff} = 0.50\mu m$, $r_{h,eff} = 0.20\mu m$

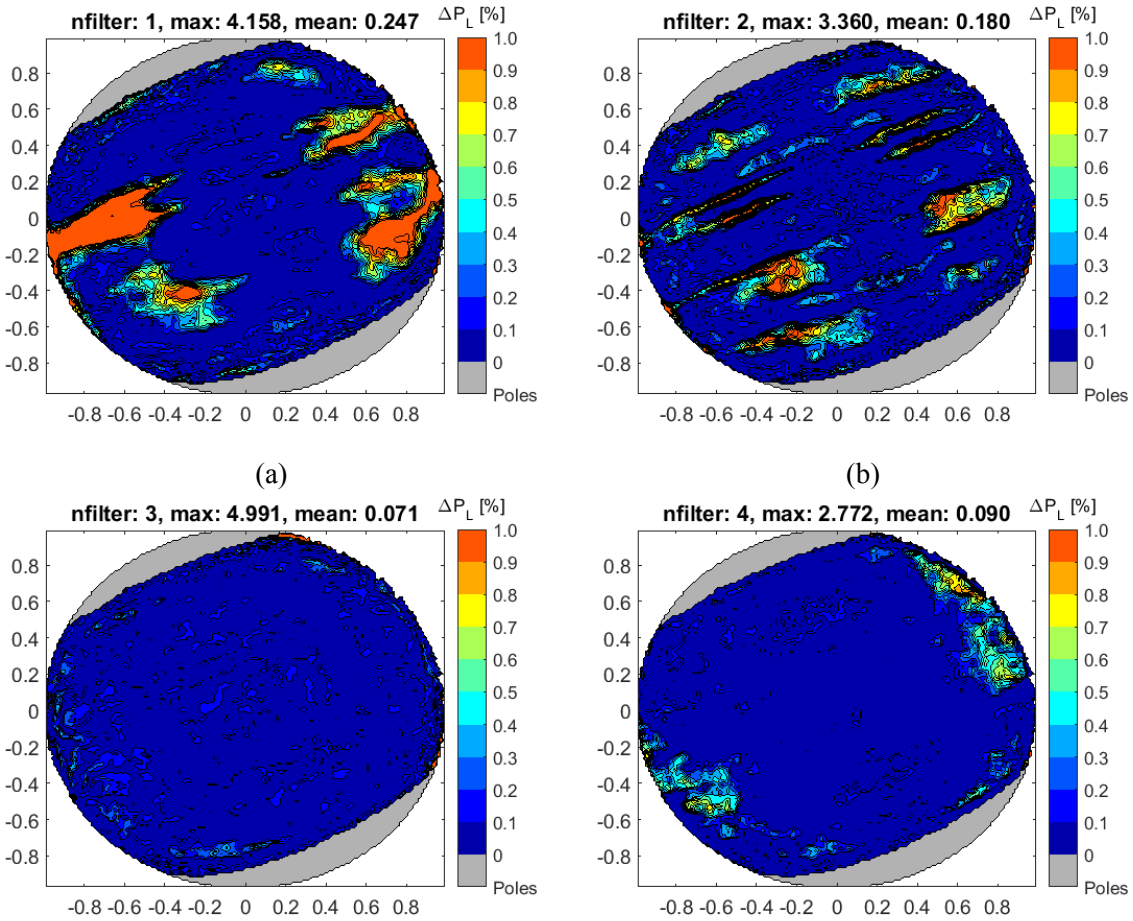

(a) (b)

(c) (d)

Figure E.4: ΔP_L for $r_{c,eff} = 0.52\mu m$, $r_{h,eff} = 0.22\mu m$

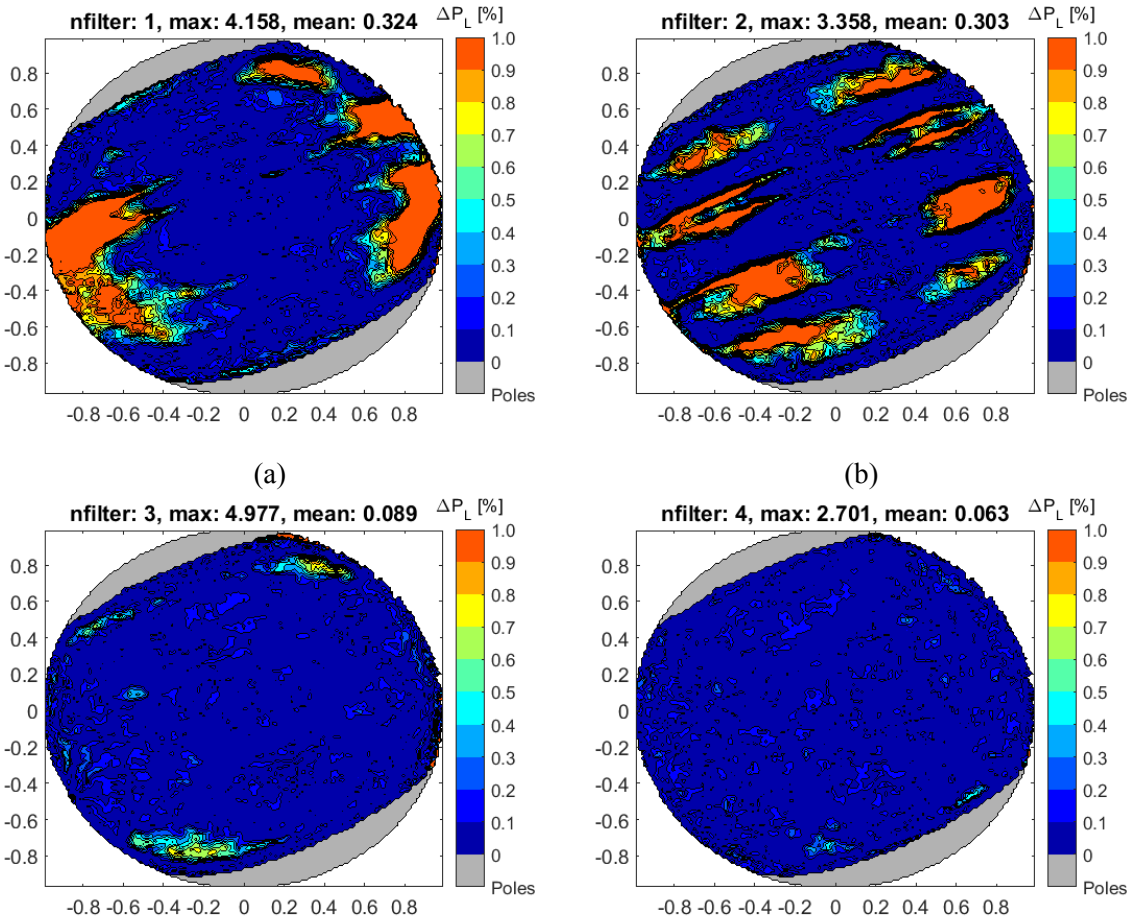

(a) (b)

(c) (d)

Figure E.5: ΔP_L for $r_{c,eff} = 0.60\mu m$, $r_{h,eff} = 0.24\mu m$

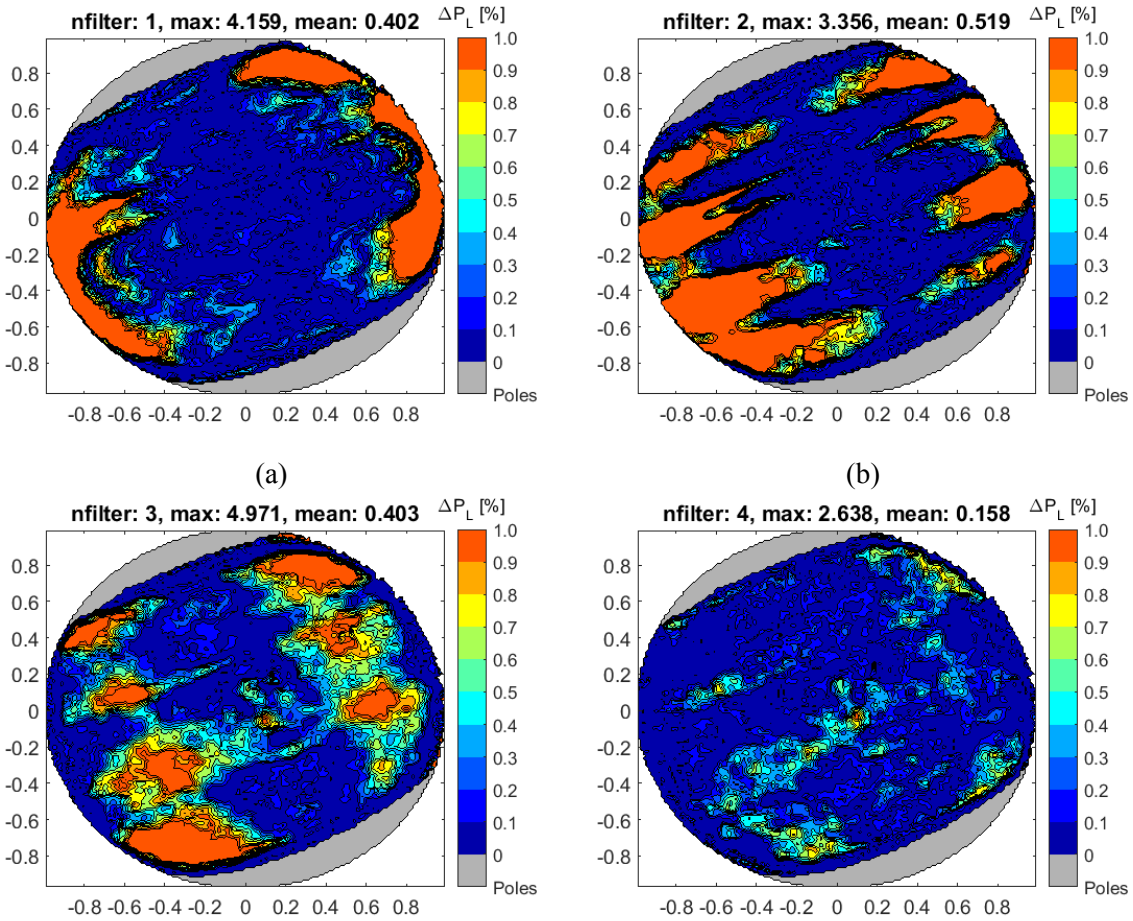

(a) (b)

(c) (d)

Figure E.6: ΔP_L for $r_{c,eff} = 0.70\mu m$, $r_{h,eff} = 0.28\mu m$

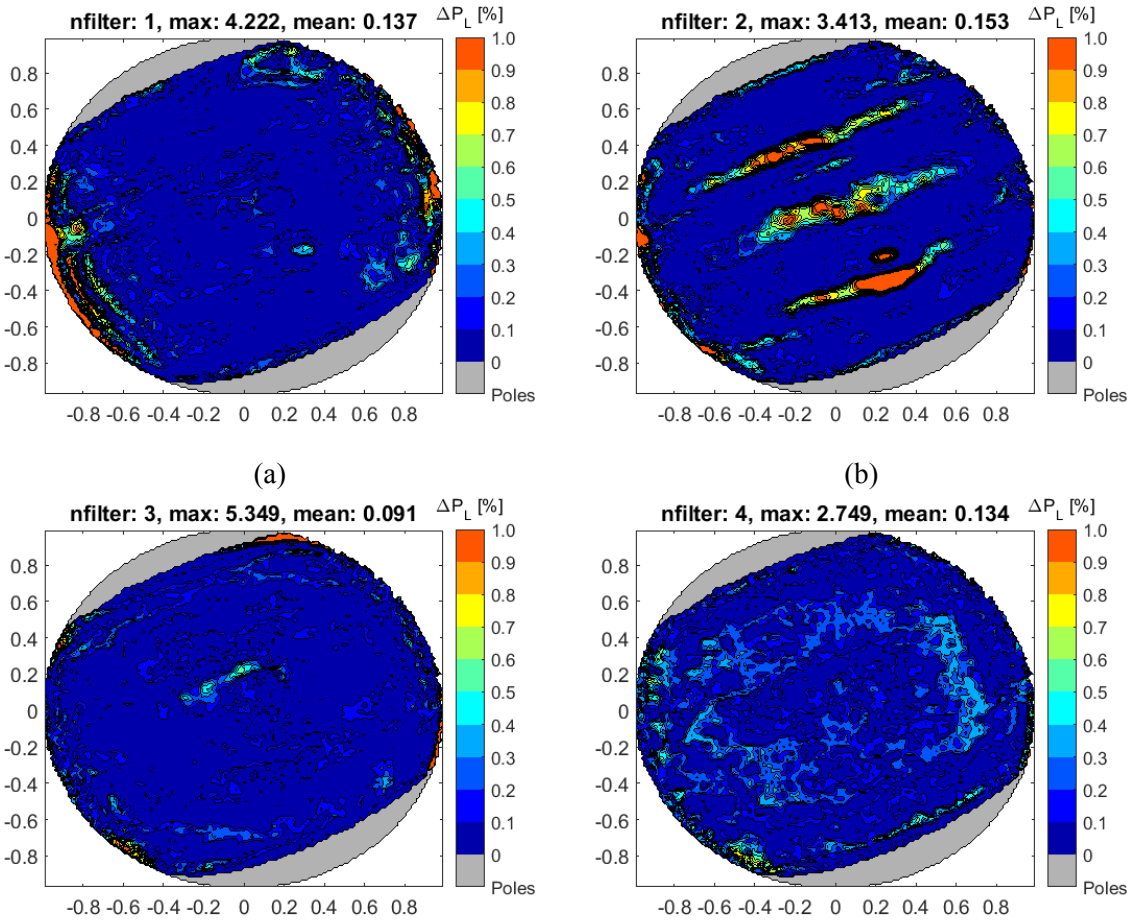

Figure E.7: ΔP_L for $r_{c,eff} = 1.00\mu m$, $r_{h,eff} = 0.50\mu m$

F

Overview of Contribution

This appendix contains the aspects discussed with external persons and indicates the corresponding parts of this report. Three external persons are contacted; William McLean, Maria Fernández Jiménez and Erich Karkoschka.

Erich Karkoschka provided tabulated data to construct Jupiter's geometric albedo curve of figure 4.4 which is used for verification of the geometric albedo to approximate UV-absorption. This curve is also present in subsequent figures as well.

Regarding Maria Fernández Jiménez contribution to this MSc thesis report, no direct contribution to the content is made. She helped me to link the Mie, DAP and GEOS files by means of a shell (.sh) file to run these three parts in one go. We discussed the optimisation procedure to find a good fit of the observations.

As the additions to the numerical model were already implemented, the Fortran code she sent me has not been used. Finally, she provided me with some reference papers which I had already found during my Literature Survey. The citations to those reference papers were therefore already present in my report.

William McLean (SRON, Netherlands Institute for Space Research, Utrecht) was contacted personally twice (on 19-07-2019 and 18-10-2019) and contacted by e-mail. We discussed about the alignment/distortion error and the observational errors (see section 3.2.1 and 3.2.2) were he elaborated upon some aspects provided in his paper ([McLean et al., 2017]). Also, we talked about the imaginary part of the refractive index, which I took into account in the optimisation procedure described in 5.5 as an optimisation parameter. I talked with my supervisor Daphne Stam about this parameter as well and about the fact that the geometric albedo of Jupiter can be used to estimate this parameter value for both the cloud and haze particles to use as initial value in the optimisation analysis to approximate UV-absorption (situation 3). Finally, we talked about how to compensate for the errors (3.2) in the analysis which he took into account by using avering/smoothing. This possibility was discussed with my supervisor but according to her this was not required for my results.

F.1. Report, explanation per section

Abstract: "characterisation of planetary atmospheres and potentially to detect and characterise exoplanets", is based on previous research, among others in [Stam et al., 2004]. General polarisation information can be found in various related research and is therefore not cited. It is described what is performed in this analysis and what the results are.

Introduction: Information from sources is cited accordingly. Previous research of [McLean et al., 2017] and [Fernández Jiménez, 2018] is explicitly mentioned.

Section 2.1: First part, stated hereafter, is based on general descriptions of the phenomenon of polarisation. This knowledge is combined and rewritten to explain this term as good as possible: "Light is a collection of transverse electromagnetic waves, where the electric and magnetic field oscillate perpendicularly to both the propagation direction and to one another. The electric field oscillation defines the polarisation state. Starlight consists of a lot of these electromagnetic waves, and the polarisation direction is totally uncorrelated such that this light is called unpolarised."

Equation 2.1, reference to [Hansen and Travis, 1974].

Figure 2.1 is self-made.

Section 2.2: The (main) sensitivity of polarimetry to the upper atmospheric layers appears several times in this report and is based on what my supervisor told me.

This section is based on what I discussed with my supervisor. All other used sources are cited accordingly.

Figure 2.2 is self-made.

Section 2.3: All used sources are cited accordingly.

Section 2.4 A similar section (about the Stokes Vector) appears in many polarisation-related documents (as [Stam et al., 2004], [McLean et al., 2017], etc.) All used sources are cited accordingly.

Chapter 3: Citations to [McLean et al., 2017] and [Devogèle et al., 2017]. The former describes how the degree of linear polarisation (P_L) can be obtained from the observations and the latter how and where the observations are taken.

Section 3.1: In this section the basic working principle of the Torino Polarimeter is described. Citation to [Oliva, 1997].

Section 3.2: The error and inaccuracies part. I discussed this part with William McLean who provided me with some additional insights on top of the work stated in his paper ([McLean et al., 2017]).

Section 3.2.1: The errors are investigated and addressed in [McLean et al., 2017] which therefore is cited. I discussed with William McLean about the noise error as I was curious how he came up with equation 3.4 to 3.6. He explained me that it took quite some time and effort and that he came up with these equation together with S. Bagnulo such that he could not explain it to me in a nutshell.

Section 3.2.2: I discussed with William McLean about the alignment and distortion error, which he explained to me in more detail such that I better understood how it works. Therefore his paper [McLean et al., 2017] is cited in this section.

Section 3.2.3: In this subsection the photon noise error for the observations are estimated with the equations from [McLean et al., 2017], which is cited accordingly.

Section 3.2.4: In this subsection I estimated the alignment error based on what I discussed with my supervisor.

Section 3.3: This section describes the wavelength filters used in this analysis which are based on data from [Bessell, 1990].
Section 4.1.1: The addition of aggregates of particles by, among others [Karalidi et al., 2013] and [McLean et al., 2017] is mentioned. Furthermore, the existing code is described and the fundamental equations are mentioned.
Section 4.1.2: The doubling adding algorithm is described in [de Haan et al., 1987] but is based on [Rossi et al., 2018]. Again, I explain what this part of the code fulfils.
Section 4.1.3: The equations in this part are described by [Hansen and Travis, 1974] which is cited therefore accordingly.
Section 4.2.1: In this subsection it is described how the optical thickness as function of wavelength is implemented; based on which theories and equations. It contains the corresponding citations. The origin of the values of table 4.2 are mentioned explicitly together with the concerning citations.
Section 4.2.2: In this subsection the implementation of the methane absorption is addressed. The absorption coefficients used are from [Karkoschka and Tomasko, 2009] which is cited accordingly. The procedure of the computation of the absorption is based on [Sánchez-Lavega, 2011] which is therefore cited as well.
Section 4.2.3: All information is cited accordingly.
Section 4.3: The verification of the Fortran code is addressed here and it is shown with data from [Stam et al., 2004] that the Fortran code works as expected.
Section 4.4: This section describes an approximation of absorption at lower wavelength. All information is cited accordingly.
Section 4.5: This analysis is carried out by myself in the begin of my MSc thesis. All figures are generated using the Fortran and my Matlab codes. The Fortan code described in section 4.1 was provided by my former supervisor. The additions made by me are addressed in section 4.2.
Section 5.1: This section describes the Matlab code and how it is linked to the existing and added Fortran code. As this work is performed by me, no citations are needed.
Section 5.2: I explain the data processing steps I carried out in the analysis. Therefore, no citations are present in this section.
Section 5.3.1: It is explained why the polar regions are disregarded in the analysis. I discussed this with my supervisor.
Section 5.3.2: I discussed with William McLean averaging/data smoothing to compensate for error sources. In conformance with my former supervisor it is decided not to take this into account in this analysis.
Section 5.3.3: I describe how I dealt with the variations in dimensions of the matrices of the observations and the numerical model.
Section 5.4: This section describes the optimisation procedure used in this analysis. No external information is given where a citation would be required.
Section 5.5 (Method): In this section the method is explained. I discussed this with Maria Fernández Jiménez, but I used another optimisation method in consultation with my supervisor. Therefore, nothing what I have discussed with Maria is present in this section. I discussed with William McLean about the imaginary part of the refractive index (nri) which I took into account as one of the optimisation parameters. I investigated the nri-values based on the geometric albedo values as discussed with my supervisor (see section 4.2). I took starting values from [Stam et al., 2004] and [McLean et al., 2017] to determine the parameter values of the

parameters described in this section using grid search.
Section 5.6: In this section the different situations used in the Results chapter are addressed. Consequently, no citations are present.
Chapter 6 (Results): In this chapter I describe my obtained results and explain them based on what I discussed with my supervisor. I discussed with William McLean a comparison of the Flux values which would be interesting on top of the P_L-comparison and this is therefore present in section 6.6.
Conclusions and Recommendations: Based on all work done. Cited accordingly.
Appendices: All computations are self-performed to verify the Fortran and Matlab code, and to analyse the accuracy vs the computation time. Verification figures to verify with are obtained from other sources which are all cited accordingly.